

JOURNAL *of*  
UNDERGRADUATE  
REPORTS IN PHYSICS

VOLUME XXX  
ISSUE 1

.....  
2021



JURP

A PUBLICATION OF THE SOCIETY OF PHYSICS STUDENTS  
Available online at [www.spsnational.org](http://www.spsnational.org)

# Editor-in-Chief

Brad R. Conrad

# Editor

Will Slaton

# Managing Editor

Kayla D. Stephens

# Contributing Editors

Kendra Redmond

# Art Director

Aaron Hansen

# Layout Designer

Michael Wernert

# SPS President

Kiril Streletsky,  
Cleveland State University

# SPS Director

Brad R. Conrad



1 Physics Ellipse  
College Park, MD 20740-3841

301.209.3007 (tel)  
301.209.0839 (fax)  
sps@aip.org  
www.spsnational.org



Find SPS on:



# Journal of Undergraduate Reports in Physics

(ISSN 0731-3764) is the publication of the Society of Physics Students, published annually by the American Institute of Physics. Printed in the USA. Standard postage paid at Freeport, OH. POSTMASTER: Send address changes to JURP, One Physics Ellipse, College Park, MD 20740-3841.

The American Institute of Physics is a federation of scientific societies in the physical sciences, representing scientists, engineers, educators, and students. AIP offers authoritative information, services, and expertise in physics education and student programs, science communication, government relations, career services, statistical research in physics employment and education, industrial outreach, and history of the physical sciences. AIP publishes *Physics Today*, the most closely followed magazine of the physical sciences community, and is also home to the Society of Physics Students and the Niels Bohr Library & Archives. AIP owns AIP Publishing LLC, a scholarly publisher in the physical and related sciences. [www.aip.org](http://www.aip.org)

# Table of Contents

2021 • VOLUME XXX, ISSUE 1

<b>LETTER FROM SPS PRESIDENT</b> .....	1
Generalized Null Lagrangians for Equations with Special Function Solutions .....	2
Mapping the Photoresponse of the Quantum-Dot Based Photon-Number-Resolving Detector .....	6
Nitrogen Beams with a National Electrostatics Corporation Alphasource and a 5SDH Accelerator .....	12
Demonstrating the Sagnac Effect Using Tabletop Optics on a Rotary Platform .....	19
Test Particle Calculation of Plasma Equilibria. ....	23
PhysiCL: An OpenCL-Accelerated Python Physics Simulator .....	26
Microgel Dynamics Characterization Using SEM .....	31
Quantum Inequalities and Particle Creation in the Presence of an External, Time-Dependent Mamaev-Trunov Potential .....	36
Probing the Energy Gaps of a Multi-Gap Superconductor: $\text{Ba}_{(1-x)}\text{K}_x\text{Fe}_2\text{As}_2$ .....	48
Photometric Study of RR Lyrae Star TV Lyn .....	52
Viscoelastic relaxation of the nuclear envelope does not cause the collapse of the spindle after ablation in <i>S. pombe</i> .....	58
Preliminary Examination of Uncertainties due to Parton Distribution Functions in Far-Forward Neutrino Production at the Large Hadron Collider. ....	61
Installation of a Cosmic-Ray Trigger System to Commission the Belle II Experiment Vertex Detector with Cosmic Rays .....	66
Preparing a Manuscript for Publication .....	73

# AIP Member Societies:

American Association of Physicists in Medicine  
American Association of Physics Teachers  
American Astronomical Society  
American Crystallographic Association  
American Meteorological Society  
American Physical Society  
Acoustical Society of America  
AVS: Science & Technology of Materials, Interfaces, and Processing  
The Optical Society  
The Society of Rheology

# Other Member Organizations:

Sigma Pi Sigma physics honor society  
Society of Physics Students  
Corporate Associates

# A Letter from the SPS President

by Alina Gearba-Sell, US Air Force Academy (USAFA)



**ABOVE:** Alina Gearba-Sell  
Photo courtesy of SPS National Office.

**The Society of Physics Students is a professional organization “that exists to help students transform themselves into contributing members of the professional community.” At the core of its mission stands the firm belief that involvement in a research project cultivates a distinct set of skills that will enhance an undergraduate’s experience and better prepare them for the challenges that they will encounter in their professional careers.**

According to the Council of Undergraduate Research, undergraduate research refers to “an inquiry or investigation

conducted by an undergraduate student that makes an original intellectual or creative contribution to the discipline,” and the benefits of undergraduate research are far-reaching.

As such, SPS has developed a variety of programs and initiatives designed to take an undergraduate through the entire research process, from the formulation of a problem, to the development of the solution, and through to the dissemination of the results.

The SPS Chapter Research Award provides research grants to support chapter research projects led by undergraduates under the supervision of a faculty mentor. This program is designed to develop critical thinking and problem-solving skills, teamwork, as well as oral and written communication skills. In addition, it could serve as a foundation for how to address complex problems in the future, whether in graduate school or the workforce. A successful proposal requires undergraduates to present a clear statement of the problem and its significance, perform a thorough literature search, lay out a well-thought-out plan for conducting the proposed research with milestones set along the way, and prepare a research budget. Performing the actual research will instill a sense of ownership in undergraduates, while enhancing their leadership and project management skills at the same time. Communicating with the research mentor on a regular basis will bolster confidence in their ability to bring the project to completion and demonstrate

the benefits of networking and collaborative research. Submitting a final report at the conclusion of the project will provide an opportunity to reflect on the research accomplishments and contemplate future avenues to be pursued, while emphasizing the importance of belonging to a professional community.

The SPS Award for Outstanding Undergraduate Research recognizes individual undergraduates who made significant research contributions to any physics-related field. SPS provides additional opportunities in travel and reporter awards for undergraduates to present their research at professional conferences and connect with the community. SPS also offers a summer internship program in research, education and policy with emphasis in building a strong community.

The Journal of Undergraduate Reports in Physics (JURP) provides a forum for undergraduates to disseminate their research outcomes in a peer-reviewed journal designed to highlight undergraduate work. Supported and hosted by AIP Publishing, AIP Publishing.

We hope this summer will be a great one, you will have the opportunity to participate in a research internship and next academic year you will engage in a face-to-face research project with a faculty member. We also hope you will consider publishing your research findings or chapter projects in JURP, take advantage of the multitude of opportunities SPS has to offer and engage with the professional community. //

Sigma Pi Sigma ( $\Sigma\Pi\Sigma$ ), the national physics honor society, was founded in 1921 by students at Davidson College. It exists to honor outstanding scholarship in physics, to encourage interest in physics among students at all levels, to promote an attitude of service, and to provide fellowship for those excelling in physics. While its “linked but distinct” counterpart, the Society of Physics Students (SPS), is an organization that helps students transform themselves into contributing members of the professional community, Sigma Pi Sigma serves to provide a lifelong framework through which to advance its mission and provide opportunities to support future physicists.

**The American Institute of Physics (AIP) generously underwrites Sigma Pi Sigma programs, including awards for chapter projects, outstanding service, and lifelong commitment to the organization’s objectives of SPS and  $\Sigma\Pi\Sigma$ . Sigma Pi Sigma also hosts the Physics Congress, or PhysCon, an inclusive conference for undergraduate physics students. We are looking forward with great excitement to the upcoming Physics Congress in Washington, DC, and will mark the centennial celebration of the founding of  $\Sigma\Pi\Sigma$ !**

**[www.sigmapisigma.org/congress/2022](http://www.sigmapisigma.org/congress/2022)**

# Generalized Null Lagrangians for Equations with Special Function Solutions

Atharva A. Dange,<sup>1, a)</sup> Lesley C. Vestal,<sup>1, b)</sup> and Zdzislaw E. Musielak<sup>1, c)</sup>

<sup>1</sup> *Department of Physics, University of Texas at Arlington, Arlington, TX 76019, USA*

<sup>a)</sup>Corresponding author: atharvaatul.dange@mavs.uta.edu

<sup>b)</sup>lesley.vestal@uta.edu

<sup>c)</sup>zmusielak@uta.edu

**Abstract.** A method to derive general standard and null Lagrangians for second-order differential equations whose solutions are special function of mathematical physics is presented. The general null Lagrangians are used to find the corresponding general gauge functions. All derived Lagrangians are new and in special cases they reduce to those published in the literature. The obtained results are applied to the Bessel, Hermite and Legendre equations, which have many applications in physics, applied mathematics and engineering.

## INTRODUCTION

Second-order ordinary differential equations (ODEs), whose solutions are given in terms of special functions (SFs) of mathematical physics [1,2], have many important applications in physics and applied mathematics as shown in standard textbooks (e.g., [3]). For several of these ODEs, Lagrangians were previously constructed [4-6]. More recently, the standard and non-standard Lagrangians for the ODEs with the SF solutions were derived [7]. In this paper, a method is developed to derive the general standard Lagrangians (SLs) as well as the so-called general null Lagrangians (NLs), which identically satisfy the Euler-Lagrange (E-L) equation and can also be expressed as the total derivative of a scalar function, also called a gauge function [8]. The SLs depend on the square of the first derivative of the dependent variable (kinetic energy-like term) and the square of the dependent variable (potential energy-like term). The NLs were studied in mathematics [9,10] and have also applied to elasticity [11], and Newtonian mechanics where they were used to introduce forces [12]. However, the role of the NLs in ODEs with the SF solutions has not yet been fully explored; doing so is the main aim of this paper. Our choice to focus on these ODEs is justified by their many physical applications familiar to graduate and undergraduate science students. Our results are applied to the Bessel, Hermite and Legendre equations as these specific SFs are used in many physical applications. Therefore, the presented results should be of interest to physicists, applied mathematicians and engineers.

## GENERAL STANDARD AND NULL LAGRANGIANS

### Generalization

Let  $\hat{D} = d^2/dx^2 + B(x)d/dx + C(x)$  be a linear operator whose coefficients  $B(x)$  and  $C(x)$  are ordinary and smooth ( $C^\infty$ ) functions. If  $\hat{D}$  acts on  $y(x)$ , which is also ordinary and smooth, then the resulting ODE can be written in the following explicit form

$$y'' + B(x)y' + C(x)y = 0. \quad (1)$$

By specifying the coefficients  $B(x)$  and  $C(x)$ , all ODEs with the SF solutions are obtained and for these equations we derive the SLs and NLs. Let  $L_n$  be a null Lagrangian and  $L_s$  be a standard Lagrangian that is used to derive an ODE with the SF solutions. The NLs described above imply that the total Lagrangian  $L_{tot}$  given by  $L_{tot} = L_s + L_n$  leads to the same ODE as using  $L_s$  only. In other words, the addition of  $L_n$  does not change the outcome when the E-L is applied. In this paper, we develop a general method to drive the standard Lagrangians together with a new family of NLs that are used to find the corresponding gauge functions.

The starting point of this method is to consider the general Lagrangian:

$$L(y', y(x), x) = \frac{1}{2}f_1(x)y'^2 + \frac{1}{2}f_2(x)yy' + \frac{1}{2}f_3(x)y^2 \quad (2)$$

where  $f_1(x)$ ,  $f_2(x)$ , and  $f_3(x)$  are ordinary and smooth functions to be determined. This Lagrangian depends on the square of the first derivative of the dependent variable (kinetic energy-like term), the square of the dependent variable (potential energy-like term) and on the mixed term with the dependent variable and its derivative. Substituting the above Lagrangian into the E-L equation, we obtain:

$$y'' + \left(\frac{f_1'}{f_1}\right)y' + \frac{1}{f_1}\left(\frac{1}{2}f_2' - f_3\right)y = 0. \quad (3)$$

Comparing (1) and (3) we get  $B(x) = \frac{f_1'}{f_1}$  and  $C(x) = \frac{1}{f_1}\left(\frac{1}{2}f_2' - f_3\right)$ , which gives  $f_1 = c_1 e^{\int B(x)dx} = c_1 E_s$  and

$f_3 = \frac{1}{2}f_2' - C(x) \cdot f_1 = \frac{1}{2}f_2' - C(x) \cdot (c_1 E_s)$ , where  $c_1$  is the integration constant and  $E_s = e^{\int B(x)dx}$ . Substituting  $f_1(x)$  and  $f_3(x)$  into  $L(y', y, x)$ , we find:

$$L(y', y, x) = L_s(y', y, x) + L_n(y', y, x) \quad (4)$$

where

$$L_s(y', y, x) = \frac{1}{2}c_1 E_s(x) [y'^2(x) - C(x)y^2(x)] \quad (5)$$

and

$$L_n(y', y, x) = \frac{1}{2}y(x) \left[ f_2(x)y'(x) + \frac{1}{2}f_2'(x)y(x) \right] \quad (6)$$

with  $L(y', y, x)$  being a combination of the general standard Lagrangian  $L_s(y', y, x)$  and the general null Lagrangian  $L_n(y', y, x)$ . It must be noted that  $L_s(y', y, x)$  generalizes the Caldirola-Kanai (CK) Lagrangian [13,14] and it reduces to the CK Lagrangian when  $B(x) = b = \text{const.}$  and  $C(x) = c = \text{const.}$ ; this SL also describes a harmonic oscillator with time dependent mass and spring constant.

## General Gauge Functions

Having obtained the general null Lagrangian, we now derive its general gauge function  $\varphi$  using:

$$L_{null} = \frac{1}{4}f_2'(x)y^2(x) + \frac{1}{2}f_2(x)y(x)y'(x) = \frac{d\varphi}{dx} = \frac{\partial \varphi}{\partial x} \Big|_{y=c} + \frac{\partial \varphi}{\partial y} \Big|_{x=c} \cdot y'(x). \quad (7)$$

Which gives,

$$\varphi = \frac{1}{4}f_2(x)y^2(x). \quad (8)$$

With  $f_2(x)$  being arbitrary, the following three cases may be considered:

- i)  $f_2 = 0 \rightarrow L_s = L_{s,min} \quad (\text{trivial case})$
- ii)  $f_2 = \text{constant} \rightarrow L_{mid} = L_{s,mid} + L_{n,mid}$
- iii)  $f_2 = f_1' \rightarrow L_{max} = L_{s,max} + L_{n,max}$



Substituting each of the cases in our gauge equation (8), we get our three-gauge functions respectively:

- i)  $\Phi = \frac{1}{4}f_2(x)y^2(x) = 0$  *No gauge function*  
 ii)  $\phi = \frac{1}{4}f_2(x)y^2(x) = \frac{1}{4} \cdot c \cdot y^2(x) = c_2y^2(x)$  *V variable gauge function*  
 iii)  $\phi = \Phi_{max} = \frac{1}{4}c_1 \cdot E_s(x) \cdot B(x) \cdot y^2(x)$  *Max variable gauge function*

## APPLICATIONS

Applications of our results to selected ODEs with the SF solutions are summarized in the following table.

**TABLE 1.**

	Equation	$L = L_S + L_n$	$L_{n,max}$	$\Phi_{max}$
General	$y'' + B(x)y' + C(x)y = 0$	$\frac{1}{2}f_1(x)y'^2 + \frac{1}{2}f_2(x)yy' + \frac{1}{2}f_3(x)y^2$	$\frac{1}{2}y[f_2y' + \frac{1}{2}f_2'y]$	$\frac{1}{4}f_2(x) \cdot y^2(x)$
General Bessel	$B(x) = \frac{\alpha}{x}$ $C(x) = \beta \left(1 + \gamma \frac{\mu^2}{x^2}\right)$	$\frac{1}{2}c_1 \cdot x[y'^2 - C(x)y^2] + \frac{1}{2}y[f_2y' + \frac{1}{2}f_2'y]$	$\frac{1}{2}c_1e^{\alpha c_2} \cdot \alpha x^{\alpha-1} \cdot y \left[\frac{\alpha-1}{2}x^{-1}y + y'\right]$	$\frac{1}{4}c_1 \cdot e^{\alpha c_2} \cdot \alpha x^{\alpha-1} \cdot y^2(x)$
Regular Hermite	$B(x) = -x$ $C(x) = x$	$\frac{1}{2}c_1e^{\frac{-x^2}{2}}[y'^2 - xy^2] + \frac{1}{2}y[f_2y' + \frac{1}{2}f_2'y]$	$\frac{1}{2}e^{\frac{-x^2}{2}} \cdot y \left[\frac{1}{2}y(x^2 - 1) - xy'\right]$	$\frac{1}{4}e^{\frac{-x^2}{2}} \cdot x \cdot y^2(x)$
Regular Legendre	$B(x) = \frac{2x}{1-x^2}$ $C(x) = \frac{l(l+1)}{1-x^2}$	$\frac{1}{2}c \left 1 - x^2\right  \left[y'^2 - \left(\frac{l(l+1)}{1-x^2}\right) \cdot y^2\right] + \frac{1}{2}y[f_2y' + \frac{1}{2}f_2'y]$	$\pm xcy' \pm \frac{1}{2}cy^2$	$\pm \frac{1}{2}c \cdot x \cdot y^2(x)$

By selecting  $\alpha$ ,  $\beta$  and  $\gamma$  different (regular, modified, spherical and spherical modified) Bessel equations are obtained.

## CONCLUSION

We considered the linear second-order ODEs whose solutions are given by the SF of mathematical physics, and derived general standard and null Lagrangians. The obtained Lagrangians are new and they generalize those previously found. The derived gauge functions are also new. The obtained results are applied to the Bessel, Hermite and Legendre equations, thus, they are of primary interests to physicists and applied mathematicians. The presented results can be easily applied to any ODE with the SF solutions.

## ACKNOWLEDGMENTS

We are grateful to two anonymous referees for carefully reading our manuscripts and providing detailed comments and suggestions that helped us to improve our paper.

## REFERENCES

1. G.M. Murphy, *Ordinary Differential Equations and Their Solutions*, (Dover Publication, Inc., New York, 2011).

2. H. Hochstadt, *The Functions of Mathematical Physics*, (Dover Publication, Inc., New York, 1986).
3. G.B. Arfken and H.J. Weber, *Mathematical Methods for Physicists*, (Elsevier Academic Press, New York, 2005).
4. M.C. Nucci and P.G.L. Leach, *J.Math. Phys.*, **48**, 123510 (2007).
5. Z.E. Musielak, *J.Phys. A: Math. Theor.*, **41**, 055205 (2008).
6. J.L. Cieřliński and T. Nikiciuk, *J.Phys. A: Math. Theor.*, **43**, 175205 (2010).
7. Z.E. Musielak, N. Davachi, and M. Rosario-Franco, *Mathematics*, **8**, 379 (2020).
8. P.J. Olver, *Applications of Lie Groups to Differential Equations*, (Springer, New York, 1993).
9. D. Krupka and J. Musilova, *Diff. Geom. Appl.*, **9**, 225 (1998).
10. M. Crampin and D.J. Saunders, *Diff. Geom. Appl.*, **22**, 131 (2005).
11. G. Saccomandi and R. Vitolo, *J. Math. Sci.*, **136**, 4470 (2006).
12. Z.E. Musielak and T.B. Watson, *Phys. Let. A*, **384**, 126838 (2020).
13. P. Caldirola, *Nuovo Cim.*, **18**, 393 (1941).
14. E. Kanai, *Prog. Theor. Phys.*, **3**, 44 (1948).



The poster features a dark background with a yellow city skyline silhouette at the bottom. A green nebula or aurora-like glow is centered behind the skyline. The title "100 YEARS OF MOMENTUM" is written in large, white, sans-serif capital letters, with the "100" and "YEARS" being significantly larger than "OF MOMENTUM". The text is suspended by thin white lines, giving it a hanging sign appearance.

**100 YEARS OF MOMENTUM**

Join us for  $\Sigma\Pi\Sigma$ 's Centennial — the 2022 Physics Congress.  
100 Years of Momentum. An interactive meeting designed for undergraduate physics and astronomy majors.

**OCTOBER 6-8, 2022 | WASHINGTON, D.C.**

**AIP**  
American Institute of Physics

[sigmapisigma.org/congress/2022](https://sigmapisigma.org/congress/2022)

**SPS**  
2022

# Mapping the Photoresponse of the Quantum-Dot Based Photon-Number-Resolving Detector

Trevor Geerds,<sup>a)</sup> Connor Govin,<sup>b)</sup> and Eric Gansen

*Department of Physics, The University of Wisconsin – La Crosse, 1725 State St, La Crosse, WI 54601, USA*

<sup>a)</sup>Corresponding author: geerds.trevor@uwlax.edu

<sup>b)</sup>connorpgovin@gmail.com

**Abstract.** Efficient and versatile photon-number resolving detectors are critical to the development of future communication systems. The quantum-dot, optically-gated, field-effect transistor (QDOGFET) is one such detector. Utilizing quantum dots (QDs), tiny islands of semiconductor, imbedded in a transistor, QDOGFETs have been shown to exhibit single-photon sensitivity and photon-number-resolving (PNR) capabilities. A photon is detected when it photocharges a QD, which alters the amount of current flowing through the transistor by screening the gate field. Crucial to the resolving power is that each charged QD produce the same response, regardless of its location within the active area of the device. Here, we investigate the extent spatial nonuniformities in the QDOGFET's response to light limit its ability to distinguish different numbers of photons. By using an optical-scanning microscope (OSM), contour plots of a QDOGFET's response are acquired that show that the device exhibits localized "hotspots" where it is particularly sensitive to photons. The spatial resolution of the microscope is enhanced by capping the QDOGFET with a solid-immersion lens (SIL). We present experimental results that show how the hotspots depend on bias conditions and help decipher the root cause of the nonuniformities.

## INTRODUCTION

This research is on the study of a novel method of detecting individual photons that makes use of nanometer-sized islands of semiconductor material, referred to as quantum dots (QDs). In a specially designed transistor, referred to as a QDOGFET (quantum dot, optically gated, field-effect transistor) [1-6], an array of QDs is embedded near the transistor's conductive channel. A photon is detected when it photocharges a QD, which alters the amount of current flowing through the transistor by screening the gate field. It has been demonstrated that QDOGFETs exhibit single-photon sensitivity with high internal quantum efficiency [1, 2] and, moreover, can accurately discriminate between the detection of 0, 1, 2, and 3 photons 83% of the time [3, 4]. However, it has also been shown that the resolving power of the detectors degrade as photon number increases, limiting the counts to low numbers. The physical mechanism that causes the degraded photon-number resolution is not well understood but appears to be related to variations in the response of the detector associated with the seed point of the photon. In this work, we present the results of measurements where we use an optical scanning microscope (OSM) and a solid-immersion lens (SIL) to investigate the spatial uniformity of the QDOGFET's response to light and use the results to identify the mechanisms that degrade the resolving power the device.

## BACKGROUND

QDOGFETs employ photoconductive gain [7] and QDs to detect individual photons. Figure 1(a) is a surface image of the device. The structure consists of alternating layers of GaAs and AlGaAs with a single layer of InGaAs QDs at the GaAs/AlGaAs interface, as shown in Fig. 1(b). A thin layer of silicon-doped material (Si  $\delta$ -doping) provides excess electrons to the conduction band (CB), forming a two-dimensional electron gas (2DEG) at the GaAs/AlGaAs interface adjacent to the QDs. The detector is fabricated by depositing source and drain ohmic



contacts on the structure surface, etching a mesa between the contacts, and depositing a semitransparent platinum (Pt) Schottky-barrier gate across the mesa. The area where photons are detected is defined by the gated portion of the channel mesa, which for the QDOGFET studied in this work, is  $5.625 \mu\text{m}^2$  in area and encompasses about 2000 QDs.

The principles of operation of the QDOGFET are shown in Fig. 1(b). During operation, a reverse bias (negative gate voltage,  $V_g$ ) is applied to the gate. When a photon is absorbed in the 100-nm-thick GaAs absorption layer (between the QDs and 2DEG), it excites an electron from the valence band (VB) to the conduction band (CB) leaving behind an empty state, or hole, in the VB. Subsequently, the positively charged hole is swept by the internal electric field toward the QDs, where it is trapped, while the excited electron is swept into the 2DEG. Once in a QD, the hole screens the internal field produced by the gate contact, subsequently changing the amount of current flowing in the 2DEG ( $\Delta I_{ds}$ ) for as long as the hole is stored in the dot. The magnitude of the step in current is dictated by the transconductance  $g_m$  of the FET, where care must be taken that the device is operating in the linear transconductive region. These current changes are converted to voltage changes,  $\Delta V_{out} = -R\Delta I_{ds}G$ , via a transimpedance amplifier with resistance,  $R$ , and gain,  $G$ , which are monitored by external electronics. During operation, the QDOGFET and its surrounding circuitry are cooled in order to decrease electrical noise.

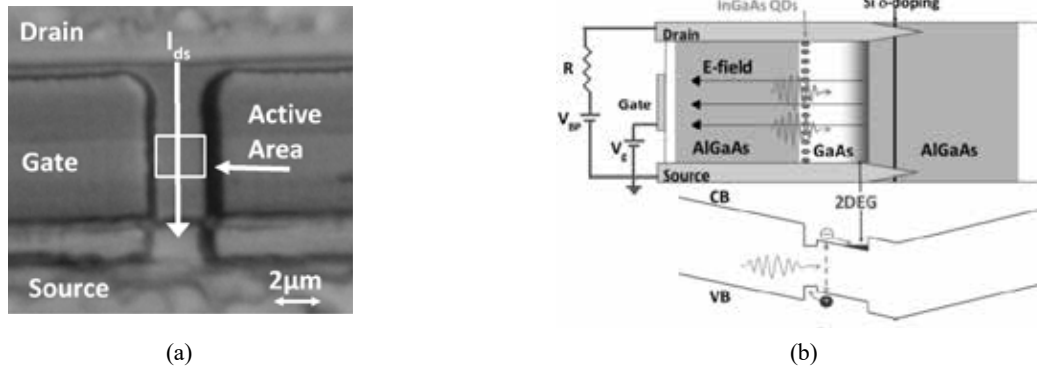


**FIGURE 1.** (a) Image of the QDOGFET surface showing the drain, gate, source, active area, and conventional current direction during operation. (b) Schematic diagram of the composition and band structure of the QDOGFET.

When the gate and 2DEG of the QDOGFET are modelled as conductive plates of an ideal parallel-plate capacitor (PPC) with the QD layer treated as an infinite plane of charge storage, a concise relationship exists between the electrical and structural characteristics of the device and its photoresponse  $\Delta I_{ds}$ . In the small-signal limit, the step in the channel current caused by a single trapped hole is given by

$$\Delta I_{ds} = g_m \frac{eW}{\epsilon' A} \quad (1)$$

where  $e$  is the elementary charge,  $W$  is the distance between the Pt gate and the QD layer,  $\epsilon'$  is the electric permittivity, and  $A$  is the active area [4, 8]. Although these current changes are small, over time even a single trapped hole causes a large change in the cumulative charge transferred in the 2DEG. The photoconductive gain associated with this process provides the detector with single-photon sensitivity. In addition, in the event that multiple photons photocharge multiple QDs, the net change in current is proportional to the number of photons, provided that each charged QD produces the same response regardless of its location within the active area of the detector. It is this aspect of the QDOGFETs that provides them with photon-number-resolving capabilities and is the focus of this work.

## EXPERIMENTAL PROCEDURE

The uniformity of the responses produced by different QDs within the QDOGFET was investigated using the cryogenic OSM shown schematically in Fig. 2(a). In these measurements, the SIL-capped QDOGFET was cooled to  $\sim 117$  K while focussed 50-ns laser pulses were raster scanned over a 100-point grid, covering its active area. At each point on the grid, the individual steps in the output voltage,  $\Delta V_{out}$ , caused by 200 laser pulses were recorded. The spatial resolution of the OSM was enhanced by mounting a cubic-zirconia SIL on the QDOGFET surface. The

diffraction limited spot diameter of monochromatic light is given by  $\frac{0.52\lambda}{NA}$ , where  $\lambda$  is the wavelength of light,  $n$  is the index of refraction of the medium, and NA is the numerical aperture of the objective lens. As a result, by using a cubic-zirconia SIL with  $n = 2.14$ , the spot size was reduced by about half in comparison to what it would have been for a bare QDOGFET. The OSM utilized a 50x-magnification objective lens with a 13-mm working distance and NA=0.55, resulting in a diffraction limited spot size of 360nm. The actual spot diameter of the OSM was slightly larger due to imperfections within the system. Figure 2(a) shows the ideal case when the laser light is normally incident on the SIL. During scanning, deviation from this ideal case occurs as the laser spot moves over the surface of the SIL. However, the SIL has a diameter of 1mm, while the maximum dimension of our scanned area is less than  $3\mu\text{m}$ . As these lengths differ by 3 orders of magnitude, any distortion effects due to scanning across the SIL are negligible.

From the raster scans of  $\Delta V_{out}$ , contour plots of the mean step height (MSH), the mean number of photons (MNP), and the mean signal per photon (MSP) were produced using the statistical approach detailed in Ref. [2]. These contour plots were then superimposed onto a surface image of the device for reference. For example, a contour plot of the MSH is shown in Fig 2(b) for  $V_g = -0.5\text{ V}$ ,  $V_{BP} = +2\text{ V}$ ,  $R = 100\text{ k}\Omega$ , and  $G = 100$ . Variations in the response of the QDOGFET are apparent in the data, where a “hotspot” consisting of a region of enhanced MSH is observed towards the drain side of the device. In the Results Section of this work, we present contour plots acquired for a variety of bias conditions that show how the hotspot depends on  $V_g$  and  $V_{BP}$ . From these data sets, we gain insight into what is causing the signal nonuniformity. Circuit parameters,  $R$  and  $G$  are kept constant for all measurements presented in this work.

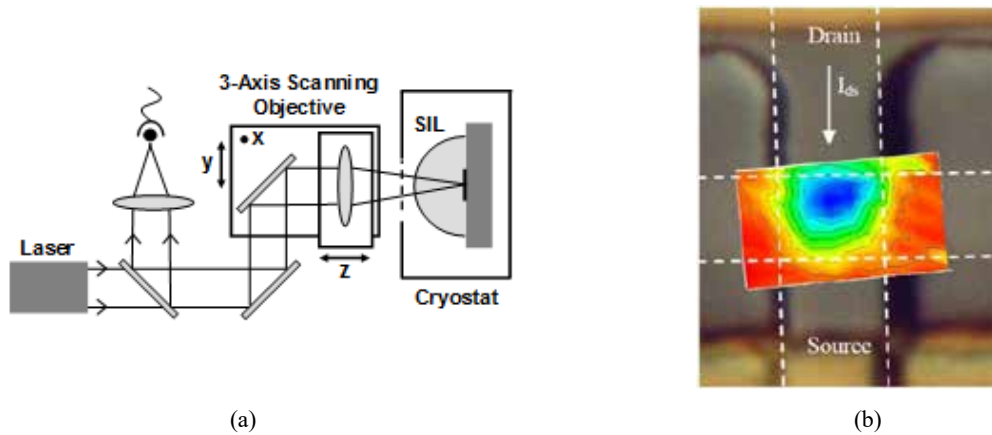


**FIGURE 2.** (a) Schematic diagram of the OSM with SIL integration that was used to map the photo-response of QDOGFETs. (b) Overlay of a MSH contour plot, acquired for  $V_{BP} = +2\text{ V}$  and  $V_g = -0.5\text{ V}$ , on an image of sample, with the active area outlined in dashed lines. For  $V_{BP} > 0$ , the drain potential is higher than the source potential, resulting in channel current  $I_{ds}$  flowing from drain to source.

## RESULTS

Contour plots showing the effect of changing the direction of the channel current are shown in Fig. 3. In Fig. 3(a),  $V_{BP} = +2\text{ V}$ , and  $I_{ds}$  flows in the downward direction, while in Fig. 3(b),  $V_{BP} = -2\text{ V}$ , and  $I_{ds}$  flow in the upward direction. The bottom panels of the figure show the MSH for the entire 100-pt grid, where the active area of the device is indicated by black dashed lines. The top panels show the MNP, and the middle panels show the MSP. For these panels, data is only shown in and around the active area, since calculations of MNP and MSP are nonsensical beyond the boundaries of the active area where the QDOGFET is not sensitive to light. The theoretical value for the signal per photon,  $\Delta V_{out}$ , calculated using Eqn. [1] is also provided in the figure for comparison. It is also marked by a black bar on the MSP legends. The potential difference between the source and drain contacts is also indicated on the figure.

The contour plots shown in Fig. 3 illustrate that the cause of the hotspot is electrical in nature, as opposed to being structural. Notice that for both polarities, the hotspot in the MSH (bottom panels) is observed near the

high-potential side of the gate. This would not be observed if the hotspot were due to variation in the thickness of the gate contact. The MNP and MSP data provide further insight into the origins of the hotspot. The MSP contour plots (middle panels) show some nonuniformity across the active area, but the pattern is less organized than the MSH data. Overall, the MSP measured across the majority of the active area is in good agreement with that predicted by the PPC model for both polarities. By contrast, the nonuniformity observed in the MNP contour plots (top panels) better match those observed for the MSH plots, which indicates that hotspot is a result of more efficient detection of photons seeded near the high-potential side of the active area.

The enhanced detection efficiency observed near the high-potential side of the active area can be explained by the dynamics of the photo-excited holes. While the transport of the holes perpendicular to the plane of the absorption layer is subject to the gate field, the motion of the holes in the plane of the absorption layer is influenced by the potential difference between the source and drain contacts. As such, positively charged holes tend to be “washed” downstream in the direction of the channel current  $I_{ds}$ . Given these dynamics, holes excited towards the high-potential side of the active area flow in the direction of  $I_{ds}$ , but can still be trapped by QDs beneath the gate contact and thus alter the channel current. By contrast, holes generated near the low-potential side of the active area tend to exit the gated area before they can be trapped by a QD.

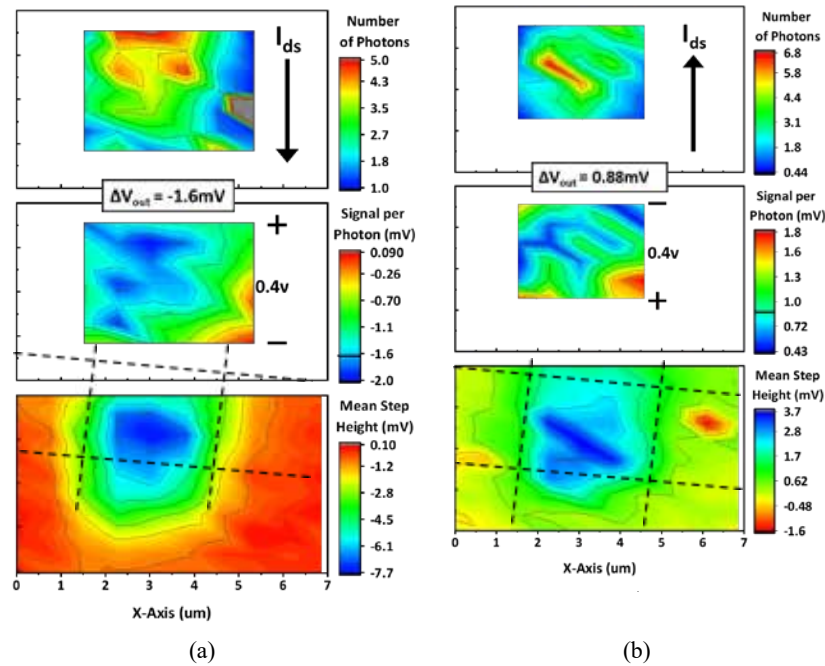


**FIGURE 3.** Contour plots of the MSH (bottom), MSP (middle), and MNP (top) for  $V_g = -0.5$  V and (a)  $V_{BP} = +2$  V, and (b)  $V_{BP} = -2$  V. The signal per photon ( $\Delta V_{out}$ ) calculated using the PPC model and Eqn. [1] is provided for comparison. The potential difference between the source and drain contacts is provided in the middle panel.

The effects of varying  $V_g$  on the contour plots of the MSH, MNP, and MSP are shown in Fig. 4. The bottom panels show that the hotspot is more centrally located on the active area when a lower-magnitude gate voltage is used. As the magnitude of  $V_g$  is increased, the hotspot is pushed further towards the high-potential side of the active area. Also, the MSP becomes less uniform and deviates further from the theoretical  $\Delta V_{out}$ . This behaviour can be explained by the large potential gradient that is formed across the active area when a large gate voltage is used. Notice that for  $V_g = -1.5$  V, the potential difference between the source and drain contacts is 0.85 V, which results in a large gradient in the localized gate voltage over the active area of the device. While the 2DEG located on the low-potential side of the active area is gated by a local  $V_g$  of -1.5 V, the other side is gated by a -2.35 V bias. Holes trapped in QDs on the high-potential side of the active area will screen the larger gate field, which has a bigger impact on the channel current, consistent with the contour of the MSP data shown in Fig. 4(c). The fact that the

MNP is lower on the high-potential side of the active area indicates that although the MSP is enhanced in this region, the detection efficiency is low since most of the photoexcited holes drift out of the area downstream.

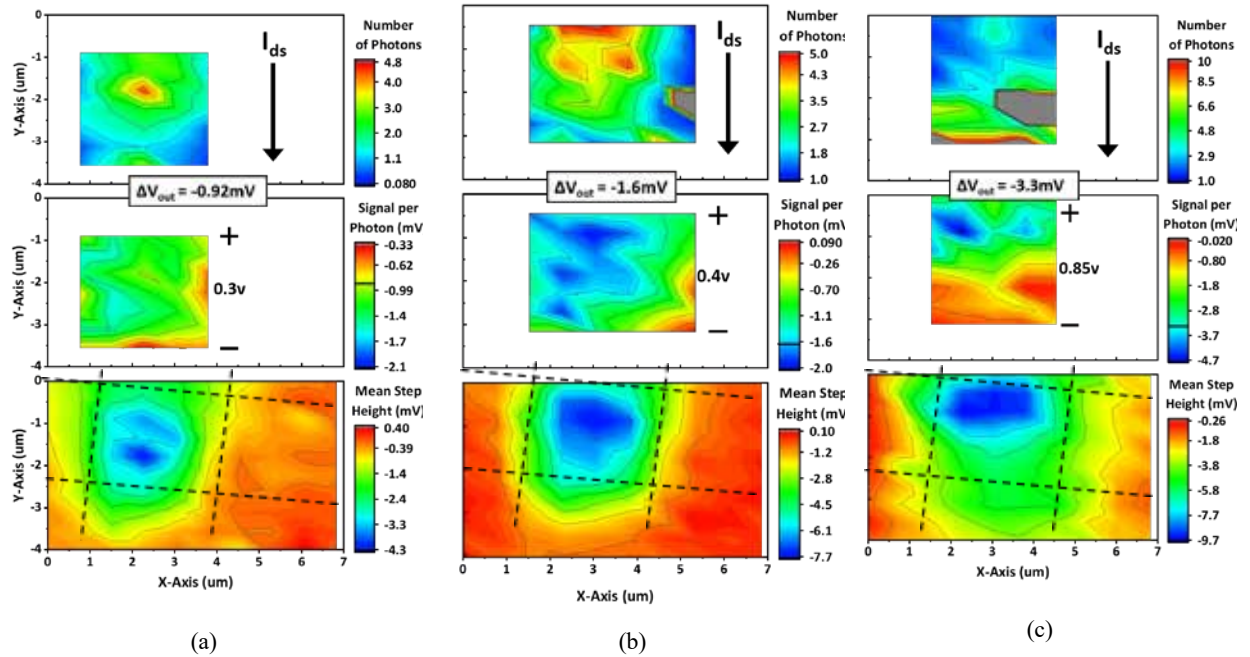


**FIGURE 4.** Contour plots of the MSH (bottom), MSP (middle), and MNP (top) for  $V_{BP} = +2V$  and (a)  $V_g = -0.1 V$ , (b)  $V_g = -0.5V$ , and (c)  $V_g = -1.5V$ . The signal per photon ( $\Delta V_{out}$ ) calculated using the PPC model and Eqn. [1] is provided for comparison. The potential difference between the source and drain contacts is provided in the middle panel.

## CONCLUSIONS

In this work we have spatially resolved the variation in the MSH, MNP, and MSP over the active area of a SIL-capped QDOGFET. We have shown that the observed variation is due to electrical aspects of the device, rather than physical ones and that the gate voltage and current polarity greatly affect these variations. Specifically, the hotspot tends towards the high potential side of the active area, with a larger potential gradient corresponding to a greater shift to that side. The variation in the MNP can be explained in terms of the in-plane transport of the holes, where they tend to drift downstream in the same direction of  $I_{ds}$ . We also see that the MSP is more uniform for smaller gate voltages due to the lower localized potential difference over the active area. This finding is consistent with previous work [3, 4], where lower gate voltages were used when demonstrating the photon-number-resolving capabilities of QDOGFET.

## ACKNOWLEDGEMENTS

We would like to acknowledge M. A. Rowe, S. M. Etzel, T. E. Harvey, and R. P. Mirin who were responsible for the epitaxial growth and fabrication of the structures studied in this work. This material is based upon work supported by the National Science Foundation, USA, under Grant No. 1406665. We would also like to thank the Wisconsin Space Grant Consortium, which provided funding through their Seed Grant.

## REFERENCES

1. M.A. Rowe, E.J. Gansen, M. Greene, R.H. Hadfield, T.E. Harvey, M.Y. Su, S.W. Nam, and R.P. Mirin, Appl. Phys. Lett. **89**, 253505 (2006).

2. E.J. Gansen, M.A. Rowe, M.B. Greene, D. Rosenberg, T.E. Harvey, M.Y. Su, R.H. Hadfield, S.W. Nam and R.P. Mirin, *IEEE. J. Sel. Topics Quantum Electron*, **13**, 1-11 (2007).
3. E.J. Gansen, M.A. Rowe, M.B. Greene, D. Rosenberg, T.E. Harvey, M.Y. Su, R.H. Hadfield, S.W. Nam and R.P. Mirin, *Nature Photonics* **1**, 585-588 (2007).
4. M.A. Rowe, E.J. Gansen, M.B. Greene, D. Rosenberg, T.E. Harvey, M.Y. Su, R.H. Hadfield, S.W. Nam, and R.P. Mirin, *J. Vac. Sci. Technol. B* **26**, 1174-1177 (2008).
5. M.A. Rowe, G.M. Salley, E.J. Gansen, S.M. Etzel, S.W. Nam, and R.P. Mirin, *J. Appl. Phys.* **107**, 63110 (2010).
6. E.J. Gansen, M.A. Rowe, S.D. Harrington, J.M. Nehls, S.M. Etzel, S.W. Nam and R.P. Mirin, *J. Appl. Phys.* **114**, 93103 (2013).
7. A. Rose, *Concepts in Photoconductivity and Allied Problems* (Interscience, New York, 1963), ch. 1.
8. G. Yusa and H. Sakaki, *Electron. Lett.* **32**, 491-493 (1996).

# phys con

2022 Physics Congress

## Plenary speakers



**Julianne Pollard-Larkin**  
MD Anderson Cancer  
Center



**K. Renee Horton**  
NASA



**Rush Holt Jr.**  
former CEO of AAAS



**Sarah Hörst**  
Johns Hopkins  
University

## Special Centennial Speakers

Eric Cornell | Jim Gates | Jocelyn Bell-Burnell | John Mather



[sigmapisigma.org/congress/2022](https://sigmapisigma.org/congress/2022)





# Nitrogen Beams with a National Electrostatics Corporation Alphasource and a 5SDH Accelerator

B. Harlow,<sup>1, a)</sup> P. A. DeYoung,<sup>1, b)</sup> and V. A. Bunnell<sup>1</sup>

<sup>1</sup>*Hope College Department of Physics, Holland, MI 49423, USA*

<sup>a)</sup>Corresponding author: [blake.harlow@hope.edu](mailto:blake.harlow@hope.edu)

<sup>b)</sup>[deyoung@hope.edu](mailto:deyoung@hope.edu)

**Abstract.** Over the past 15 years, Hope College has been producing hydrogen and helium ion beams with an Alphasource<sup>®</sup> ion source and 5SDH Pelletron<sup>®</sup> tandem Van de Graaff accelerator. The manufacturer stated the possibility of creating nitrogen ions from this source, but Hope College has not, up until now, attempted to do so. By mixing approximately 1% nitrogen into hydrogen source gas, imidogen (NH<sup>+</sup>) and amidogen (NH<sub>2</sub><sup>+</sup>) ions are created and accelerated through the tandem accelerator. Oxygen and hydroxide beams are also present due to residual water vapor in the source after maintenance. Post acceleration, these ion beams were directed into a scattering chamber by a dipole bending magnet for identification. Alternate beams such as these open up new possibilities for future experiments such as nitrogen implantation.

## INTRODUCTION

Hope College has an Alphasource<sup>®</sup> ion source<sup>1</sup> paired with a 5SDH Pelletron<sup>®</sup> tandem Van de Graff Accelerator<sup>2</sup>. The Alphasource<sup>®</sup> ion source is a charge-exchange type source and is marketed and used as a source for negative H and He ions. Many of these sources are in operation around the world because they are a reliable technology for the production of He<sup>-</sup> ions, not available from sputter sources, for acceleration by tandem accelerators<sup>3</sup>.

The manufacturer of this ion source, National Electrostatics Corporation<sup>4</sup>, and Ref. 5 state there is a possibility of creating imidogen (NH<sup>+</sup>), oxygen, and hydroxide (OH<sup>+</sup>) ions with this ion source. Amidogen (NH<sub>2</sub><sup>+</sup>) ions could potentially be made, but N<sup>+</sup> ions are unexpected because the ground state electron configuration of this ion is unstable.<sup>6</sup> However, very little exact information about finding and optimizing these alternate beams is given. The process necessary to make these alternate beams was studied. Source gas changes were necessary and a model for the bending magnet was created assuming non-relativistic particles. Although the paths through the beam line are very complex, the underlying principle for the model is that all particles with the same value of  $mv/qB$  will take the same path through the focusing and bending magnets. Sample ion source and accelerator settings for various beam species have been found for various beam energies and ions. The magnet current required to bend these beams can be consistently predicted using the model which confirms the identity of each beam. These beams have the potential for being used for nitrogen implantation.

## ACCELERATOR DESCRIPTION

The current accelerator at Hope College was installed in 2004.<sup>7,8</sup> Fig. 1 shows a layout of the installation. An Alphasource<sup>®</sup> ion source creates a plasma using an RF electric field and a magnetic field. Ions are extracted with an axial electric field (probe). The positive ions from the plasma undergo charge exchange as they pass through gaseous rubidium.<sup>1,3</sup> Between the ion source and the low energy entrance to the accelerator, the now negative ions are focused and steered. The focusing and steering elements include a velocity selector (crossed electric and

magnetic field), a vertical electrostatic steerer, and an electrostatic Einzel lens. An insertable Faraday cup is used to measure the low energy beam current. While different ions such as  $\text{NH}^-$  and  $\text{NH}_2^-$  will have different speeds and only one will follow the central path through the accelerator, the low-energy Faraday cup cannot distinguish these two ions. The same is true for  $\text{O}^-$  and  $\text{OH}^-$  ions. The two velocities are very close and since the Faraday cup is close to the velocity selector, the two species are not significantly separate in space when they reach the cup.

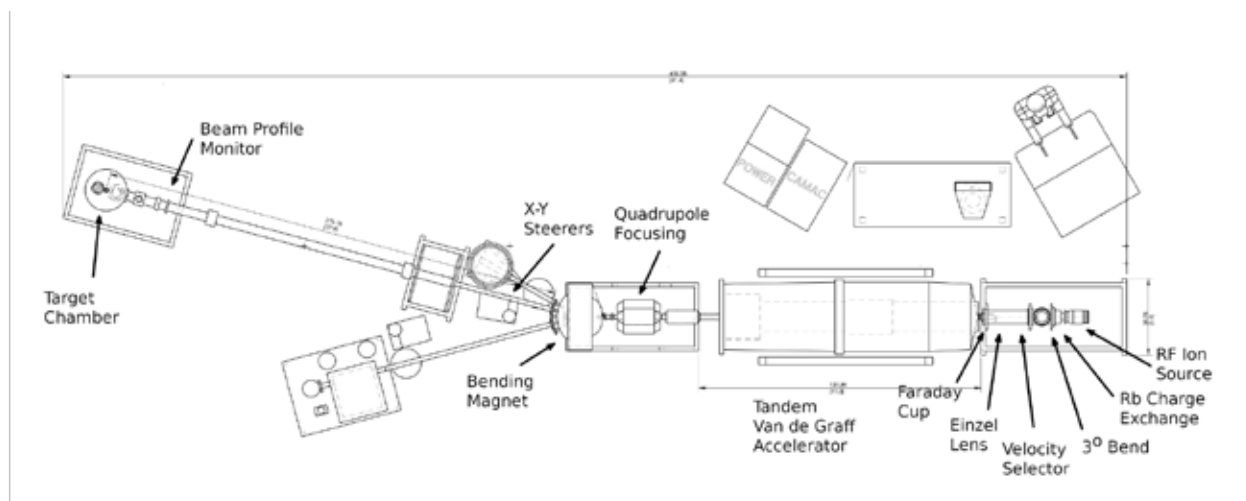


**FIGURE 1.** Layout of the accelerator and associated components.

The tandem Van de Graaff accelerator has a maximum Terminal Voltage ( $TV$ ) of 1.7 MV. The ions are first accelerated by the positive  $TV$  toward the center of the accelerator gaining energy. Electrons are then stripped off during collisions with low pressure nitrogen gas in the center of the tandem leaving a positive ion which is repelled by the  $TV$  gaining additional energy. Ions will have a total energy that depends on the  $TV$  and Charge State ( $CS$ ) of the ion after undergoing stripping in the terminal of the accelerator according to  $E \approx TV + TV * CS$ . This expression is approximate because the ions always have some initial energy from the ion source. Additionally, in those cases where the source produces a molecular ion rather than a simple atomic ion, the expression is even less exact because it does not recognize that the ion has a different mass before and after charge exchange in the center of the accelerator. In general, hydrogen beams will have a maximum energy of  $\sim 3.4$  MeV, and  $\alpha$  particles ( $\text{He}^{2+}$ ) have a maximum energy of  $\sim 5.1$  MeV.

After the accelerator, the beam is directed down a beam line which includes an x and y quadrupole-doublet focusing magnet and a dipole bending magnet. The dipole magnet deflects the beam by  $15^\circ$  into a scattering chamber  $\sim 7.2$  m downstream. The x and y magnetic steering magnets on this line were only varied when the particular species and charge state were changed to minimize perturbations to the path. A beam profile monitor is positioned immediately before the scattering chamber and is used to ensure a consistent beam position and shape regardless of beam species and energy. The scattering chamber is equipped with a Faraday cup to measure beam current, and the current in this cup was maximized at each setting to fine tune the beam line settings.

## MODELING ION BEAM BEHAVIOR

Approximate ion source settings for imidogen ( $\text{NH}^-$ ) are given by the Alphatross manufacturer, but there is only limited documentation regarding specifics. There is little information about exactly what is extracted from the ion source. Specifically, does the source produce atomic nitrogen  $\text{N}^-$  (unexpected because the extra electron is unbound), molecular  $\text{NH}$ , molecular  $\text{NH}_2$ , or a combination? In principle, the current in the dipole bending magnet is a sensitive indicator of the energy and species of the accelerated ion. Thus, the main challenge of finding and identifying alternate beams is the need to accurately model the bending magnet behavior.

In general, the behavior of the dipole magnet can be modeled based on Eq. 1,

$$r = \frac{mv}{qB} = K \sqrt{\frac{mE}{q^2 I^2}}, \quad (1)$$

where  $m$  is the ion mass,  $v$  is the ion velocity,  $q$  is the charge of the ion, and  $B$  is the magnetic field in the magnet. Note that, as is frequently the case, the magnetic field is not known, but rather it is the current through the magnet that is known. The goal is to establish a constant path through the bending magnet and then calibrate the current in the magnet with well known ion species and energies.

Eq. 1 can also be cast in terms of  $E$ , the total kinetic energy of the ion,  $I$ , the current in the magnet coils, and  $K$ , a proportionality constant. The proportionality constant is not known because the field for the actual magnet has not been mapped to establish a relationship between the current and the field. However, if ions are constrained to always follow the same path through the magnet, the current needed to bend a reference ion with radius  $r_0$  can be related to the current needed for any other ion following radius  $r$  according to Eq. 2.

$$r_0 = r \Rightarrow \sqrt{\frac{m_0 E_0}{q_0^2}} I_0 = \sqrt{\frac{mE}{q^2}} I \quad (2)$$

This can be rearranged as shown in Eq. 3 to predict the appropriate  $I$  for any ion given a current  $I_0$  for a specific ion with  $m_0$ ,  $q_0$ , and  $E_0$  that follows a central path.

$$\frac{I}{I_0} = \frac{q_0}{q} \sqrt{\frac{mE}{E_0 m_0}} \quad (3)$$

The process of determining the proportionality constant began with a well-understood reference beam, Hydrogen at  $2.513 \pm 0.020$  MeV. Eq. 3 then gives approximate current values for beams of He and O. If the measured currents are plotted versus  $\frac{Em}{q^2}$ , the current should show a  $y = a + b\sqrt{x}$  behavior. The offset term was included to account for an offset in the current readback from the power supply versus the actual field in the magnet coils.

There is one final consideration that is necessary. When the species leaving the ion source are molecular ions such as imidogen (NH) or hydroxide (OH), these molecules will dissociate in the center of the terminal. In these cases, the energy gained during transit through the accelerator is more complicated because the molecule dissociates when stripping in the terminal takes place. The result is that the final energy of a particle is

$$E_{final} = \frac{m}{M} (|q_i| V_{terminal} + E_{source}) + q_f V_{terminal} \quad (4)$$

where  $q_i$  is the charge of the ion extracted from the the source,  $q_f$  is the charge after stripping,  $m$  is the mass of the species exiting the accelerator and traversing the magnet and  $M$  is the mass of the molecule produced in the ion source. The final energies listed in Table I do include the energy given the ions by the extraction voltage in the ion source and the overall bias voltage applied to the source ( $E_{source}$ ). In this study, no attempt was made to relate measurements to a theory of the dissociation of fast molecular species in matter. There is some theoretical understanding of the dissociation process given in Refs. 9 and 10.

## MEASUREMENTS

The bending magnet current for various ions with various charge states and total kinetic energies (various terminal voltages) was adjusted for maximum beam current in the scattering chamber Faraday cup. A summary list of combinations measured is given in Table 1.

The beam-line steerers and the quadrupole doublet focusing magnet were left constant through the range in order to prevent skewing the data by introducing a different path for the particles. A beam profile monitor and a Faraday cup in the downstream scattering chamber were used to find the bending magnet current that gave the maximum beam. The beam profile monitor allowed one to get close to the desired beam location since this visual aid is easier to use and insured that the trajectory was not somehow skewed.

The optimal magnet current and the beam kinetic energy have some uncertainty. The statistical uncertainty in the magnet current was taken to be 0.05 A and reflects the inability of the accelerator operator to find the absolute best setting given the inherent fluctuations in beam current. This uncertainty is smaller than the symbols in the figures shown and discussed below. There is also a systematic uncertainty due to the calibration of the generating voltmeter. This uncertainty is estimated to be  $\pm 20$  keV and arises because the GVM calibration is done infrequently.

The large dipole bending magnet is subject to hysteresis effects. If hysteresis is ignored when magnet adjustments are made during beam tuning, the relationship between the expected setting and actual setting becomes too imprecise. The size of this effect is shown in Fig. 2. All the measurements presented in the next section were made in a way where the magnet current was always only increased. If the magnet current needed to be reduced, it was turned back to zero before being increased again. Great care was taken when tuning for maximum beam to increase the current in small steps so as not to overshoot the correct current for maximum beam.

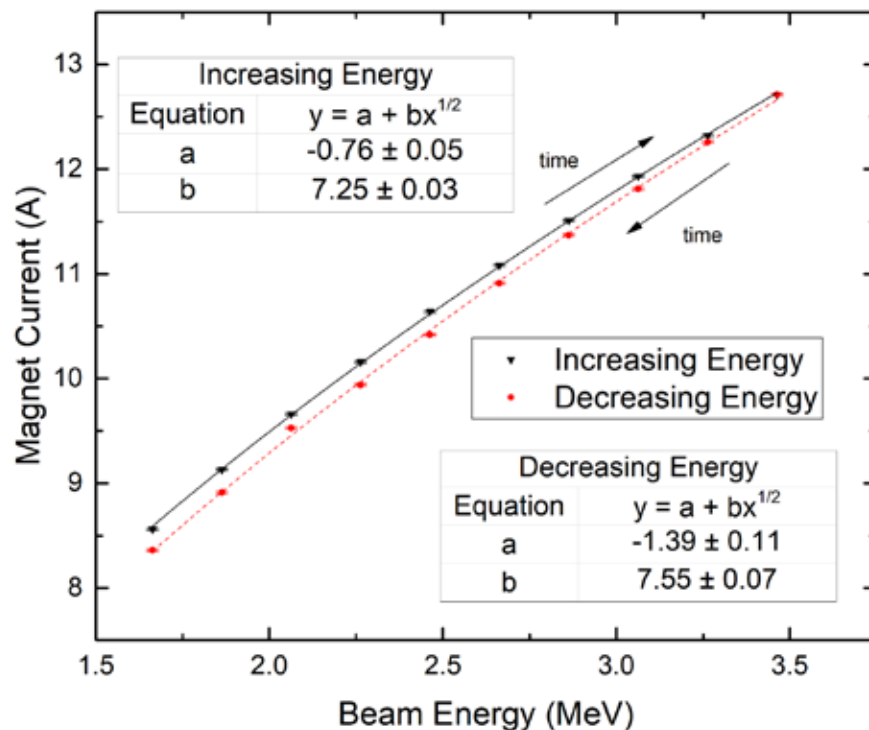


**FIGURE 2.** Hysteresis in the dipole bending magnet. The solid black line indicates magnet current with increasing energy and the red dotted curve was measured with decreasing steps. (Color on-line)

## RESULTS

The goal of this work was to conclusively identify ion beams, especially nitrogen, imidogen, and amidogen from the Alphasource® ion source and transport the resulting beam to the scattering chamber with a usable intensity ( $>0.3$  nA in the scattering chamber). In order to definitively identify the ions, especially those associated with molecules, the systematics of the transport needed to be well understood.

Various combinations of different ions from the ion source, accelerating potentials, and final charge states were directed into the end-station Faraday cup and the magnet current was recorded. Table 1 and Fig. 3 summarize the various combinations that were conclusively identified.

Starting with the  $H^+$  ions of various energies, a preliminary relationship between the magnet current and the parameter  $\frac{Em}{q^2}$  was established. The data set was extended to include  $He^+$  and  $He^{2+}$  ions of differing energies and final charge states with confidence based on the manufacturer's stated settings in the source operations manual. The relationship was refined and next  $O^+$ ,  $O^{2+}$ , and  $O^{3+}$  ions (from atomic O from the source) were added to the data set. The current versus  $\frac{Em}{q^2}$  relationship predicted the currents for various final energies and final charge states with

**TABLE 1.** A summary of the various ion, charge state, and kinetic energy from this investigation. In those cases where a range of energies is given, the typical step size in the accelerator terminal voltage was 100 keV. Also given is the  $\frac{Em}{q^2}$  factor from Eq.2 that is necessary to compare the currents for diverse ions.

Post-source	Final Beam	Final Energy (MeV)	$Em/q^2$ (MeV $\times$ A/ $Z^2$ )	Magnet Current (A)
H <sup>-</sup>	H <sup>+</sup>	1.67-3.53	1.67-3.53	8.56-12.71
He <sup>-</sup>	He <sup>+</sup>	1.68-3.33	6.71-13.33	17.41-24.79
	He <sup>2+</sup>	2.51-5.30	2.51-5.30	10.58-15.60
NH <sup>-</sup>	N <sup>+</sup>	2.01-3.01	29.15-42.18	36.28-44.26
	N <sup>2+</sup>	3.65	12.79	24.19
	N <sup>3+</sup>	4.89	7.62	18.59
NH <sub>2</sub> <sup>-</sup>	N <sup>+</sup>	1.95-2.92	27.34-40.91	35.58-44.37
	N <sup>2+</sup>	3.58	12.54	23.91
O <sup>-</sup>	O <sup>+</sup>	2.50	39.93	43.73
	O <sup>2+</sup>	2.50-5.29	9.98-21.15	21.24-31.44
	O <sup>3+</sup>	3.23-7.05	5.91-12.53	16.31-24.05
OH <sup>-</sup>	O <sup>+</sup>	2.42	38.76	43.02
	O <sup>2+</sup>	2.45-5.18	9.79-20.74	21.01-31.12
	O <sup>3+</sup>	3.27-6.94	5.28-12.34	16.13-23.85

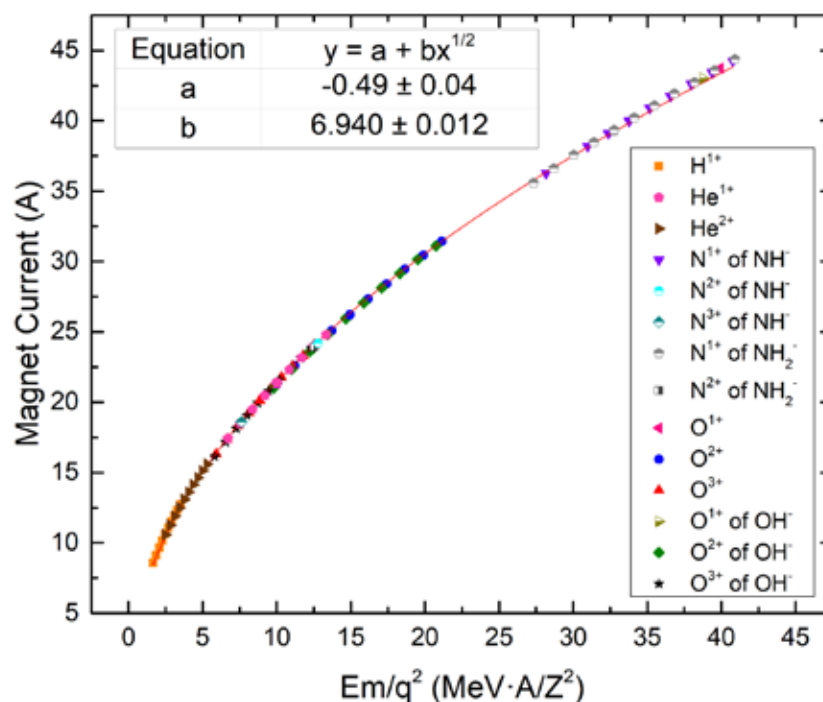


**FIGURE 3.** Current in the dipole bending magnet for various beams species. The legend shows the variety of initial and final ions, charge states, and molecular species. The x axis,  $\frac{Em}{q^2}$ , was chosen to account for the obvious main dependencies on mass and charge state allowing all the data to be presented on a single plot. Statistical uncertainties are smaller than the symbol size. (Color online)



reasonable accuracy and the actual measurements were added to the data set. Next, nitrogen ions ( $N^+$ ,  $N^{2+}$ , and  $N^{3+}$ ) from source ions of imidogen ( $NH^+$ ) were predicted (Eq. 4) and measured with good accuracy. At this point, weaker beams of N and O from molecular source ions of amidogen ( $NH_2^+$ ) and hydroxide ( $OH^+$ ) were predicted and measured. No appreciable amount of  $N^-$  from the ion source was observed. The final relationship was fit as shown in Fig. 3. The excellent agreement between data and the overall model indicates that usable N beams were produced, accelerated, and properly identified.

Specific ion source settings are given in Table 2. For He measurements, standard He was used as the source gas.

**TABLE 2.** Ion source settings for the variety of species produced by the ion source.

Ion Species	Source Magnet Current (A)	Probe Voltage (kV)	Bias Voltage (kV)
H <sup>+</sup> , NH <sup>+</sup> , NH <sub>2</sub> <sup>+</sup> , O <sup>+</sup> , OH <sup>+</sup>	4.00	3.00	10.28
He <sup>+</sup>	4.00	6.00	17.75

For all other cases, the source gas was 1% nitrogen gas added to the normal hydrogen source gas. The impact of varying this ratio was not investigated. This small admixture of N did not noticeably change the performance of the source when extracting H. It was unnecessary to add oxygen since residual oxygen is prevalent enough in the system simply from oxygen and water vapor introduced into the source when maintenance is done. (The leak rate is low enough that the oxygen beams decrease significantly in intensity during the weeks following source openings.) NEC recommends an aluminum canal for the production of hydrogen ions and the same canal was in place when extracting imidogen and amidogen from the source. It was necessary to adjust the velocity selector, located between the ion source and accelerator, to find maximum beam each time a different species was being extracted from the source. Additionally, a vertical steerer and Einzel lens (also located between the source and accelerator) were adjusted but required only minimal changes. The values of the other source parameters are given in Table 2. The source gas pressure set to the nominal value given by the manufacturer in all cases,  $\sim 3 \times 10^{-6}$  Torr.

## CONCLUSION

The ion species imidogen ( $NH^+$ ), amidogen ( $NH_2^+$ ), O<sup>+</sup>, and hydroxide ( $OH^+$ ) species were produced using an NEC Alphasource charge exchange source by incorporating 1% nitrogen into the hydrogen feed gas. Imidogen, amidogen, and hydroxide molecules dissociate in the center of the accelerator terminal in the gas stripper. Atomic N<sup>+</sup> ions were not produced at a detectable level as expected.

The measurements are well described by the assumed mathematical model. Additionally, hysteresis was taken into account and analyzed for the dipole bending magnet. These beams have the potential for nitrogen implantation and creating nitrogen vacancies in diamond and other crystalline materials.

## ACKNOWLEDGEMENTS

The authors thank Dave Daugherty for his commitment to successful operation of the accelerator. This work was funded through support from the National Science Foundation under grants MRI-0319523 and RUI-PHY-1911418.

## REFERENCES

1. Alphasource Source RF-Charge Exchange Ion Source, <https://www.pelletron.com/wp-content/uploads/2017/02/Alphasource-v1.pdf>.
2. Complete Pelletron Systems for Ion Beam Analysis, <https://www.pelletron.com/wp-content/uploads/2016/09/COMPLETE-IBA-SYSTEM-Handout.pdf>.
3. R. Middleton, Nuclear Instruments and Methods in Physics Research **A122**, 35-43 (1974).
4. National Electrostatics Corporation, 7540 Graber Road, P.O. Box 620310, Middleton, WI 53562, USA. [nec@pelletron.com](mailto:nec@pelletron.com). (608) 831-7600.

5. R.J. Ward, G.M. Brown, D. Ho, B.F.O.F. Stockler, C.G. Freeman, S.J. Padalino, and S.P. Regan, CEU poster JP10.00019, 58th Annual Meeting of the APS Division of Plasma Physics, San Jose, CA, USA (2016).
6. H. Hotop and W. C. Lineberger, Journal of Physical Chemistry Reference Data **14**, 732-741 (1985).
7. G. F. Peaslee, and P. A. DeYoung, SM/AE-02, International Topical Meeting on Nuclear Research Applications and Utilization of Accelerators: 4-8 May, Vienna (2009).
8. A. Pena, P. A. DeYoung, and G. F. Peaslee, Poster CK.057, American Physical Society, Division of Nuclear Physics Meeting, Chicago, IL, United States (2004).
9. D. Gemmell, Nucl. Instrum. Methods **179**, 41-56 (1980)
10. J. Remillieux, Nucl. Instrum. Methods **179**, 31-40 (1980).

**phys  
con**  
2022 Physics Congress

### Special Centennial Speakers

Eric Cornell | Jim Gates | Jocelyn Bell-Burnell | John Mather

### Events

- 5 Plenary sessions
- Tours: Green Bank Observatory, National Labs around DC, GWU, UMD, Smithsonian and more
- 15+ workshops
- Poster Session & Physics Fine Art Exhibit and Competition
- Career Expo Chapter Showcase
- Grad School Fair
- High Energy Hot Chocolate and Game Night
- Astronomy Night at GWU
- Chapter showcase
- Dance Party & Physics Phestival



**AIP**  
American Institute  
of Physics

[sigmapisigma.org/congress/2022](https://sigmapisigma.org/congress/2022)



# Demonstrating the Sagnac Effect Using Tabletop Optics on a Rotary Platform

Jonathan Mock,<sup>1, a)</sup> Jared Medlin,<sup>1, b)</sup> Matthew Richards<sup>1, c)</sup>  
and Edward Hamilton<sup>1, d)</sup>

<sup>1</sup>*LeTourneau University, 2100 S Mobberly Ave, Longview, TX 75602, USA*

<sup>a)</sup>Corresponding Author: JonathanMock@LeTU.edu

<sup>b)</sup>JaredMedlin@LeTU.edu

<sup>c)</sup>MatthewRichards@LeTU.edu

<sup>d)</sup>EdwardHamilton@LeTU.edu

**Abstract.** A Sagnac interferometer splits an incident beam of light into two components which travel in opposite directions of the same path. Consequently, each beam travels an equivalent distance. However, by rotating the entire apparatus at a sufficient speed, a noticeable change in the beams' interference pattern is observed. This pattern results from one beam travelling against rotation and the other travelling with rotation, resulting in an increase or decrease in apparent path length, respectively. This is known as the Sagnac Effect. By using a traditional mirror-and-laser interferometer setup and a large turntable, we demonstrate the Sagnac Effect by showing that a given angular velocity results in a phase shift which matches what is predicted.

## INTRODUCTION

When first learning about the consequences of relativity, it is useful to understand the experiments which led to its inevitable acceptance. A major cornerstone in this history is the initial hypothesis of a luminous ether with its eventual rejection. While the Michelson-Morley experiment is frequently demonstrated at the undergraduate level, the Sagnac effect also provides powerful evidence for a lack of an ether (even without addressing relativity). This paper intends to demonstrate an undergraduate experiment with a Sagnac interferometer alongside the interpretations which can be drawn from such experimentation.

In the 19<sup>th</sup> century, Maxwell's formulations of electromagnetic theory alongside Young and Fresnel's revival of Huygens' light wave propagation theory created the working assumption that there must be an ether through which electromagnetic waves propagate.<sup>1</sup> Experiments such as the Michelson-Morley and Sagnac interferometers were developed to measure the speed of the hypothesized ether relative to the Earth. When Michelson and Morley failed to find a nonzero speed measurement for the ether, an alternative hypothesis was proposed that the Earth drags the ether (and so the ether would appear stagnant to the Earth).<sup>2</sup> While Michelson and Morley found unpredicted results, Georges Sagnac successfully demonstrated his predicted "optical rotation effect" and believed it to be a "direct observation of the luminous ether."<sup>3</sup> One of the underlying assumptions to the Sagnac's calculations, however, is that the ether is not dragged along by the interferometer.<sup>3,4</sup> The Sagnac experiment together with the Michelson-Morley experiment poses a contradiction: the ether must not be dragged to produce the positive result in the Sagnac interferometer, but it simultaneously needs to be dragged to produce the null result in the Michelson-Morley interferometer.<sup>5</sup> These experiments alongside several others have failed to provide evidence for an ether; henceforth, the current belief is that light does not require a medium.<sup>2</sup>

Beyond its applicability in refuting the ether, the Sagnac effect is widely used in navigational systems and sensory technologies. Ring laser gyroscopes use a system of mirrors to create a common path for light to travel around (this is closely comparable to the Sagnac interferometer created in this experiment) while fiber optic gyroscopes control the path of light with fiber optic cables.<sup>6</sup> Placing three gyroscopes orthogonal to each other allows for measurements in all three degrees of freedom for a navigation system.<sup>6</sup> The Sagnac effect is also used in fiber optic current sensors. Optic current sensors are not influenced by electromagnetic interference, and so they are advantageous in high power systems.<sup>7</sup> These fiber optic sensors are also sensitive to birefringence effects from temperature and vibrations; current research is investigating how to use this birefringence for sensory applications.<sup>8,9</sup>

In 1921, Paul Langevin provided the first interpretation of the Sagnac effect from general relativity.<sup>10</sup> His derivations<sup>10</sup> for a rotating Sagnac interferometer find the propagation time difference between the counterpropagating waves to be:

$$\Delta t = \frac{4A\omega}{c^2} . \quad (1)$$

The area inside the beam path is given as “A”, and the difference of time traveled is “ $\Delta t$ .” In the following, let  $N$  be the number of fringes that pass by.

$$\Delta\phi = 2\pi\Delta N = 2\pi(f * \Delta t) = 2\pi * \frac{c}{\lambda} * \frac{4A\omega}{c^2} = \frac{8\pi\omega A}{c\lambda} \quad (2)$$

$$\therefore \Delta\phi = \frac{8\pi\omega A}{c\lambda} \quad (3)$$

The above relationship gives the phase difference as a function of angular velocity.

## THE EXPERIMENT

To demonstrate the Sagnac effect, this experiment uses TeachSpin’s Sagnac interferometer.<sup>11</sup> The basic layout of the interferometer is shown in Figure 1(a). A polarizing beam-splitter cube (PBSC) separates an incident 45°-linearly polarized beam into two equal-power, orthogonal  $p$ -state beams. Each beam traverses the loop in opposing directions and rejoins at the original PBSC. These component beams are split again (not shown in figure) and sent into two separate photodetectors to allow for further analysis. The breadboard the interferometer is built upon has urethane pads at each corner to reduce ambient vibrations and stiffening beams to reduce the possibility of the breadboard deformation, both of which can distort the final images of the beams.

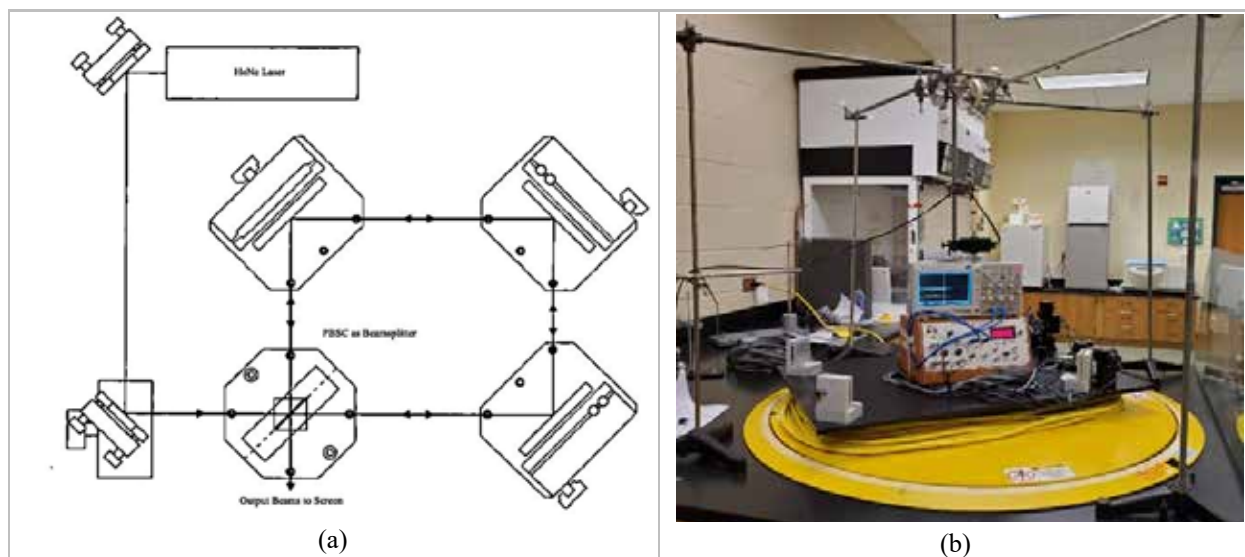


**FIGURE 1:** (a) Sagnac interferometer design detailed by TeachSpin.<sup>11</sup> (b) Apparatus utilized in experiment.

This interferometer can detect shifts in the thousandths of a fringe according to TeachSpin.<sup>2</sup> Introducing motion such as rotation of the apparatus results in wobbling and stray air currents which cause shifts that exceed this value; around one to two-thousandths of a fringe depending on speed. The Sagnac effect, summarized mathematically in Equation 3, will not exceed this value at lower angular velocities and smaller areas and will be indistinguishable

from it. With a small area of  $0.274 \text{ m}^2$  and a wavelength of  $633 \text{ nm}$  but a high angular velocity of  $2.75 \text{ rad/s}$  the calculated shift from the Sagnac effect is one hundredth of a fringe; one magnitude higher than the shifts from other effects and enough to clearly demonstrate the Sagnac effect in action.

The combination of the interferometer's weight, size, and required angular velocity require the use of an industrial turntable. It offers the ability to rotate at high speeds and can support any weight within the scope of this experiment. A Vernier angular velocity detector which is mounted above the center of the turntable and fixed so that the turntable will turn the disk in the detector, providing for reliable measurements of  $\omega$ . This detector is capable of measurements with a precision of  $0.109 \text{ rad/s}$ . Two photodetectors measure the relative intensity of the two beams after they undergo the Sagnac effect. The laser's electronics box (supplied by TeachSpin) supplies power to the laser and the photodetectors. An oscilloscope will record the signals from the photodetectors. The final apparatus is shown in Figure 1(b).

The laser is run for thirty minutes before running trials to minimize power fluctuations resulting from increasing temperatures. Each trial runs for twenty seconds. The first five seconds are for measuring the voltages of each photodetector's signal while the interferometer is stationary. The remaining fifteen seconds involve measuring these voltages while the interferometer rotates at various velocities. Each run is then analyzed by the methodology below.

The rotational phase difference is the difference of each photodetector's output voltage while the system rotates. Note that this value changes as rotational velocity changes. The sum of these two voltages is the total output voltage of the original beam. The rotational phase difference divided by the total original output voltage determines the phase shift. These values are then averaged across all trials at each increment of velocity. The results of this are summarized in Table 1 (only a limited range is shown). Figure 2 shows all the velocity data compared to the predicted change.

**TABLE 1:** Angular Velocity vs Phase Shift  
(Range  $1.4180 \text{ rad/s}$  to  $2.9450 \text{ rad/s}$ ).

Velocity	Measured Change	Theoretical Change	Percent Error
1.4180	0.0538	0.0515	-4.5099
1.5270	0.0569	0.0555	-2.5968
1.6360	0.0616	0.0594	-3.7406
1.7450	0.0586	0.0634	7.4958
1.8540	0.0625	0.0673	7.1763
1.9630	0.0660	0.0713	7.4747
2.0730	0.0698	0.0753	7.2578
2.1820	0.0739	0.0792	6.7110
2.2910	0.0752	0.0832	9.6687
2.4000	0.0838	0.0872	3.8539
2.5090	0.0833	0.0911	8.6061
2.6180	0.0872	0.0951	8.3249
2.7270	0.0899	0.0990	9.2450
2.8360	0.0931	0.1030	9.6303
2.9450	0.0976	0.1069	8.7086

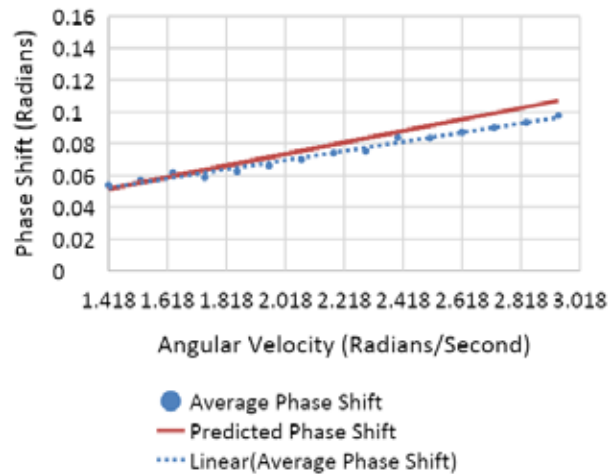


**FIGURE 2:** Predicted Change vs Measured Change vs Angular Velocity.

This data is correlated with predicted values in ranges  $1 \text{ rad/s}$  to  $3 \text{ rad/s}$  due to the relatively low effect of signal disturbance compared to the Sagnac effect. An angular velocity above or below these bounds results in a Sagnac effect that is too low to be meaningfully distinguished from experimental sources of distortion such as vibration or air currents, particularly at higher velocities. Therefore, for regions where the angular velocity is between  $1 \text{ rad/s}$  and  $3 \text{ rad/s}$  the correlation with the predicted effect offers strong evidence for the Sagnac effect.

## CONCLUSION

A noticeable correlation of the measured phase shift to the Sagnac effect is observed. Individual data points and tests varied from expected values due to experimental errors, but more data points mitigated these deviations. Due to the nature of interferometry, reducing outside and systematic interference is the largest challenge of this experiment;



things as small as vibrations from a refrigerator across the room created noticeable shifts in data. In future experiments of this type, it is recommended to consider alternative setups that would reduce the effect of outside interference as well as mitigate risk to the equipment if higher rotational speeds are desired. Despite these limitations, this experiment adequately shows the lack of an ether through the no-ether Sagnac effect applying to the data. We encourage the use of this experiment in undergraduate laboratories to deepen each student's understanding of the historical breakthrough that shaped how physics is today.

### ACKNOWLEDGMENTS

This work was supported by a grant from the Welch Foundation. The authors would like to acknowledge TeachSpin for supplementary materials as well as Dr. Edward Hamilton and Dr. Steve Ball for their guidance and mentorship.

### REFERENCES

1. N. Huggett and C. Hoefer, "Absolute and Relational Theories of Space and Motion," in *The Stanford Encyclopedia of Philosophy*, (Metaphysics Research Lab, Stanford, 2018).
2. R. Harris, *Modern Physics* 2<sup>nd</sup> ed (Pearson Addison-Wesley, San Francisco, 2008), pp. 7-8.
3. G. Sagnac, *The Abraham Zelmanov Journal*, **1**, 75 (2008).
4. O. Darrigol, *Comptes Rendus Physique* **15**, 791, 824 (2014).
5. G. B. Malykin and V. I. Pozdnyakova, *Ring Interferometry* (De Gruyter, 2013), pp. 8-13.
6. A. Maini, *Lasers and Optoelectronics: Fundamentals, Devices, and Applications* (John Wiley and Sons Ltd, 2013), pp. 540-549.
7. B. Pal, *Guided Wave Optical Components and Devices: Basic, Technology, and Applications* (Elsevier Academic Press, 2005), pp. 414-416.
8. X. Fu, S. Huang, D. Li, J. Zhang, G. Fu, W. Jin, W. Bi, and Q. Hu, *Optical Fiber Technology*, **61** (2021).
9. D. Meng, C. Miao, X. Li, J. Li, J. Shi, W. Xu, X. Yang, D. Xu, T. Liu, and J. Yao, *Optical Fiber Technology*, **61** (2021).
10. G. Pascoli, *Comptes Rendus Physique*, **18**, 567 (2017).
11. *Modern Interferometry: MII-A Instructor's Manual* (TeachSpin Inc, Buffalo, 2018), pp. 5.1-5.11.

# Test Particle Calculation of Plasma Equilibria

Jonathan Sullivan-Wood<sup>1, a)</sup> and Daniel Holland<sup>1, b)</sup>

<sup>1</sup>*Illinois State University, Department of Physics, Normal, IL 61790-4560, USA*

<sup>a)</sup>Corresponding author: jmsull1@ilstu.edu

<sup>b)</sup>dlhollar@ilstu.edu

**Abstract.** We present a numerical technique for self-consistently calculating plasma equilibria with prescribed sources and sinks on the boundaries, i.e. a scattering system. The method is applied to the earth's magnetotail. The method follows individual particles through a prescribed magnetic field, while calculating the density, current and pressure that the particle contributes on a uniformly spaced grid. The individual particles are weighted to model a given source distribution and the total equilibrium properties, including the resulting magnetic field, are evaluated. The calculated and prescribed magnetic fields are then compared. If the fields differ significantly, the two fields are mixed and the process repeated. Convergence to the self-consistent field typically takes between 100 and 150 iterations.

## INTRODUCTION

Determining the self-consistent properties of a plasma equilibrium is typically a very challenging problem, but is essential for determining the stability and wave properties in the plasma. This is particularly true for cases where the scale length of the variations in the plasma are on the order of the ion gyroradius or smaller. One common method is to choose a distribution function and self-consistently solve the Vlasov-Maxwell equations using moments of the distribution. This technique has produced many useful results,<sup>1-5</sup> however it misses the effects of nonlinear/chaotic particle dynamics on the distribution function and resulting equilibrium and stability. Test particle simulations provide an alternative, in which the fields are assumed to be known and a distribution of particles is launched from a source region and pushed through the given fields.<sup>6-9</sup> Once all the particles in a source distribution have moved through the system, the total average density ( $n$ ), current ( $\mathbf{j}$ ), pressure tensor ( $\mathbf{Q}$ ), are used to update the fields. The process is repeated until the input and calculated fields are in agreement. Test particle codes are well suited for determining equilibrium solutions with good spatial resolution using a relatively small number of particles, but cannot yield any information about the time evolution and stability of the calculated equilibria. The resulting equilibria may be used as initial conditions for Particle-in-Cell simulations that can evaluate the wave and stability properties of the system.

## TEST PARTICLE SIMULATION

A fundamental first step in a test particle code is to compute the contributions of a single particle. This process is complicated by the facts that the particle motion is in general chaotic and that it is not known a priori how long a particle will remain in the calculation region. At any given time, however, the distribution function of a single particle is formally given by

$$f_{sp} = \frac{1}{L^3 \Omega_0} \delta\left(\frac{r-r(t)}{L}\right) \delta\left(\frac{v-v(t)}{\Omega_0 L}\right) \quad (1)$$

where  $L$  is the characteristic scale length and  $\Omega_0$  is the characteristic frequency. The spatial (velocity) delta function is three dimensional so that  $\delta\left[\frac{r-r(t)}{L}\right] = \delta\left[\frac{x-x(t)}{L}\right] \delta\left[\frac{y-y(t)}{L}\right] \delta\left[\frac{z-z(t)}{L}\right]$  and similar for the velocity space

delta function. For our work on the current sheet,  $L$  and  $\Omega_0$  are taken to be the initial scale length of the assumed field and the cyclotron frequency in the asymptotic magnetic field. The first three moments of the distribution (density( $n$ ), current( $j$ ), and pressure ( $Q$ )) are calculated as

$$n(\hat{r}, t) = \int f_{sp}(r, v, t) dv = \frac{1}{L^3} \delta(\hat{r} - \hat{r}(t)) \quad (2)$$

$$j(\hat{r}, t) = q \int v f_{sp}(r, v, t) dv = \frac{q\Omega_0}{L^2} \hat{v} \delta(\hat{r} - \hat{r}(t)) \quad (3)$$

$$Q(\hat{r}, t) = m \int v v f_{sp}(r, v, t) dv = \frac{m\Omega_0^2}{L} \hat{v} \hat{v} \delta(\hat{r} - \hat{r}(t)) . \quad (4)$$

Here  $q$  ( $m$ ) is the charge (mass) of the particle and we have defined the normalized variables  $\hat{r} = r/L$  and  $\hat{v} = v/\Omega_0 L$ . The contribution of a single particle to the equilibrium quantities is obtained by averaging instantaneous values along the trajectory for the time,  $T$ , that the particle is in the system, i.e.

$$\overline{W}(\hat{r}) = \frac{1}{T} \int_0^T W(\hat{r}, t) dt, \quad (5)$$

where  $W$  is any velocity moment ( $n$ ,  $j$ ,  $Q$ ) and in general,  $T$  will be different for each particle. Assuming that we calculate the particle position and velocity at equally space time intervals,  $\Delta t$  so that  $T = N\Delta t$ , we may approximate the integral as a finite sum. Thus

$$\bar{n}(\hat{r}) = \frac{1}{L^3} \left[ \frac{1}{N} \sum_{n=0}^N \delta_{\hat{r}, \hat{r}_n} \right] \quad ; \quad \bar{j}(\hat{r}) = \frac{q\Omega_0}{L^2} \left[ \frac{1}{N} \sum_{n=0}^N \hat{v}_n \delta_{\hat{r}, \hat{r}_n} \right] \quad ; \quad \bar{Q}(\hat{r}) = \frac{m\Omega_0^2}{L} \left[ \frac{1}{N} \sum_{n=0}^N \hat{v}_n \hat{v}_n \delta_{\hat{r}, \hat{r}_n} \right] \quad (6)$$

where  $\hat{r}_n$  ( $\hat{v}_n$ ) is the normalized position (velocity) at the  $n^{\text{th}}$  time step and  $\delta_{\hat{r}, \hat{r}_n}$  is the Kroneker delta function. Since the moments will be interpolated onto a grid, it is important that the time step be chosen sufficiently small so that a particle does not cross a complete grid cell in a single step. The sums in the square brackets are easily calculated by linearly interpolating the values at each step onto the grid points that bound the cell the particle is in during a particular step. An extra (guard) cell adjacent to the calculation region must be included to ensure the proper contributions of the moments to the edge grid points. In principle this process can be applied in 1, 2, or 3 dimensions.

As a particular example of the test particle method, we consider the magnetotail current sheet where we use the GSE coordinate system with its origin in the center of the earth, the x-direction is in the direction of the sun, y is in the dawn to dusk direction and z is normal to the ecliptic. In this system, the magnetic field is given by  $B = B_0 f(z/L) \hat{x} + B_z \hat{z}$  where  $f(z/L)$  is a smoothly varying function that asymptotes to  $\pm 1$  as  $z \rightarrow \pm \infty$ . For the case  $f(z/L) = \tanh(z/L)$ , this is the well-known modified Harris model. The field is taken to only vary in the z-direction, since the scale lengths in x and y are much longer than L.

To calculate the equilibrium profiles, we choose the ion source distribution function in the asymptotic region to be a drifting Maxwellian, i.e

$$f(v) = C e^{-\frac{mv^2}{2T} - \frac{m(v_{\parallel} + v_D)^2}{2T}} \quad (7)$$

where  $C$  is a constant,  $T$  is the ion temperature and  $v_D = \sqrt{\frac{2\varepsilon T}{m}} = \sqrt{\frac{2E_{\text{drift}}}{m}}$  is the drift velocity along the field line given in terms of the fraction,  $\varepsilon$ , of the thermal energy and  $E_{\text{drift}} = \varepsilon T$ . Once a particle has escaped from the system, the single particle moments are weighted such that the density at the top grid point due to that incoming particle is unity to ensure that each particle has equal weight in the phase space. To guarantee that a particle contributes properly to the top grid cell, it is launched two gyro-radii above the guard cell and is considered to have left the system when the absolute value of the z-position reaches a distance of two gyro-radii above the launch point. Once all of the particles have been added together, the total moments are weighted such that the height integrated y-current density produces the proper change in the x-component of the magnetic field given by  $f(z/L)$  (i.e. from -1 to +1). The total calculation may be greatly speeded up if we assume identical particle sources above and below the

current sheet, since we may then use the symmetry of the system to only launch particles from either above or below the current sheet and then reflect the moments across the  $z=0$  plane. As a common first approximation, we assume that the electrons are sufficiently mobile so as to provide a neutralizing background. Non-symmetric sources may be modeled by launching separate distributions from either side of the current sheet.<sup>9</sup> Once a new magnetic field has been calculated, it is compared with the initial field. If the fields are in agreement, we end the simulation, if not, we mix the old and new fields together and calculate a new input field. We typically use 95% old field and 5% new field to ensure convergence, but as a general rule, for smaller drift velocities a smaller percentage of the new field is required.

To convert a calculated equilibrium in code variables into physically meaningful quantities we begin by defining  $L = \sigma R_E$ , where  $R_E$  is the radius of the earth and  $\sigma$  is a constant to be determined. Assuming a proton plasma and using the definitions of the moments above, we find that  $\sigma = 0.036 \sqrt{\left(\frac{\hat{n}_{top}}{n_0}\right)}$ , where  $\hat{n}_{top}$  is the calculated density in the top grid cell and  $n_0$  is the asymptotic particle density measured in  $cm^{-3}$ . Furthermore, the asymptotic magnetic field is given by  $B_0 = 14.1 \sqrt{\frac{n_0 T_0}{\hat{n}_{top} \hat{T}}}$  where  $T_0$  is the ion temperature measured in keV and  $\hat{T}$  is the ion temperature in code variables. The results for the case  $n_0 = 0.35 cm^{-3}$ ,  $T_0 = 5keV$ ,  $E_{drift} = 0.1T_0$  and  $B_z = 0.1B_0$  are shown in Figure 1 (a)-(c). The field looks very much like the Harris-magnetic field, but the density is almost constant throughout the reversal.

In figure 1(d) and (e) we show how the peak in the current density and the scale length of the field reversal vary as a function of the drift energy. Higher drift energies result in more peaked density profiles and thinner sheets. These properties may play an important role in the next phase of the project where we allow for more complex electron models. For example, if the electrons are taken as a Boltzmann distribution, the short scale length and peaked density may result in a significant electric field in the  $z$ -direction that will in turn modify the ion dynamics.

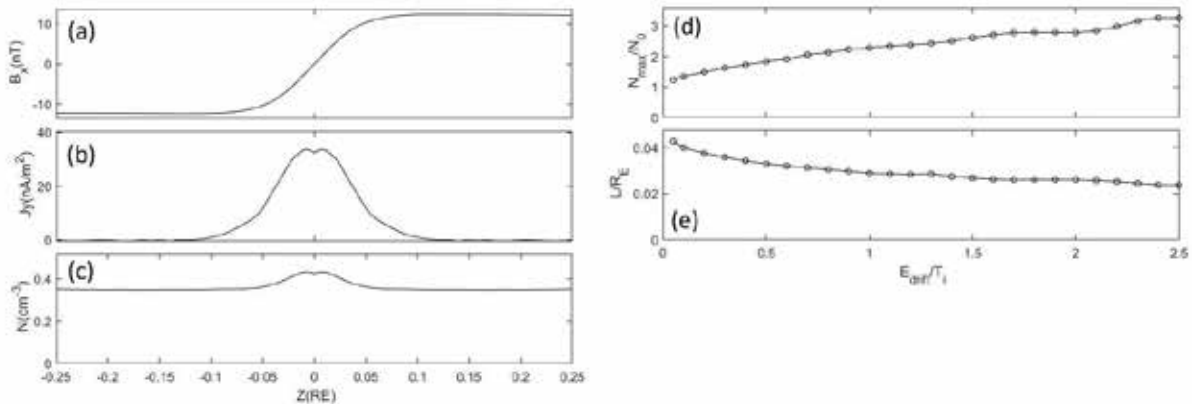


**FIGURE 1.** Example results from the code. (a)-(c) are the self-consistent magnetic field, current density and particle density for the case in which  $n_0 = 0.35 cm^{-3}$ ,  $T_0 = 5keV$ ,  $E_{drift} = 0.1T_0$  and  $B_z = 0.1B_0$ . Frames (d) and (e) show the percentage increase in the peak density and the scale length of the field reversal as a function of the drift energy.

## REFERENCES

1. E.G. Harris, *II Nuevo Cimento* **23**, 115-121 (1962).
2. M.I. Sitnov, L.M. Zelenyi, H.V. Malova, and A.S. Sharma, *J. Geophys. Res.* **105**, 13,029-13,043 (2000).
3. G. Zimbardo, A. Greco, P. Veltri, A.L. Taktakishvili, L. Zelemyi, *Annales Geophys.* **22**, 2541-2546 (2004).
4. M.I. Sitnov, M. Swisdak, P.N. Guzdar and A. Runov, *J. Geophys. Res.* **111**, A08204 (2006).
5. T. Neukirch, F. Wilson, and O. Alanson, *Plasma Phys. Control. Fusion* **60** 014008 (2017).
6. P. L. Pritcherr and F. V. Coroniti, *J. Geophys. Res.* **97**, 16,773-16,787 (1992).
7. G.R. Burkhart, J.F. Drake, P.B. Dusenberry and T.W. Speiser, *Geophys. Res.* **97**, 13799-13815 (1992).
8. D.L. Holland and J. Chen, *Geophys. Res. Lett.* **20** 1775-1778 (1993).
9. J. Harold and J. Chen, *Geophys. Res.* **101**, 24899-24909 (1996).

# PhysiCL: An OpenCL-Accelerated Python Physics Simulator

Benjamin Warner

*Department of Computer Science, Pacific Lutheran University, Tacoma, WA 98447, USA*

<sup>a)</sup>Corresponding author: warnerbc@plu.edu, b.c.warner@wustl.edu

**Abstract.** Numerical methods of physics analysis require specialized forms of programming as well as attention to issues of implementation. PhysiCL is a Python package that aims to provide general-purpose tools for performing OpenCL-accelerated physics simulations with ease. PhysiCL contains a Numpy-based code units system, a set of generic simulation tools, built-in tools for photon scattering, tools for measuring light behavior, and tools for writing new OpenCL-based simulation features. This package can be installed via PyPI using `pip install physiCL`, and found on GitHub with source code and examples at <https://github.com/bcwarner/physicl>.

## INTRODUCTION

PhysiCL is a Python library that utilizes OpenCL to accelerate physics simulations, and it is intended to make writing physics simulations easier for both students and researchers. Currently, the feature set is designed primarily to work with simulations involving light scattering, and future work may expand it beyond this. We shall examine the basic usage of PhysiCL, its OpenCL metaprogramming tools, its code units system, and its base light scattering system.

## FEATURES

### Basic Simulation Operation

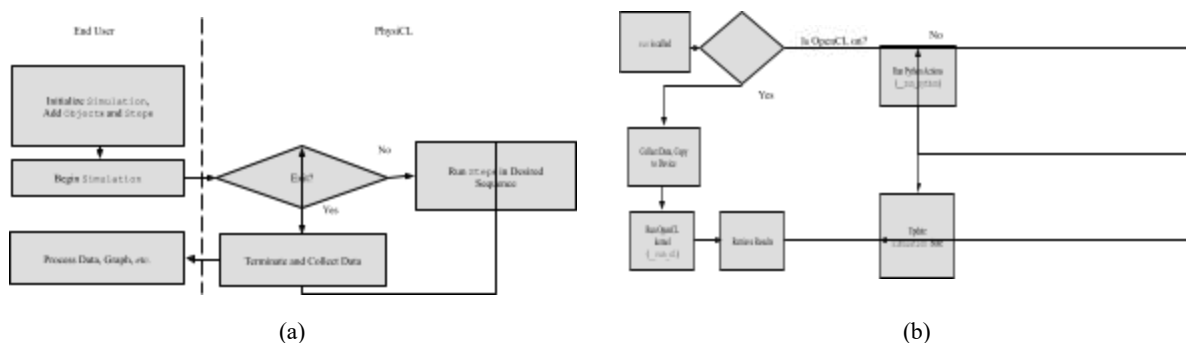


**FIGURE 1.** Outline of a basic simulation conducted using PhysiCL. (a) Outline of a general simulation, with the area left of the dashed line showing what the end user controls and the right showing what is abstracted away from the end user. (b) Outline of the operation of a Step in PhysiCL. A Python or OpenCL is run depending on whether OpenCL is turned on by the user.



At the root of the PhysiCL package is `Simulation`. It is primarily defined by an *exit condition*, two values representing  $\Delta t$  and  $t$ , an OpenCL context and command queue, a list of `Objects` and a list of `Steps`. When we call `start`—which will call `run` on a separate thread—some setup is performed. We set  $t$  and  $\Delta t$  to zero, get the starting timestamp, and initialize a list for keeping track of  $t$ s that were simulated. Then, while the exit condition returns false, we call `run` on each `Step`. After the exit condition returns true, we call `terminate` on each `Step` for it to perform any clean up. An overview of this process appears in Fig. 1a. Each `Step` utilizes three main methods, `__init__`, `run`, and `terminate`, as well as `__run_cl` and `__run_python`. The first is used to initialize the `Step`, the second one is used when the simulation runs each `Step`, and the third one is called when the simulation is finished running. The last two are called to run the simulation using a parallelized OpenCL implementation or native Python implementation, which allows for the comparison of their relative performance. Users who wish to write new `Steps` will primarily modify `__init__` and `run`, in addition to both `__run_cl` and `__run_python` if such a comparison is desired. An overview of a typical process the latter three functions are used in is shown in Fig 1b.

There are two primitive steps in the root module of PhysiCL. The first, `UpdateTimeStep`, is initialized with a function that takes the simulation as an argument, determines what  $\Delta t$  should be and updates  $t$  accordingly. The second, `MeasureStep`, is a generic class for measuring the states of simulations that subclasses will override as needed. In general, users will extend `MeasureStep` or one of its subclasses to measure behavior, and user extensions upon `Step` will represent state-altering behavior. Another `Step` worth noting is `physicl.newton.NewtonianKinematicsStep`, which updates the position of objects according to their velocity.

## OpenCL and Metaprogramming

PhysiCL relies on OpenCL and PyOpenCL<sup>3</sup> to achieve accelerated computation, and uses metaprogramming techniques—where new code is generated dynamically—in concert to provide increased speed in developing and executing simulations. OpenCL is a library that allows for parallel computing on a variety of devices, using programs known as *kernels*.<sup>1,2</sup> Kernels may be metaprogrammed using PhysiCL's `CLProgram`. `CLProgram` represents a partially written OpenCL kernel as well as the Python code needed to provide it input and retrieve output. There are two stages to metaprogramming using `CLProgram`. OpenCL kernels must be compiled before they are used, and when we first need to build our kernel, we call `build_kernel`. When this function is called, a completed OpenCL kernel is generated. From there, we can call `run`—which is done from within a `Step`—and the appropriate Python code to collect input data and run the kernel will be generated. After the kernel finishes, the resulting output of the kernel is then used to update the simulation as needed.

## Measurements



**FIGURE 2.** Three examples of the `Measurement` class demonstrating dimensional analysis and unit conversions. (a) Examples of binary and unary operations. (b) Example of two automatic unit conversions.

This subclass of Numpy's `ndarray`<sup>7</sup> represents an array of numbers that follows the *code units* scheme, which is where we scale units up or down to avoid floating point precision loss. Instances of this class are initialized with two parameters, `raw_value`, and `units`. `raw_value` can be another `ndarray`, another `Measurement`, or a list mixed with numbers and other `Measurements`. `units` is a string representing the units of the value, which

are written as their corresponding symbol, either the Python power symbol ( $**$ ) or a caret ( $^$ ), and the dimension of the unit.

The scaling process starts by determining what units are being used. After isolating these units, they are recursively converted to their defining units until they have been reduced to the 7 fundamental SI units. After this, we convert these fundamental units to the code scale units.<sup>4</sup> Each of these code scale units carries a scaling factor, which is used to affect the scaling of all Measurements that rely on the same fundamental units. We multiply each element of our array by this scale. We store these dimensions, as well as the dimensions of the original units used for use whenever a string representation is needed. Each of the 7 fundamental SI units can be scaled up or down using `set_code_scale`, as seen in Fig. 2a. Currently, it is designed so that it can only be done once, before any related modules are imported. This is to optimize for speed, as performing checks to see if two Measurements have the same scale can be costly; however, it may be possible to use something akin to a counter to keep track of the current scale. After it is set up, it may be operated on by directly calling one of Numpy's ufuncs—such as `numpy.square`<sup>5</sup>—or by utilizing the corresponding Python operator, generating results with the appropriate underlying units and scale, as seen in Fig. 2. It will not cancel or reduce any original units passed to it for speed; however, a future implementation may reduce units lazily when a string representation is needed.

## Photon Scattering, Measurement, and Generation

```
In [2]: T = 5778
Eg = np.linspace(phys.light.E_from_wavelength(200e-9), phys.light.E_from_wavelength(2500e-9), 1000)
gamma = phys.light.planck_distribution(Eg, T)

E = [phys.light.planck_phot_distribution(phys.light.E_from_wavelength(200e-9), phys.light.E_from_wavelength(2500e-9), T, bins=50000) for x in range(10000)]
phot = phys.light.generate_photons_from_E(E)
for p in phot:
    p.r = phys.Measurement([-6440e3 * 5, 0, 0], "m**1")
```

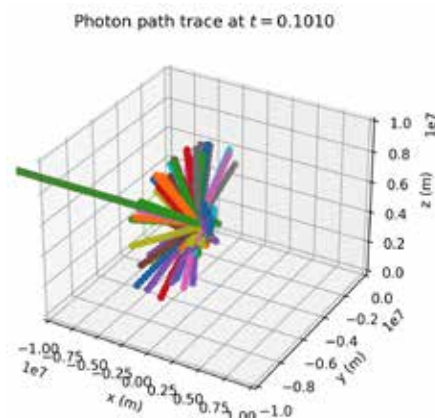
(a)

```
In [4]: runtime = ((6440 * 5 * 6440) * 1e3 / phys.light.c) * 5
print("Target runtime: " + str(runtime))
A targ = phys.Measurement(5.1e-11, "m**2") * (phys.Measurement(532e-9, "m**1") ** 4)
sim = phys.simulation(c1_w=True, exit_lambda=code cond.t == runtime)

sim.add_step(1, phys.UpdateTimeStep(lambda t: phys.Measurement(0.001, "s**1")))
sim.add_step(1, newton.NewtonianKinematicStep())
sim.add_step(1, light.ScatterIsotropicStep(k=h_targ, variable_n = True, variable_n_fn = c1_n, wavelength_dep_scattering=True))

tp = phys.light.TracePathMeasureStep(1000)
sim.add_step(0, tp)
sim.add_obj(phot)
```

(b)



(c)

**FIGURE 3.** An example simulation involving isotropic scattering around an approximation of the upper half of Earth's atmosphere with a photon distribution resembling that of the Sun, as well as output displayed in matplotlib. (a) A segment of the necessary code to set up a simulation involving a beam of photons being scattered, namely the creation of PhotonObjects drawn from `planck_phot_distribution`. (b) Another segment of the necessary code required to set up the simulation, including the addition of Steps and PhotonObjects. (c) The resulting paths of a beam of photons as they travel towards an object with arbitrarily high density.

Currently, the main feature of this package are the tools for photon scattering and measurement, which are in the `physicl.light` module. It includes `ScatterDeleteStep` and `ScatterIsotropicStep`, which represent photon absorption and isotropic scattering, respectively. It also includes `ScatterMeasureStep`, which measures photons passing through specified planes, `ScatterSignMeasureStep`, which measures the quantity

of photons with a positive/negative sign along any axis, and `TracePathMeasureStep`, which tracks the path a photon takes.

The first class, `ScatterDeleteStep`, represents the scattering of photons as if they were being absorbed into a medium. It assumes that the medium has a specified uniform number density,  $n_{targ}$ , and cross-sectional area,  $A_{targ}$ , throughout the entire simulation space. When this step is run, it finds all `PhotonObjects` within the simulation, and collects the  $\Delta r$ s for all photons. It also generates a random number in  $[0, 1)$  for each photon, and allocates two lists, one pointing to the photons examined, and another for the results of the OpenCL kernel it will run. The kernel will find  $P_{coll} = n_{targ} A_{targ} \Delta r$ , and if  $P_{coll}$  is greater than the random number generated for a particular photon, then it will be marked for removal. After the OpenCL kernel returns, the marked photons are deleted from the simulation.

`ScatterIsotropicStep` represents the scattering of photons as if they were being refracted into a random direction. Like `ScatterDeleteStep` it assumes a consistent  $n_{targ}$  and  $A_{targ}$  throughout the entire simulation, however the  $n_{targ}$  may be varied with an OpenCL expression, and if the user desires, scattering may also be dependent on the wavelength, as occurs with Rayleigh scattering. When this `Step` is run it first collects the  $\Delta r$  for each photon. It then generates a random  $\theta \in [0, 2\pi)$ ,  $\phi \in [0, \pi)$  that will be used to derive a new direction for the photon to go, and a random number  $rand \in [0, 1)$ . Next, it collects the original  $\vec{v}$  for the photons; if wavelength-dependent scattering is on, it collects each  $E_\gamma$ ; and if variable  $n_{targ}$  is on, it collects the current  $r$  of each photon. Then when the kernel is completed, `ScatterIsotropicStep` will apply the changes calculated in the kernel. If the velocity was changed, the photon will have its  $\Delta v \leftarrow v_{new} - v_{old}$ . An example of this in use can be seen in Fig. 3.

`ScatterMeasureStep` measures the total quantity of photons within a simulation, as well as the number and energies of photons that pass through a plane at a given point in time. When initialized, the user may decide whether they want the total quantity of objects to be measured, coordinates for the planes where we should measure photons passing through, and whether the `ScatterDeleteStep` should also record the energies of the photons passing through. `ScatterSignMeasureStep` measures the number of objects within a simulation as well as the number of objects whose  $v_x, v_y, v_z$  have values greater than zero. `TracePathMeasureStep` tracks the position of each object throughout a simulation. When this step is run, it iterates through each object in the simulation and performs several steps. If the current object in the iteration does not have a unique identifier, it assigns one. `TracePathMeasureStep` then records the starting time, creates a list to store positions, and if the user desires, the frequency with which the photon changed velocity. Then, `TracePathMeasureStep` records the current position of the object, and if the velocity changes, increments the accumulator representing the frequency of velocity changes. After the simulation is complete, `TracePathMeasureStep` compiles the data collected into a two-dimensional array representing the  $t$ s that were recorded, with each row represents an individual object, the number of times its velocity changed if desired, and finally all positions that were recorded for each time. An example of `TracePathMeasureStep` can be seen in Fig. 3, where its output data is graphed to show atmospheric refraction.

In addition to these tools to simulate and measure photons, there is `planck_phot_distribution`, which randomly generates a series of photon energies according to a desired segment of the Planck distribution. `planck_phot_distribution` works by finding the total area under a Planck distribution curve for a desired number of bins, normalizing the total area under these bins so that it equals 1, and finally randomly picking an energy bin using our normalized distribution. There are also two other ways to generate photons. `generate_photons_from_E` takes a list of  $E_\gamma$  and generates new photons for each energy given with a velocity of  $c$  in the  $+x$  direction. `generate_photons` takes a function that generates random numbers, minimum and maximum energies, and a desired number of photons, and returns a list of `PhotonObjects`.

## ACKNOWLEDGMENTS

I would like to acknowledge my physics professor, Dr. Sean O'Neill, for his guidance and feedback on this project. I would also like to acknowledge my capstone advisor, Dr. David Wolff, for providing feedback and facilitating this project. In addition, I would like to acknowledge Megan Longstaff, a fellow physics student who connected me with Dr. O'Neill. Finally, I would like to acknowledge Dr. Katrina Hay, Dr. William Greenwood, and

Professor Laurie Murphy for advising my academic career so far, without them this project would not have happened.

## REFERENCES

1. *Heterogeneous Computing with OpenCL*, edited by B. Gaster, (Morgan Kaufmann, Waltham, 2012), p. 277.
2. *OpenCL Programming Guide*, edited by A. Munshi (Addison-Wesley, Upper Saddle River, 2012), p. 603.
3. A. Klöckner, N. Pinto, Y. Lee, B. Catanzaro, P. Ivanov, and A. Fasih, *Parallel Computing* **38**(3):157–74 (2012).
4. Bureau International des Poids et Mesures, *The International System of Units 9th ed.* (2019), available from <https://www.bipm.org/utis/common/pdf/si-brochure/SI-Brochure-9.pdf>.
5. S. van der Walt, S.C. Colbert, and G. Varoquaux, *Comput Sci Eng.* **13**(2):22–30 (2011).



# JOIN US AT THE INTERSECTION OF SCIENCE AND ART

Call for Poster and Art submissions for  
the 2022 Physics Congress!

Have research or a project you want to present?  
Create a wonderful piece of art inspired by  
science that you'd like to show off?

**Sign up for the Poster and/or Art  
Competition at the 2022 Physics Congress!**

Prizes available for the winners!

PhysCon Travel Awards are NOW available for  
individuals and chapters attending the congress.  
Students awarded must submit abstracts for the  
poster or art session.



Apply Here:  
[www.sigmapi sigma.org/sigmapi sigma/congress/2022/awards](http://www.sigmapi sigma.org/sigmapi sigma/congress/2022/awards)



# Microgel Dynamics Characterization Using SEM

Samantha Tietjen,<sup>a)</sup> Richard Sent, Petru S. Fodor,<sup>b)</sup> and Kiril A. Streletzky<sup>c)</sup>

*Department of Physics, Cleveland State University, Cleveland, OH 44115, USA*

<sup>a)</sup>Corresponding authors: stietjen.2015@gmail.com

<sup>b)</sup>p.fodor@csuohio.edu

<sup>c)</sup>k.streletzky@csuohio.edu

**Abstract.** A methodology for imaging the dynamics of individual microgel particles using high resolution scanning electron microscopy (SEM) is presented. To enable this, the microgels are dispersed in an ionic liquid, which due to its low vapor pressure allows them to remain in suspension even under the high vacuum conditions present in a typical electron gun. Thus, compared with conventional electron microscopy studies of microgels, no sample drying or freezing is necessary which preserves their morphology while also allowing to probe microgel dynamics in solution. The results based on the individually tracked particles are compared with results from dynamic light scattering (DLS) which measures the mean size and diffusion properties of large collectives of particles. For the size measurements, the SEM and DLS data are in general agreement. For the particle dynamics, monitoring individual microgel motion reveals complex dynamics in which, aside from the expected thermal motion, one observes effects such as clustering, rotation and drift. This is in contrast with a control sample of hard sphere-like silica particles where the motion is primarily diffusional in good agreement with DLS studies.

## INTRODUCTION

Microgels are polymer-based particles that exhibit a reversible swelling in water, making them a system of interest for bio-sensing and drug delivery applications [1]. The experimental data on the size and dynamics of these systems is typically collected using optical techniques, such as dynamic light scattering (DLS). DLS relies on averaging data collected from sample volumes containing large numbers of particles. Thus, these methods often have to rely on the approximation of dilute, monodisperse particles of a certain shape (e.g. spheres) [2]. In this context having the ability to observe the dynamics of individual particles is particularly important for multicomponent systems, assemblies for non-spherical particles, or particles that have complex interactions with their environment.

Electron microscopy methods are an important set of tools used for the characterization of micro- and nano-scale systems, owing to their very high spatial resolution. They have been used in previous studies to characterize the morphology and size of microgel particle systems [3]. One has to note though, that the imaging in an electron microscope requires samples that: (i) are compatible with the high vacuum conditions in an electron gun required to prevent the scattering of the electron signal and electric discharges; (ii) are conductive so that they can dissipate charge accumulation due to beam exposure; and (iii) can withstand the potential thermal damage associated with exposure to the high energy electron beam. For the microgel example, meeting these stringent requirements involves drying or cryofreezing the samples. This might change microgel morphology [4], and more importantly prevents studies of dynamics of their motion or response to environmental conditions.

In this work, an alternative sample preparation methodology for microgel systems has been explored, enabling their high-resolution imaging in a scanning electron microscope (SEM). The method relies on dispersing the system of interest (microgels) in an ionic liquid. Owing to the very low vapor pressure of the ionic liquid used at room temperature, even under the high vacuum in the SEM, the suspension remains in liquid state. Moreover, the electrical and thermal conductivity of the ionic liquid also limits sample charging and thermal damage. This allows the imaging of the motion of individual microgel particles in conditions similar with those used for studying

dynamics of large ensembles of microgels using DLS. Aside from SEM imaging of microgel ionic liquid samples, this work presents SEM results for a control sample of monodisperse hard sphere silica particles in ionic liquid.

## EXPERIMENTAL PROCEDURE

Hydroxypropylcellulose (HPC) microgels were synthesized in water following refs. [2]. The final concentration of microgels in the aqueous solution was 2% by volume. Following the synthesis, the microgels were dispersed in the ionic liquid using equal amounts of stock solution and ionic liquid. The mixture was purged with dry  $N_2$  for 24 to 72 hours. In the process the water evaporated, while the mass of the solution was monitored, resulting in a microgel suspension in ionic liquid of 2% by volume. The ionic liquid used in this study was 1-n-Butyl-3-methylimidazolium (98% purity, Sigma Aldrich), chosen to maximize the mutual solubility of the ionic liquid with that of water [5]. A control sample of silica monodispersed microspheres (Cospheric LLC, 890 nm  $SiO_2$ ) in ionic liquid was prepared with the same volume concentration.

Solutions of the microgels in both water and ionic liquid were characterized using DLS setup described in ref. [6]. Figure 1 shows the temperature dependence of microgel hydrodynamic diameter ( $2R_H$ ) in ionic liquid and water. While ionic liquid DLS runs are noisier, the measured  $2R_H$  in ionic liquid agrees well with the  $2R_H$  in water below the microgel phase transition temperature ( $\sim 41^\circ C$ ). The larger error bars in the ionic liquid are indicative of stronger thermal fluctuations. To limit thermal effects of the laser beam on microgel ionic liquid solution all of the DLS data was collected at laser powers below 0.035 W. Heating the samples above the phase transition temperature, i.e.  $41^\circ C$ , did show differences between the water and ionic liquid suspensions, as the microgels showed no apparent deswelling in ionic liquid while deswelling by a factor of 2 in diameter in water, as expected.

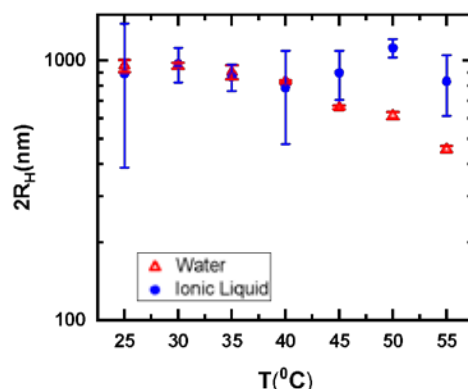


**FIGURE 1.** Hydrodynamic diameter ( $2R_H$ ) of microgels as a function of solution temperature in water and ionic liquid.

To prepare samples for SEM studies, the ionic liquid microgel suspension was dispersed ultrasonically for 10 minutes, and then a 1  $\mu L$  sample drop was deposited on a TEM copper grid. The excess liquid was removed using a piece of filter paper touched to the side of the grid, leaving the ionic liquid film as membranes suspended in the grid openings. The grid was then mounted on a standard SEM pin holder or an adaptor holder for TEM grids (Ted Pella #16111 or #15469). The imaging was done at room temperature in a field emission electron microscope Inspect F50 (FEI). It was observed that high magnification, high acceleration voltages, and long exposure resulted in the crosslinking of the ionic liquid leading to quenching of the particle dynamics. To mitigate this, the acceleration voltage was limited to 2kV and the diffusion data was collected for less than 1 minute to limit the overall dose.

## RESULTS AND DISCUSSION

SEM imaging of the particles suspended in ionic liquid allowed size measurements on individual particles. The secondary electron signal is used for imaging, with the contrast arising mainly from the topography of the microgel particles rising above the liquid ion – vacuum interface. These values were consistent with the distribution values extracted from DLS data. Moreover, the actual motion of individual particles could be monitored over times sufficiently long to observe their relevant dynamics. Figure 2a shows an SEM frame snapshot of 44 silica particles, the control sample. Using similar time stamped frames, the time evolution of the x- and y- position coordinates of



the particles are extracted using an open source particle tracking package (Tracker 5.0 [7]). Figure 2b shows the reconstructed trajectories for the 44 particles shown in Figure 2a over 33 seconds.

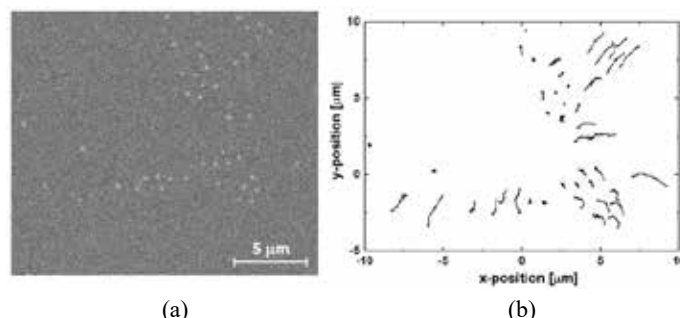


**FIGURE 2.** (a) Scanning electron microscopy snapshot of silica particles in ionic liquid ( $t = 0$  s). (b) Trajectories of the 44 silica particles tracked over a period of  $\sim 33$  seconds.

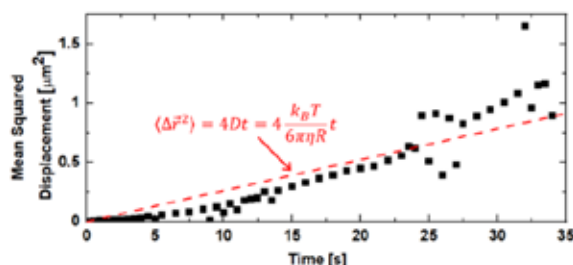


**FIGURE 3.** Time dependence of the average mean squared displacement for the silica particles imaged in Fig. 2. The dashed line corresponds to the expected two-dimensional Brownian motion.

The data collected for this assembly is summarized in Figure 3 by graphing the mean square displacement  $\langle \Delta \vec{r}^2 \rangle$  of the collection of particles as a function of time. For the control silica particles system, the resulting dynamics is consistent with the expectations based on the Stokes-Einstein equation (shown in Figure 3,  $D = \frac{k_B T}{6\pi\eta R}$ ) for thermal diffusion, where the diffusion constant  $D$  is calculated based on the particle hydrodynamic radius  $R = 890$  [nm]/2 and the measured ionic liquid viscosity  $\eta$  at room temperature  $T$ . In the above analysis, the motion is assumed to be two-dimensional as the secondary electron signal used for imaging originates primarily from the top surface of the sample, and thus only the motion of particles moving along the ionic liquid – vacuum interface could be captured. This approach is consistent with other high-resolution studies of hard-sphere like particles suspended in ionic liquids [8].

A similar procedure was followed to obtain corresponding data sets for microgel samples. In contrast with the silica samples the microgels exhibit more complex behavior, which deviates from simple thermal motion and includes clustering, rotational diffusion, and drift. Figure 4a, shows the initial positions as well as the subsequent motion of several microgel particles. The four particles in the lower-left corner have convergent trajectories which in many instances leads to clustering, where particles become temporarily attached and undergo collective motions. This type of clustering is particularly pronounced in regions close to where the ionic liquid suspension is attached to the copper TEM grid, possibly due to the liquid layer being thicker near the grid.

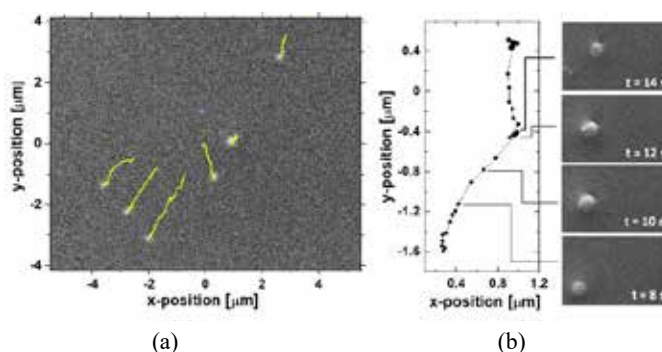


**FIGURE 4.** (a) Trajectories of microgels tracked over ~45 seconds; (b) High resolution snapshots of the translational and rotational motion of a single microgel particle and on left, trajectory of the particle imaged.

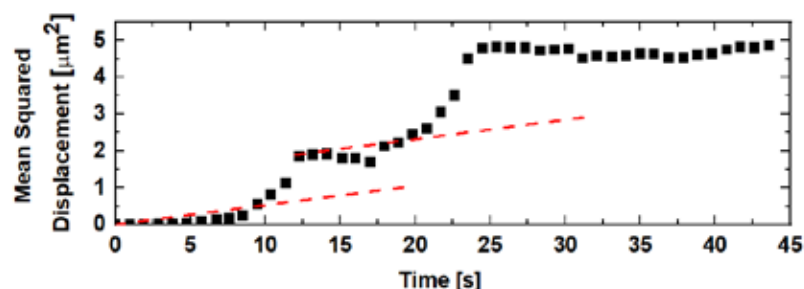


**FIGURE 5.** Mean squared displacement of the microgel tracked in Fig. 4b (the dashed lines correspond to the expected time dependence of the mean squared displacement for an assembly of thermally diffusing particles).

In another example of complex motion, Figure 4b shows a series of high-resolution snapshots of a single microgel particle. The morphological asymmetry of this particle allows for the observation of its rotational motion where the particle undergoes a  $\sim 90^\circ$  rotation in the image plane over 4 seconds. This rotational motion is also accompanied by a complicated translational motion, in which the particle motion is localized over time scales on the order of 10 seconds, then rapidly drifts to another region, where the localized motion resumes. An analysis of the mean squared displacement, Figure 5, finds that the localized motion is consistent with thermal diffusion. The episodes of rapid drift sequences interrupting the thermal diffusion, indicate that the dynamics of this system is quite rich. This is possibly related with the complex microgel morphology and their more complicated interactions with the environment. The observed complex microgel dynamics made it impossible to deduce microgel translational diffusion coefficient via averaged mean-squared displacement approach used for silica particles. Additional data on particle-particle and particle-environment interactions is needed to fully understand microgel motion in ionic liquid.

## CONCLUSIONS

We have demonstrated that high resolution imaging of particles dispersed in an ionic liquid can be a very powerful tool for studying their structure and dynamics. For silica systems tracked particle motions match well the theoretical assumptions of monodisperse noninteracting spherical particles. The results are consistent with motion dominated by thermal diffusion. On the other hand, microgel suspensions show significant deviations from simple Brownian motion, presumably related to their different morphology and non-trivial particle-particle and particle-environment interactions. Future work will focus on acquiring data to uncover these relationships, as well as to image microgel dynamics under changing environmental conditions, such as temperature.

## ACKNOWLEDGEMENTS

The authors acknowledge NSF (REU award #1659541) for support of S.T., CSU's USRA for support of R.S., and CSU's FRD award for support of K.S. This work was also supported by the NSF Grant No. 1126126. Authors

would like to thank T. Dobrila and D. Terrano for initial microgel SEM and IL viscosity measurements. Any opinions, findings, conclusions and/or recommendations expressed here are those of the authors and do not necessarily reflect the views of the NSF.

## REFERENCES

1. J.K. Oh, R. Drumright, D.J. Siegwart, K. Matyjaszewski, *Prog. Polym. Sci.* **33**, 4, 448 (2008).
2. K. Freeman, J. Adamczyk, K.A. Streletsky, *Macromolecules* **53**, 21, 9244 (2020).
3. J. Liang, F. Teng, T.-M. Chou, M. Libera, *Polymer* **116**, 1 (2017).
4. T. Dobrila, K.A. Streletsky, P. Fodor, *The Ohio Journal of Science* **118**, A48 (2018).
5. T. Zhou, L. Chen, Y. Ye, L. Chen, Z. Qi, H. Freund, K. Sundmacher, *Ind. & Eng. Chem. Res.* **51**, 17, 6256 (2012).
6. R. McDonough, R. Cueto, P. Russo, G.D.J. Phillies, K.A. Streletsky, *Macromolecules* **48**, 19, 7245 (2015).
7. <https://physlets.org/tracker/>
8. P.Y. Kim, A.E. Ribbe, T.P. Russell, D.A. Hoagland, *ACS Nano*, **10**, 6, 6257 (2016).

# Apply for SPS Fall Awards!

Apply by **November 15** to be considered for the following awards:



### Future Faces of Physics Award

Made to SPS chapters to support projects designed to promote physics across cultures, as well as promote the recruitment and retention of people from groups historically underrepresented in physics.



### Marsh W. White Award

Made to SPS chapters to support projects designed to promote interest in physics among students and the general public.

### SPS Chapter Research Award

Provides calendar year grants to support local chapter activities that are deemed imaginative and likely to contribute to the strengthening of the SPS program.



### Sigma Pi Sigma Chapter Project Award

Awarded to Sigma Pi Sigma chapters for funding of chapter inductions and events that aim to engage alumni or expand the recognition of Sigma Pi Sigma within the campus and surrounding community.

Visit our website to see past awarded chapters' projects and apply today!  
[www.spsnational.org/awards](http://www.spsnational.org/awards)

# Quantum Inequalities and Particle Creation in the Presence of an External, Time-Dependent Mamaev-Trunov Potential

Kalista Schauer,<sup>1, a)</sup> Dr. Michael Pfenning,<sup>1, b)</sup> and Jared Cochrane<sup>1, c)</sup>

<sup>1</sup>United States Military Academy at West Point, West Point, New York 10996-1790, USA

<sup>a)</sup>Corresponding author: kalistaschauer@gmail.com

<sup>b)</sup>michael.pfenning@westpoint.edu

<sup>c)</sup>jared.cochrane.mil@mail.mil

**Abstract.** In 2011, Mr. Dan Solomon proposed a model of a quantized scalar field interacting with a time-dependent Mamaev-Trunov potential in two-dimensional Minkowski spacetime. This model is governed by the Klein-Gordon wave equation with a time-dependent potential. Mr. Solomon claims that this model violates both the classical energy conditions of special relativity and the quantum energy conditions of quantum field theory in curved spacetime. Every classical energy condition can be violated, and their natural replacements are known as quantum inequalities. Mr. Solomon attempted to prove violations of the spatial and temporal quantum inequalities, and he correctly assumed that the negative energy splits into two fluxes at the Cauchy surface, where the potential is turned off. Unfortunately, Solomon neglects the contribution to the energy density due to particle creation when the potential is turned off at time  $t = 0$ . In this project, we calculate the contribution to the stress energy tensor due to particle creation. We show that while the classical energy conditions are violated, the quantum energy inequalities hold, contrary to Mr. Solomon's statements.

## SCIENTIFIC BACKGROUND

### Mathematical Background

The mathematical foundation of quantum mechanics consists of wave functions and operators. Wave functions express the state of a system while operators represent observables. Linear algebra is the underlying mathematics of quantum mechanics, where abstract vectors represent wave functions and observables are performed as linear transformations [1]. Quantum mechanics uses Dirac notation to represent a vector as a 'ket', shown as  $|a\rangle$ . The dual vector for a ket is a 'bra', with the inner product 'bra-ket' written as  $\langle a|b\rangle$ .

An inner product space is a vector space over the real or complex numbers containing inner products or dot products. The vector spaces in which wavefunctions exist are called Hilbert spaces. Hilbert spaces are finite-dimensional and span the complex numbers [2]. A Hilbert space is a Banach space where the norm, or mapping, is an inner product. Hilbert spaces are mathematically easier to handle than general Banach spaces due to orthogonality. A Hilbert space is a complete inner product space, an example of which is the collection of square integrable functions,

$$f(x) \text{ where } \int_a^b |f(x)|^2 dx < \infty, \quad (1)$$

denoted as  $L_2(a, b)$ . While this is a relatively small vector space, it is the Hilbert space referred to in quantum mechanics [2]. The calculations in this paper use two-dimensional Minkowski spacetime. This refers to a Euclidean manifold, with one spatial dimension and one temporal dimension, where the spacetime interval between two events does not depend on an inertial frame of reference in which the events were measured.

Another mathematical object used throughout this paper is a tensor, which is analogous to a vector-composed matrix. Tensors are arrays of functions of spatial coordinates. The most common tensor in this paper is the stress-energy tensor, with the general form of,

$$\hat{T}_{(x,t)} = \begin{pmatrix} T_{tt}^L & T_{tx} & T_{xt} & T_{xx} \end{pmatrix}, \quad (2)$$

which describes the density and flux of matter and energy in spacetime. This is a generalization of the stress tensor of Newtonian physics. In general relativity, the Einstein tensor describes space-time curvature and the energy momentum tensor describes localized matter distribution.

## Quantum Field Theory

In quantum mechanics, a single particle, with spin =  $\frac{1}{2}$ , has two quantum states in a two-state system: one state represented as  $|\downarrow\rangle$  and the other as  $|\uparrow\rangle$ . In the Copenhagen model of quantum mechanics, a particle exists in a state of superposition where the particle is simultaneously in both states. The superposition wave function for a system with two spatial states,  $A$  and  $B$ , can be written as,

$$\psi = \frac{1}{\sqrt{2}} [|\uparrow\rangle|A\rangle + |\downarrow\rangle|B\rangle]. \quad (3)$$

A wave function describes the state of a particle. While a particle is constrained to move in one dimension, influenced by a specified force, a wave function is dependent on position for any given time. Until an act of measurement collapses the wave function, particles do not have specific dynamical properties like position or momentum [1]. Upon measurement of the system, the wavefunction spontaneously decays and the observer sees the system existing in only one of the two states. States are entangled if they are directly correlated with one another [3]. All observables in a system have corresponding wavefunctions [1]. These wavefunctions are mathematically represented by a superposition of pure time harmonic, or sinusoidal, vibrations. Multiplying the wavefunction by its complex conjugate and integrating gives the probability of finding the particle between two points for a given time. A particle's probability density is described as a wave group. The time-dependent Schrödinger equation [1], written below, can be solved to find a particle's wave function  $\psi(x, t)$ ,

$$i\hbar \frac{\partial \psi}{\partial t} = -\frac{\hbar^2}{2m} \frac{\partial^2 \psi}{\partial x^2} + V\psi. \quad (4)$$

In this paper, the potential  $V$  has no explicit time-dependence. The general solution to the time-dependent Schrödinger equation is a linear combination of separable solutions, a continuous sum over wavenumbers. The solution, called a wave packet, carries a range of energies and speeds. Wave packets are localized state functions consisting of a packet of waves with wavenumbers and frequencies centered around a single value  $k$  [1]. As time increases, quantum wave packets disperse, meaning that the width of the wave packet increases with time. This happens because each plane-wave component in the wave packet has a unique wave number and propagates at a different velocity [5]. Wave packets for bound states have discrete harmonic components [11] and wave packets of free electrons with initially localized position disperse over time. Wave packets of classical macroscopic objects also have dispersion times, albeit on a much longer time scale. Dispersion is an important aspect of waves and wave propagation. The dispersion relation, different for various physical systems, is the relationship between a wave's frequency and wavenumber. In quantum mechanics, the smaller the value of the spatial uncertainty  $\sigma_x$ , the faster electron wave packets disperse [5].

According to Heisenberg's uncertainty principle, one cannot simultaneously measure momentum and position with precise and accurate measurements for both. Instead, the more precisely one measures momentum, the less precisely one can measure position, and vice versa. With the standard deviation denoted by  $\sigma$ , the Heisenberg uncertainty principle for position and momentum is,

$$\sigma_x \sigma_p \geq \frac{\hbar}{2}. \quad (5)$$

## Energy Conditions in Classical General Relativity

We treat spacetime as a classical curved Lorentzian manifold. This manifold is subject to the Einstein equation,

$$R_{\mu\nu} - \frac{1}{2}Rg_{\mu\nu} - \Lambda g_{\mu\nu} = 8\pi G_N T_{\mu\nu}. \quad (6)$$

If  $u^\mu$  is a future-directed timelike vector and  $k^\mu$  is a future-directed null vector, then the stress-tensor for matter under classical physics obeys the classical energy conditions contained in Table 1.

**TABLE 1.** Energy Conditions in Classical General Relativity.

Energy Condition	Inequality
Weak Energy Condition	$T_{\mu\nu}u^\mu u^\nu \geq 0$
Null Energy Condition	$T_{\mu\nu}k^\mu k^\nu \geq 0$
Strong Energy Condition	$(T_{\mu\nu} - \frac{1}{2}Tg_{\mu\nu})u^\mu u^\nu \geq 0$
Dominant Energy Condition	$T^\mu_\nu u^\nu \geq 0$

In classical physics, observer-measured energy density is non-negative. Thus, for all timelike vectors  $u^a$ , the matter stress-energy tensor  $T_{ab}$  obeys the weak energy condition. The weak energy condition constrains the behavior of Einstein's field equation solutions. At a critical stage during gravitational collapse, the weak energy condition makes singularity formation inevitable. Thus, gravitational mass must be positive [9].

## Quantum Inequalities

A general feature of quantum field theory is the proposition every classical energy condition can be violated. This means that energy density under quantum field theory can be negative without bound. Situations yielding observer-measured negative energy density include the Casimir effect (explanation below, see Figure 1), black hole evaporation, and squeezed light states. Without placing restraints on negative energy density, it is possible to violate the cosmic censorship conjecture that every singularity must have an event horizon to hide the singularity from direct observation. In addition, it would then be possible to experience closed time-like curves or traversable wormholes, both of which are not allowed under classical physics [9]. The constraints on negative energy density come in the form of quantum inequalities, which are “natural” mathematical replacements for the classical energy conditions. Quantum inequalities constrain the duration and magnitude of negative energy fluxes. Most often, a quantum energy inequality is averaged along the worldline, or geodesic, of an inertial observer. This paper will focus on the worldline quantum inequality with mention to the spatial quantum inequality.

## Cauchy Surface

A Cauchy surface is a plane in spacetime where points on the plane are spatially related but have no time difference. A spacetime possessing a Cauchy surface is inherently causal. Causality implies that the Cauchy surface can be thought of as an instant in time where the initial conditions of the plane uniquely determine future events. We study a two-dimensional spacetime where the Cauchy surface refers to the one-dimensional plane of  $t = 0$ . The term IN region refers to events in the causal past where  $t < 0$  and the OUT region refers to the causal future where  $t > 0$ .

## The Casimir Effect

The Casimir effect is a physical force due to the presence of a quantized field. Mechanically speaking, it is the attractive force between two parallel perfectly conducting plates held at a close separation distance. The force arises from the quantum and thermal vacuum fluctuations of the electromagnetic field [15].

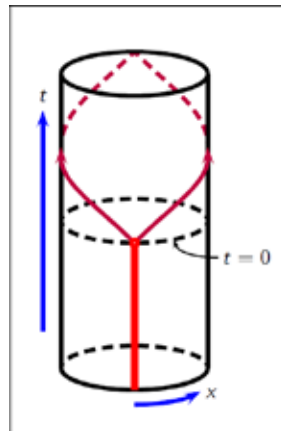


FIGURE 1. The Casimir effect (red) in two-dimensional spacetime.

The Casimir effect for a two-dimensional, potential-free cylinder spacetime is displayed in Figure 1. The expression for a cylinder spacetime with no potential for the OUT region ( $t > 0$ ) is,

$$\langle \tilde{0}_L | T_{00} | \tilde{0}_L \rangle_{Ren.} = \left( \frac{-\pi}{6L^2} + \frac{1}{4L} \right) \delta_{\mu\nu}. \quad (7)$$



The expression for a cylinder spacetime for the IN region ( $t < 0$ ) is,

$$\langle 0_L | T_{00} | 0_L \rangle_{Ren.} = \left( \frac{-\pi}{6L^2} + \frac{A}{L^2} \right) \delta_{\mu\nu}. \quad (8)$$

which is true for all locations except that of the delta-function potential.

A motivating problem for this research is calculating the Casimir effect for a scalar field in the presence of delta-type potentials. The “Casimir problem” refers to the response of a quantum field’s fluctuations in response to externally imposed boundary conditions. Physically, there are no interactions strong enough to enforce a boundary condition on every frequency of a fluctuating field. Graham et al. explore a physical model of this situation [12].

## Wightman Axioms

Despite the long history of quantum field theories, there are no rigorous descriptions of the structure of quantum field theories. Quantum field theory is often described as the quantization of classical field theories. Quantum field theories that use axioms, known as axiomatic quantum field theories, take a more systematic approach. Axiomatic quantum field theory can explain the transition from Minkowski spacetime to Euclidean spacetime, therefore explaining the transition from relativistic quantum field theory to Euclidean.

Wightman fields are operator valued distributions satisfying the Wightman Axioms. The Wightman functions, which are used in this paper, are the functions that correlate to Wightman fields. Wightman quantum field theory consists of the space of states (the projective space of a complex Hilbert space), the vacuum vector, a unitary representation of the Poincaré group (which is the group of Minkowski spacetime isometries, or length-preserving linear transformations), and field operators. This data collectively satisfies the three Wightman Axioms of covariance, locality, and spectrum condition [15].

## Green’s Functions

Green’s theorem is often used in electrostatics problems involving finite regions of space with bounding surfaces and prescribed boundary conditions. This is because it provides mathematical tools to handle boundary conditions [6]. In previous papers, Green’s functions are used to derive the energy conditions with a closed boundary and Cauchy boundary conditions [7]. One begins with the wave equation, which typically has the basic structure,

$$\nabla^2 \Psi - \frac{1}{c^2} \frac{\partial^2 \Psi}{\partial t^2} = -4\pi f(x, t), \quad (9)$$

where  $f(x, t)$  is a known source distribution and  $c$  is the velocity of wave propagation in the medium. The solution to the wave equation can be represented as a sum of mode functions. The Euclidean two-point function is equal to the sum of the mode functions and is the analogue of a Feynman Green’s function,  $G(\mathbf{x}, \mathbf{x}')$ , for the Lorentzian metric. Thus, to solve the wave equation, it is helpful to first find a Green’s function.

The general solution for a Green’s function is comprised of the advanced and retarded Green’s functions,  $G^{(-)}(x; x')$ ,  $G^{(+)}(x; x')$ , respectively. The general solution for the Green’s function is,

$$G(R) = AG^{(+)}(R) + BG^{(-)}(R), \quad (10)$$

where  $R = |R|$ , where  $R = x - x'$  given the vectors of points  $x$  and  $x'$ . Coefficients  $A$  and  $B$  depend on the boundary conditions of the given problems.  $G^{(+)}$ , the in-traveling wave, exhibits the causal behavior associated with a wave disturbance. The term  $AG^{(+)}(R)$  represents a diverging spherical wave that propagates from the origin. Likewise,  $G^{(-)}$  is the advanced Green’s function where the term  $BG^{(-)}(R)$  represents a converging spherical wave traveling toward the origin [6].

The time-dependent Green’s functions for a nondispersive medium are,

$$G^{(\pm)}(R, \tau) = \frac{1}{R} \delta\left(\tau \mp \frac{R}{c}\right), \quad (11)$$

where the Green’s functions are dependent on the relative distance,  $R = x - x'$ , and the relative time,  $\tau = t - t'$ , between source and observation point. The delta function’s argument shows that an effect, observed at point  $\mathbf{x}$  at time  $t$ , is caused by the action of a source located a distance  $\mathbf{R}$  away occurring at an earlier (retarded) time. The time difference, represented as  $\frac{R}{c}$ , is the time of propagation of the disturbance between the two points. To solve the wave function, one can integrate the Green’s function  $G^{(\pm)}(x, t; x', t')$  and source distribution  $f(x', t')$ ,

$$\Psi^{(\pm)}(x, t) = \iint G^{(\pm)}(x, t; x', t') f(x', t') d^3x' dt'. \quad (12)$$

This equation applies to a source distribution localized in time and space. To apply the above equation to a definite physical problem, one may add solutions to the homogeneous equation [6].

By calculating the solutions to the wave equation, one can construct the quantum inequalities by summing the solution mode functions. Thus, by knowing the two-point function for the given spacetime, one can calculate the quantum inequalities by Euclideanizing and taking the necessary derivatives of the two-point function [7].

## PROJECT INTRODUCTION

In classical physics, there exist classical energy conditions that mathematically constrain energy density in space and time to be nonnegative (Table 1). These come from the observation that mass is only positive in value. However, in quantum physics, energy density can be negative. Quantum inequalities are natural replacements for classical energy conditions and are local constraints on the extent and magnitude of negative energy density in spacetime. In quantum field theory, the energy density can be calculated from the Wightman two-point function,

$$\rho(x, t, x', t') = \frac{1}{2} \left( \partial_t \partial'_t + \partial_x \partial'_x \right) G(x, t, x', t'). \quad (13)$$

Mamaev and Trunov proposed a novel method to calculate the Casimir effect, explained below. They calculated the vacuum expectation value of the stress-energy tensor for a relativistic quantum field theory, where the quantum field interacts with an externally applied potential featuring two Dirac delta functions. A paper by Solomon asserts that this violates the spatial energy condition. However, Solomon did not include the energy contribution of particle creation to the stress-energy tensor. In contrast, in this paper we include the effects of particle creation.

We propose calculating the energy contribution to the stress-energy tensor caused by particle creation at the Cauchy surface, where  $t=0$ . To mathematically prove the correctness of this approach, we examine two-dimensional Minkowski spacetime in the presence of an external, time-dependent Mamaev-Trunov potential. For simplicity, we are using the relativistic Klein-Gordon-Fock wave equation for massless, spinless particles,

$$\frac{\partial^2 \Phi}{\partial t^2} - \frac{\partial^2 \Phi}{\partial x^2} + V(x, t) \Phi = 0. \quad (14)$$

The Klein-Gordon-Fock relativistic wave equation originates from the Schrödinger equation and describes energy and momentum. The equation is second order in space and time and describes the dynamics of a boson particle. We use this equation because it is mathematically simpler to use than the Dirac equation for relativistic particles with half integer spin.

The scalar quantum field with the time-dependent potential is,

$$\frac{\partial^2 \Phi}{\partial t^2} - \frac{\partial^2 \Phi}{\partial x^2} + 2\lambda V(x) \theta(-t) \Phi = 0, \quad (15)$$

with the Mamaev-Trunov-type potential given by,

$$V(x) = \left[ \delta\left(x - \frac{a}{2}\right) + \delta\left(x + \frac{a}{2}\right) \right]. \quad (16)$$

The potential is two delta-functions barriers separated by a distance  $a$  and centered at the origin. The presence of the delta-functions causes a constant, negative-energy Casimir effect in the empty region between them and zero energy density outside of the delta-functions [3]. When the potential is shut off, the negative-energy Casimir effect becomes dynamical, and begins to move left- and right-ward in the spacetime.

Substituting (10) into (9) yields,

$$\frac{\partial^2 \Phi}{\partial t^2} - \frac{\partial^2 \Phi}{\partial x^2} + \lambda \left[ \delta\left(x + \frac{a}{2}\right) + \delta\left(x - \frac{a}{2}\right) \right] \Theta(-t) \Phi = 0, \quad (17)$$

where  $\lambda$  is the coupling constant,  $\delta$  is the Dirac Delta function, and  $\theta$  is the unit step function.

## Results of Mamaev And Trunov

Mamaev and Trunov, in their 1981 paper [11], proposed a novel method to calculate the Casimir effect by calculating the vacuum expectation value of the stress-energy tensor for a relativistic quantum field theory. Mamaev and Trunov calculate the vacuum energy-momentum tensor for bounded manifolds without necessitating a cut-off value. They replace impenetrable boundaries with localized potentials dependent on  $\lambda$ . This method uses a quantum field that interacts with an externally applied potential- the “Mamaev-Trunov potential” used in this paper. Mamaev and Trunov calculate the well-behaved difference between the expectation value of the stress-energy tensor with and without a potential. By taking the limit of the coupling strength as the potential approaches infinity, they calculate the traditional Casimir effect.

The quantum field,  $\Phi(x, t)$ , in this model utilizes the Klein-Gordon-Fock equation with a time-independent potential,

$$\left[ \partial_t^2 - \partial_x^2 + \lambda V(x) \right] \Phi(x, t) = 0. \quad (18)$$

Mamaev and Trunov determine the kinetic energy density, the part of the energy density that does not explicitly dependent on the scalar potential, of a massless scalar field in one-dimensional spacetime. They use a simple potential comprised of two Dirac delta functions that have a separation distance of  $a$  and are centered around the origin. The potential is given by,

$$V(x) = \delta\left(x + \frac{a}{2}\right) + \delta\left(x - \frac{a}{2}\right). \quad (19)$$

This yields a negative result for kinetic energy density in the region between  $-\frac{a}{2}, \frac{a}{2}$ , shown in grey in Figure 2. Next, they calculate the renormalized vacuum expectation value of the energy-density operator. This is expressed

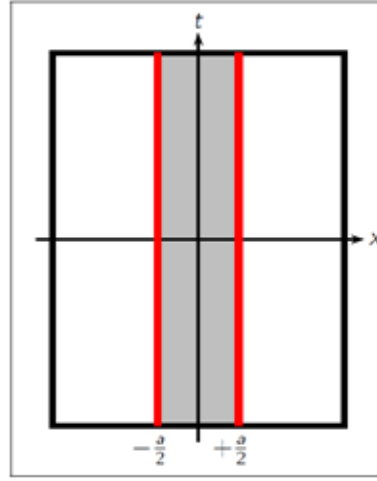


FIGURE 2. Mamaev and Trunov's solution for the Casimir effect (red).

mathematically as,

$$\langle \Omega | T_{00} | \Omega \rangle_{ren}(x) = \varepsilon \left[ \Theta\left(x + \frac{a}{2}\right) - \Theta\left(x - \frac{a}{2}\right) \right], \quad (20)$$

where  $\varepsilon = \varepsilon_1 + \varepsilon_2$ , and  $\varepsilon_1$  is the contribution to the vacuum expectation value due to the “odd” mode solutions and  $\varepsilon_2$  is the contribution to the vacuum expectation value due to the “even” mode solutions.

An approximation of the value of the Casimir energy density is given by,

$$\varepsilon(\lambda, a) = -\frac{\lambda}{2\pi a} \int_0^\infty \frac{dy y e^y}{y e^y + \sinh \frac{a}{2} \sinh y} + \frac{\lambda}{2\pi a} \int_0^\infty \frac{dy y e^y}{y e^y + \cosh \frac{a}{2} \cosh y} \simeq -\frac{3\pi\lambda}{4a(18\lambda a + 7\pi^2)}. \quad (21)$$

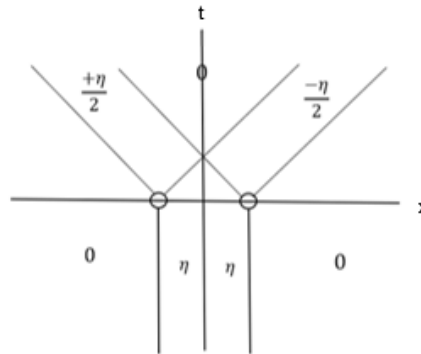


FIGURE 3. Our competing model. The difference between Mr. Solomon's model and ours is that our model includes boundary conditions for the energy fluxes.

## Results of Graham et al.

Graham et al. [12] explore a physical model of the Casimir effect by coupling a fluctuating field to a smooth background potential where the boundary condition is implemented in a certain limit. Graham et al. develop new methods to compute renormalized energy densities and single loop quantum energies. The former process is the method we use in this paper to compute the renormalized energy density. The approach of Graham et al. uses scattering data to compute Green's functions for time-independent background fields. Their calculation is useful for the numerical study of single limits since it both avoids oscillating terms as well as exponentially growing and decaying terms.

We examined the results of Graham et al. [12] to learn from their general approach to calculating a complete renormalization of the expectation value of energy density for a scalar field in the presence of a potential. Graham et al. calculate a massive scalar field in Minkowski spacetime that obeys the wave equation,

$$\left[ \partial_t^2 - \partial_x^2 + m^2 + \lambda \left( \delta \left( x - \frac{a}{2} \right) + \delta \left( x + \frac{a}{2} \right) \right) \right] \Phi(x, t) = 0. \quad (22)$$

Graham et al. renormalize by identifying divergent contributions to the Casimir energy. They separate the expectation value of the energy density operator into three parts,

$$\langle \Omega | T_{00} | \Omega \rangle_{Ren.} = \frac{1}{2} (\bar{\epsilon} + \epsilon_{FD} + \epsilon_{CT}), \quad (23)$$

where,

$$\bar{\epsilon}(x, a, \lambda) = \int_m^\infty \frac{dt}{\pi} \frac{\eta(it, x)}{\sqrt{t^2 - m^2}}, \quad (24)$$

and,

$$\epsilon_{FD}(x, a, \lambda) + \epsilon_{CT}(x, a, \lambda) = \frac{\lambda}{2\pi} \delta \left( |x| - \frac{a}{2} \right) - \frac{m^2 \lambda}{2\pi} \int_m^\infty \frac{dt}{t \sqrt{t^2 - m^2}} \left( e^{-2|x-\frac{a}{2}|t} + e^{-2|x+\frac{a}{2}|t} \right). \quad (25)$$

The vacuum expectation value of the energy density is then calculated as,

$$\langle \Omega | T_{00} | \Omega \rangle_{Ren.} = \left( -\infty + \frac{\lambda}{4\pi} \right) + \left[ \delta \left( x - \frac{a}{2} \right) + \delta \left( x + \frac{a}{2} \right) \right] + \{0 \text{ for } |x| > a/2, \epsilon(\lambda, a) \text{ for } 0 \leq |x| < a/2\}. \quad (26)$$

## Results of Flanagan

We examine the results of Flanagan [9] to calculate energy density of the stress-energy tensor by using bounds. Flanagan analyses the behavior of the renormalized expected stress-energy tensor in two-dimensional Minkowski spacetime for a free massless scalar field. Flanagan calculates the optimal lower bound and characterizes its respective state. Next, Flanagan calculates the lower bound for an arbitrary smooth positive weighting function. Flanagan's definition for the temporally sampled energy density for fixed spatial position  $x_0$  is,

$$\epsilon_T[f] = \int_{-\infty}^\infty \langle \omega | : T_{00} : | \omega \rangle (x_0, t) f(t) dt, \quad (27)$$

where  $T_{\mu\nu}$  is the stress-energy operator and  $f(v)$  is a non-negative normalized sampling function. Flanagan then defines the spatially sampled energy density as,

$$\int_{-\infty}^\infty \langle \rho \rangle_{Ren.}(\tau) f(\tau) d\tau \geq -\frac{1}{24\pi} \int_{-\infty}^\infty \frac{f(v)^2}{f(v)} dv. \quad (28)$$

## Results of Solomon

In 2011, Dan Solomon published a paper [10] claiming that his model would violate Flanagan's two-dimensional worldline quantum inequality [9],

$$\int_{-\infty}^\infty \rho(\tau) f(\tau) d\tau \geq -\frac{1}{24\pi} \int_0^\infty \frac{f'(v)^2}{f(v)} dv, \quad (29)$$

where  $\rho(\tau)$  is the energy density,  $f(\tau)$  is a sampling function, and  $f(v)$  is a non-negative normalized sampling function.

Solomon derived that the negative energy between the two delta-functions splits into two fluxes of negative energy, one moving left and one moving right as shown in Fig. 2. For an observer sitting to the right of the region of the potential, the negative energy-density integrated against Solomon's test function results in the inequality,

$$\frac{-\eta}{2} \left( \frac{3a^5}{8t_0^5} + \frac{5a^3}{2t_0^3} \right) \geq -\frac{5}{3\pi t_0^3}, \quad (30)$$

which indeed violates the worldline quantum inequality in two dimensions. Solomon uses a similar technique to violate the spatial quantum inequality. If the fluxes shown in Figure 2 are correct, then the quantum inequalities would fail, demonstrating a mathematical flaw in a fundamental property of quantum physics.

However, turning off the Mamaev-Trunov potential at the Cauchy surface, where  $t = 0$ , causes a change in the background spacetime. This leads to particle creation that causes excitations of the "standard" modes in the "OUT" region of spacetime, where  $t > 0$ . Solomon neglects the fact that shutting off the potential at time  $t = 0$  results in particle creation. Not incorporating particle creation results in an incorrect value for the energy contribution to the stress-energy tensor, eventually leading to a different result.

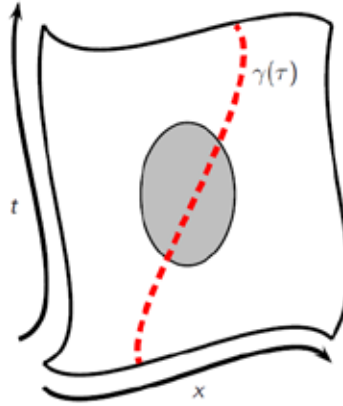


**FIGURE 4.** A two-dimensional universe with a timelike geodesic (red line) passing through a region of space encompassing negative energy density (grey region).

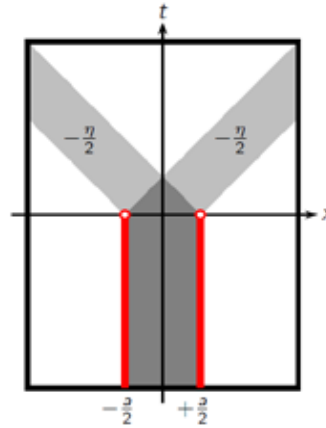


**FIGURE 5.** Solomon's Model.

## Previous Work on Topic

A previous paper published by Pfenning [13] studies a massless, quantized scalar field in the presence of an external, time-dependent Mamaev-Trunov potential for a single delta-function in two-dimensional cylinder spacetime, illustrated in Figure 6. As in this project, the quantum field is governed by the Klein-Gordon-Fock wave equation.

The renormalized expectation value of the stress-energy tensor for the IN region is,

$$\langle 0_L | T_{\mu\nu}^{IN} | 0_L \rangle_{Ren} = \left( -\frac{\pi}{6L^2} + \frac{B-C}{L^2} \right) \delta_{\mu\nu}, \quad (31)$$

and for the OUT region is,

$$\langle 0_L | T_{\mu\nu}^{OUT} | 0_L \rangle_{Ren} = \frac{\lambda}{4\pi} [\delta(t+x) + \delta(t-x)] \delta_{\mu\nu} + \frac{\lambda}{4\pi} [\delta(t+x) - \delta(t-x)] [0 \ 1 \ 1 \ 0]. \quad (32)$$

Shutting the potential off at time  $t = 0$  creates two positive energy pulses, shown in Figure 7. The pulses have magnitude  $\frac{\lambda}{4\pi}$ ; one pulse moves in the  $-x$  direction and the other in the  $+x$  direction.

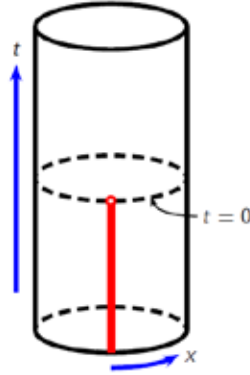


FIGURE 6. Pfenning's model of cylinder spacetime in the presence of a potential.

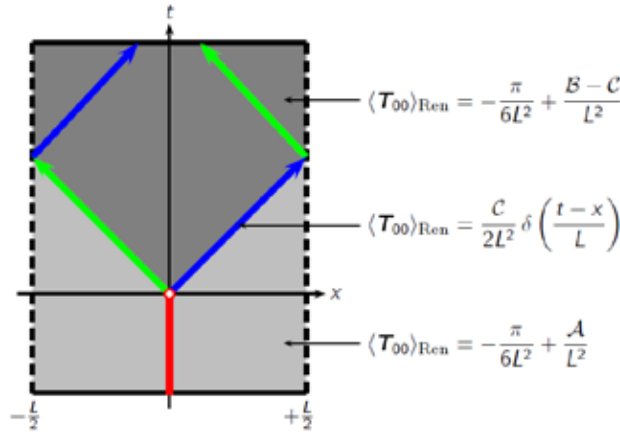


FIGURE 7. Findings from Dr. Pfenning's model of cylindrical spacetime.

## CALCULATIONS

This paper mathematically demonstrates that there exist excitations of the “standard” modes of the OUT region of spacetime when the potential is turned off. The first task is to solve two initial value problems for Cauchy data (initial data) at time  $t = 0$ . Doing so involves calculating the Fourier decomposition of plane waves from the causal past (time  $t < 0$ ) to the Cauchy data surface. This step was calculated by Mamaev and Trunov in their 1982 paper [14]. The antisymmetric mode solution to the Klein-Gordon equation is,

$$\Phi_{k1}^-(x, t) = \frac{1}{\sqrt{2\pi\omega}} e^{-i\omega t} \sin \sin(kx), \quad (33)$$

and the symmetric mode solution is,

$$\Phi_{k2}^-(x, t) = \frac{1}{\sqrt{2\pi\omega}} e^{-i\omega t} \cos(k|x| + \delta). \quad (34)$$

We calculate the Cauchy data as,

$$\Phi_{k1}^-(x, 0) = \frac{1}{\sqrt{2\pi\omega}} \sin \sin(kx) \quad (35)$$

$$\partial_t \Phi_{k1}^-(x, 0) = \frac{-i\omega}{\sqrt{2\pi\omega}} \sin \sin(kx), \quad (36)$$



for the antisymmetric modes and,

$$\Phi_{k2}^-(x, t) = \frac{1}{\sqrt{2\pi w}} e^{-i\omega t} \cos(k|x| + \delta) \quad (37)$$

$$\partial_t \Phi_{k1}^-(x, 0) = \frac{-i\omega}{\sqrt{2\pi w}} \cos(k|x| + \delta), \quad (38)$$

for the symmetric modes.

The next task is to determine the Fourier coefficients,  $\overline{\alpha(\kappa)}$  and  $\beta(\kappa)$ . We begin by taking the Fourier transform of the functions at the Cauchy surface. Our calculated value for the Fourier coefficients is,

$$\overline{\alpha(\kappa)} = \frac{1}{i2\sqrt{2}} \left( \sqrt{\frac{\omega}{w}} + \sqrt{\frac{w}{\omega}} \right) (\delta(\kappa - k) - \delta(\kappa + k)) \quad (39)$$

$$\beta(\kappa) = \frac{1}{i2\sqrt{2}} \left( \sqrt{\frac{\omega}{w}} - \sqrt{\frac{w}{\omega}} \right) (\delta(\kappa - k) - \delta(\kappa + k)), \quad (40)$$

for the antisymmetric modes and,

$$\overline{\alpha(\kappa)} = \frac{1}{2\sqrt{2\pi}} \left( \sqrt{\frac{\omega}{w}} + \sqrt{\frac{w}{\omega}} \right) \{ \pi \cos \delta [\delta(\kappa - k) + \delta(\kappa + k)] - \frac{2k \sin \delta}{k^2 - \kappa^2} \} \quad (41)$$

$$\beta(\kappa) = \frac{1}{2\sqrt{2\pi}} \left( \sqrt{\frac{\omega}{w}} - \sqrt{\frac{w}{\omega}} \right) \{ \pi \cos \delta [\delta(\kappa - k) + \delta(\kappa + k)] - \frac{2k \sin \delta}{k^2 - \kappa^2} \}, \quad (42)$$

for the symmetric modes. Notice that the Fourier coefficients for the symmetric mode are more complicated than the Fourier coefficients for the antisymmetric mode.

We next calculate the continued evolution of each mode for  $t > 0$ , using the plain wave mode,

$$\Psi_{\kappa}(x, t) = \frac{1}{\sqrt{4\pi\omega}} e^{i(\kappa x - \omega t)}, \quad (43)$$

and the generic solution,

$$\Psi(x, t) = \int_{-\infty}^{+\infty} [\overline{\alpha(\kappa)} \Psi_{\kappa}(x, t) - \beta(\kappa) \Psi_{\kappa}(x, t)] d\kappa \quad (44)$$

where  $\overline{\alpha(\kappa)}$  and  $\beta(\kappa)$  are the Fourier coefficients. The continued evolution of each mode is,

$$\Psi_{(x,t)}^{even} = \frac{1}{\sqrt{2\pi w}} \{ \cos \delta \cos \cos(kx) e^{-i\omega t} \quad (45)$$

$$- \frac{k}{\pi} \sin \delta \int_{-\infty}^{\infty} \frac{d\kappa}{k^2 - \kappa^2} [ \cos \cos(\kappa x - \omega t) + i \frac{w}{\omega} \sin \sin(\kappa x - \omega t) ] \} \quad (46)$$

$$\Psi_{(x,t)}^{odd} = \frac{1}{\sqrt{2\pi w}} \sin \sin(kx) e^{-i\omega t}. \quad (47)$$

Next, we combine the Fourier evolution of the modes and renormalize by subtracting the same expression for  $\lambda = 0$ . We then take the derivative of the Wightman function to find the unrenormalized density,

$$\rho(x, t, x', t') = \frac{1}{2} \left( \partial_t \partial_{t'} + \partial_x \partial_{x'} \right) G(x, t, x', t'), \quad (48)$$

where  $G(x, t, x', t')$  is the Wightman function, explained in the ‘Wightman Axioms’ section.

We then calculate the Fourier transform for IN region plane waves at the Cauchy surface to find the Fourier coefficients of plane waves to the causal future. The result is,

$$\Phi^{OUT}(x, t) = \int_{-\infty}^{\infty} dk [a(k) \psi(k, x, t) + b(k) \psi(k, x, t)], \quad (49)$$

where  $a(k)$  and  $b(k)$  are the Fourier coefficients for the IN region. We find that the number of created particles is proportional to  $|b(k)|^2$ .

We next calculate the mode contributions for the entirety of our two-dimensional spacetime, and find that the antisymmetric mode contribution is,

$$G_{Anti}^+(\vec{x}; \vec{x}') = \frac{1}{2\pi} \int_0^{\infty} dk \frac{1}{w} \sin(kx) e^{-i\omega t} \frac{1}{w} \sin(kx') e^{+i\omega t'}, \quad (50)$$

and the symmetric mode contribution is,

$$G_{Sym}^{+REN}(\vec{x}, \vec{x}') = \frac{1}{2\pi} \int_0^{\infty} \frac{2k}{w} [\cos(\kappa|x| + \delta) \cos(\kappa|x'| + \delta) - \cos(\kappa|x|) \cos(\kappa|x'|)] e^{-i\omega(t-t')}. \quad (51)$$

Note that these results display the renormalized positive frequency Wightman function. The next step is to calculate the expectation value of energy density in the OUT region. We calculate the vacuum expectation value of the stress-energy tensor to be,

$$\langle T_{tt} | 0 \rangle_{ren}(x, t) = \frac{\lambda}{8\pi} [\delta(x+t-\frac{a}{2}) + \delta(x+t+\frac{a}{2}) - \frac{1}{2} [\Theta(x+t+\frac{a}{2}) - \Theta(x+t-\frac{a}{2})]] + \frac{\lambda}{8\pi} [\delta(x-t-\frac{a}{2}) + \delta(x-t+\frac{a}{2}) - \frac{1}{2} [\Theta(x-t+\frac{a}{2}) - \Theta(x-t-\frac{a}{2})]]. \quad (52)$$

Choosing a stationary geodesic at  $x_0$  which is either to the right or the left of the potential, we determine that the energy density is,

$$\rho_{ren}(t) = \langle 0 | T_{tt} | 0 \rangle_{ren}(x_0, t). \quad (53)$$

The left-hand side of the quantum inequality comes from the integration of this expression against Solomon's test function, i.e.

$$LHS = \int_0^{\infty} \rho_{ren}(t) f(t) dt, \quad (54)$$

where,

$$f(t) = \frac{30}{t_0^2} t^2 (t - t_0)^2. \quad (55)$$

Our resulting inequality is,

$$-\frac{5}{3\pi t_0^2} \frac{\lambda}{4\pi a} \left( \frac{27a^5}{10t_0^5} + \frac{25a^3}{4t_0^3} \right) \geq -\frac{5}{3\pi t_0^2}. \quad (56)$$

This result, unlike Solomon's, is always true, as the left-hand side is positive for all values of  $a$  and  $t_0$ . The positive energy pulse on the leading and trailing edges of the traveling negative-energy regions overwhelms the negative energy contributions in the quantum inequality. Therefore, particle creation and the positive energy associated with it play a dominant role in the dynamical model and the spatial quantum inequality is not violated.

## CONCLUSION

Classical energy conditions are mathematical constraints on energy conditions in space and time. In classical physics, the energy conditions constrain energy density to be nonnegative because mass is positive in value. In quantum physics, however, energy density can be negative. The replacements for classical energy conditions, quantum inequalities locally constrain the magnitude and extent of negative energy density in spacetime. Mamaev and Trunov generated a method to calculate the Casimir effect, a physical force arising due to the presence of a quantized field, by calculating the vacuum expectation value of the stress-energy tensor for a relativistic quantum field theory and using a double delta function potential. A paper by Dan Solomon claims that this violates the spatial energy condition; however, Solomon neglected the energy contribution of particle creation to the stress-energy tensor. In this paper, we include the effects of particles created after shutting off the potential at the Cauchy surface and re-calculate the energy contributions to the stress-energy tensor. We do so in a two-dimensional Minkowski spacetime with an external, time-dependent Mamaev-Trunov potential. We find that the spatial quantum inequality is not violated.

## ACKNOWLEDGMENTS

I would like to thank my research advisor, Dr. Michael Pfenning, for sharing his expertise and assistance with me during the research process.

## REFERENCES

1. D.J. Griffiths and D.F. Schroeter, *Introduction to quantum mechanics* (Cambridge University Press, 2018).
2. B. Hall, *Quantum theory for mathematicians* (Springer, 2013).
3. D.J. Wineland, *Reviews of Modern Physics*, **85**(3), 1103 (2013).
4. A. Weiner, *Ultrafast optics* (John Wiley & Sons, 2011).
5. C.L. Herzenberg, preprint arXiv:0706.1467 [physics.gen-ph] (2007).
6. J.D. Jackson, *Classical electrodynamics* (1999).
7. M.J. Pfenning and L.H. Ford, *Physical Review D*, **57**(6), p.3489 (1998).
8. E. Schrödinger, *Die Naturwissenschaften*, **28**, pp.664-666 (1926).
9. É.É. Flanagan, *Physical Review D*, **56**(8), p.4922 (1997).
10. D. Solomon, preprint arXiv:1003.1526 [quant-ph] (2010).

11. S.G. Mamaev and N.N. Trunov, Soviet Physics Journal, **24**(2), pp.171-174 (1981).
12. N. Graham, R.L. Jaffe, V. Khemani, M. Quandt, M. Scandurra, and H. Weigel, Nuclear Physics B, **645**(1-2), pp.49-84 (2002).
13. M.J. Pfenning, Physical Review D, **98**(6), p.065004 (2018).
14. S.G. Mamaev and N.N. Trunov, Yadernaya Fizika, **35**(4), pp.1049-1058 (1982).
15. M. Schottenloher, "Axioms of Relativistic Quantum Field Theory," in *A Mathematical Introduction to Conformal Field Theory. Lecture Notes in Physics*, (Springer, Berlin, Heidelberg, 2008), Vol. 759, [https://doi.org/10.1007/978-3-540-68628-6\\_8](https://doi.org/10.1007/978-3-540-68628-6_8).

# SPS Summer Internships

The SPS summer internship offers 10-week long positions in:

- Science Policy
- Communication
- Research
- Education
- Outreach



Applications due  
**January 15**



All internships include paid housing, a competitive stipend, a commuting allowance, and transportation to and from Washington, DC.

For more information and to view the previous work and journal entries of SPS interns, please visit [spsnational.org/programs/internships](https://spsnational.org/programs/internships).



# Probing the Energy Gaps of a Multi-Gap Superconductor: $\text{Ba}_{(1-x)}\text{K}_x\text{Fe}_2\text{As}_2$

Keeran Ramanathan, Luke Conover, Oberon Wackwitz, and Roberto Ramos

*University of the Sciences, Philadelphia, PA, 19104, USA*

<sup>a)</sup>Corresponding author: r.ramos@usciences.edu

**Abstract.** In order to spectroscopically probe the superconducting energy gap of potassium-doped Ba122 iron pnictides, in particular  $\text{Ba}_{(1-x)}\text{K}_x\text{Fe}_2\text{As}_2$  where  $x = 0.33$  (under-doped regime), we have performed four-wire conductance measurements from  $T = 2\text{K}$  to  $52\text{K}$ . We report evidence for multi-gap features with gaps corresponding to directional tunneling through the  $ab$ - axes of this iron pnictide. The multi-gap features a predominant result of tunneling across the  $ab$ - plane with gaps of  $\Delta_1 = 2\text{-}4\text{ meV}$  and  $\Delta_2 = 9\text{-}11\text{ meV}$ . These gap values are temperature dependent.

## INTRODUCTION

Multi-band superconductors, such as the iron pnictides, can exhibit multiple energy gaps depending on the crystal growth conditions and on which tunneling directions are made accessible by the sample fabrication process.<sup>1</sup> The energy gaps are often anisotropic with respect to the crystal lattice, corresponding to superconductivity along directions parallel or perpendicular to the  $c$ -axis of the lattice.<sup>1,2</sup> We present and discuss results of measurements of the energy gaps of single crystals of iron pnictides (K-doped Ba-based 122 family) using point contact spectroscopy.

Transport through a point contact is classified into three separate regimes: diffusive, quantum, and ballistic.<sup>3</sup> Each regime correlates to the contact diameter  $a$  and the electronic mean free path  $l$  of the contact material; the mean free path stems from the successive elastic and inelastic scattering of electrons. In the diffusive regime, the sample size is much larger than the mean free path so that transport is independent of the form of the system. In the quantum regime, the sample is similar to the mean free path so that edge and boundary effects dominate. In the ballistic regime, the charge carriers make ballistic motion while boundaries play the role of scatterer. Spectra such as the superconducting energy gap has been shown to be readable from point contact data if the interface between normal metal leads and the superconductor is in the ballistic regime, when heating effects are minimized.<sup>4</sup> It has been recently demonstrated that if the junction size is reduced to the ballistic regime, where the electron mean path is longer than the junction size, that conductance measurements using PCS (Point Contact Spectroscopy) can be reduced to a simpler tunneling model. This allows the PCS technique to sample the effective density of states obtained from integrating over the whole Fermi surface, and has been appropriately applied to iron pnictides that behave like a non-Fermi liquid.<sup>4</sup>

Our measurements that use nanometer-size gold wires pressed against crystals are ideally within the ballistic regime. Features such as Andreev reflections occur within the point-contact between a normal metal  $N$  and a superconductor  $S$ , and is a charge-transfer process by which normal current in  $N$  is converted to supercurrent in  $S$ .<sup>1</sup> When the electronic energy of the applied voltage is within the value of the superconducting gap (Fermi level of the superconductor), the electron is physically not allowed to tunnel across the two-state junction and as a result, a cooper pair is formed within the superconductor while a hole is reflected back inside the normal metal. Thus, identifying Andreev reflections can reveal spectroscopic properties of the superconductor.<sup>4</sup> More generally, measuring the differential conductance  $dI/dV$  as a function of applied voltage  $V$ , which is a direct measure of the superconducting energy gap, can show the important spectroscopic properties of the superconductor and give insight into the mechanisms driving superconductivity in these materials. This allows for the probing of single- and multi-gap structures of superconductors and serves as the basis for point-contact spectroscopy.

## EXPERIMENTAL PROCEDURE

Single crystals of  $\text{Ba}_{0.67}\text{K}_{0.33}\text{Fe}_2\text{As}_2$  of high crystalline quality were obtained from collaborators who had grown samples by using the self-flux method with FeAs as flux, as described in the literature.<sup>5</sup> The crystals were then cleaved by means of mechanical exfoliation using Scotch tape, to produce a fresh, shiny surface. To prepare the samples for current-voltage measurements, four soft point contacts were made by controlled application of silver paint on nanometer-diameter gold wires set upon the crystals mounted on a copper platform.

Four contacts were made in order to implement four-wire measurement technique designed to eliminate contributions from lead resistances.<sup>6</sup> To access the *ab*- and *c*-axes simultaneously through the crystal, V-shaped gold wires connecting the point contact are oriented between 30-45° relative to the copper platform.

The sample was then mounted onto a custom-built sample holder thermally anchored using black Stycast Epoxy on the second stage cold finger of a Janis Cryocooler with a base temperature of 2 Kelvin. The second stage is covered by a metal shroud that acts doubles as a 2 Kelvin radiation shield, which is then covered with a vacuum can pumped down with an Edwards TS-75 turbomolecular pump.

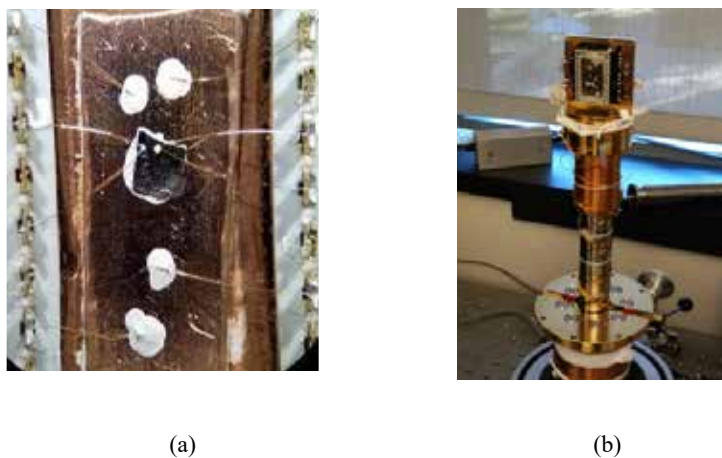


**FIGURE 1:** (a) The Iron Pnictide Crystal sample (~2mm across) was mounted on a copper platform. Soft point contacts were made using nm-sized gold wire and silver paint (white dots centered on iron pnictide crystal). (b) The sample holder was thermally anchored to the second stage of a Janis Cryocooler.

At base temperature, a current bias was provided by a ramped waveform generator and the voltage response and conductance were measured through two Stanford SR830 low-noise lock-in amplifiers to reduce external noise and produce high resolution measurements. A temperature series of conductance as a function of voltage was collected through a data acquisition device (DAQ) and controlled through Labview and analyzed using Python.

## RESULTS AND DISCUSSION

Using the four-wire approach, the resistance of the under-doped iron pnictide  $\text{Ba}_{(1-x)}\text{K}_{(x)}\text{Fe}_2\text{As}_2$  where  $x = 0.33$ , was measured and found to have a superconducting critical temperature of 38 Kelvin. This can be observed in Figure 2, where there is a dramatic change in the magnitude and sharpness of the conductance curve  $dI/dV$  vs  $V$ . For temperatures at and below  $T_c = 38$  Kelvin, there is marked enhancement of conductance in the form of a peak while below  $T_c$ , the signal becomes rounded and progressively reduced. Furthermore, a temperature series of the conductance measurements from 2.0 – 52.0 Kelvin show features in the form of a broad shoulder and a peak. These features – enhancements in conductance are typically interpreted to correspond to superconducting energy gaps, in this case, a small gap  $\Delta_1$  symmetric about 2-4 meV and a large gap  $\Delta_2$  symmetric about 9-11 meV (See Figure 2). These two predominant features for  $\text{Ba}_{0.67}\text{K}_{0.33}\text{Fe}_2\text{As}_2$  are consistent with two flavors of tunneling along the *ab* plane. The insets of Figure 2 show that the peaks move with temperature, which is characteristic of the temperature dependence of conventional superconducting energy gaps.<sup>1</sup> Looking at the literature, these results are very similar to data from *P. Samuely et al.*<sup>7</sup> that report two energy gaps with similar values for a nominally similar composition of  $\text{Ba}_{0.55}\text{K}_{0.45}\text{Fe}_2\text{As}_2$  at temperatures below its  $T_c$  of 30K. In 2008, *Gonnelli et al.*<sup>9</sup> also obtained two-gap spectra on



the  $\text{LaFeAsO}_{1-x}\text{F}_x$  polycrystals that compare remarkably well with these values. In addition, two-gap spectra were also observed in under-doped  $\text{Ba}_{(1-x)}\text{K}_{(x)}\text{Fe}_2\text{As}_2$  using Raman scattering.<sup>9</sup> On the other hand, there have been observations of only single energy gap features, using STM, in iron pnictides that are doped with cobalt<sup>10</sup> and potassium.<sup>11</sup>

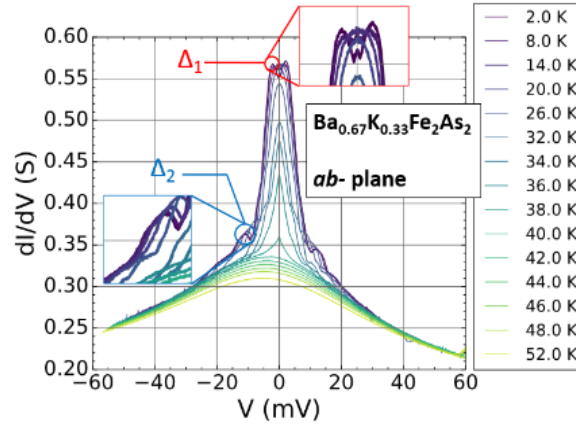


**FIGURE 2:** Data for Differential Conductance  $dI/dV$  vs Voltage  $V$  of iron pnictide  $\text{Ba}_{(1-x)}\text{K}_{(x)}\text{Fe}_2\text{As}_2$  where  $x = 0.33$  (under-doped regime) and  $T = 2.0 \text{ K}$  to  $52.0 \text{ K}$ . Two gap values  $\Delta_1$  at 2-4 meV and  $\Delta_2$  at 9-11 meV are suggested by the shoulders and bumps on the conductance curves. Similar features have been observed in the literature for other superconductors. The two insets show that within each gap, peaks move with temperature, which is characteristic of conventional superconducting energy gaps.

## CONCLUSION AND FUTURE WORK

We have performed PCS measurements on under-doped iron pnictide  $\text{Ba}_{0.67}\text{K}_{0.33}\text{Fe}_2\text{As}_2$  and observed two temperature-dependent features that correspond to gap values: a small  $\Delta_1 = 2\text{-}4 \text{ meV}$ , and a large gap,  $\Delta_2 = 9\text{-}11 \text{ meV}$ . For future work, we will plot the normalized superconducting energy gap values  $\Delta(T)/\Delta(0)$ , where  $\Delta(0)$  is the gap at zero temperature, that should decrease with  $T/T_c$ , and compare with results of other research. We plan to determine the common underlying factor shared by various superconductors studied by different groups that exhibit these similar two-gap structures. Towards this, we plan to measure more doping regimes of potassium-based iron pnictide and other doping types of iron pnictides such as phosphorus and cobalt.

## ACKNOWLEDGEMENTS

We acknowledge Joseph Lambert (National Radio Astronomy Observatory) for help with setting our experimental apparatus. We gratefully acknowledge our collaborators from Rice University, Pencheng Dai, Chengling Zhang, Yu Song, and Guotai Tai, for providing us with high-quality iron pnictide single-crystals. Finally, we acknowledge support from the National Science Foundation Grant DMR-1555775 and the Charles Kaufman Foundation.

## REFERENCES

1. X.Zhang, Y.-S. Oh, Y. Liu, L. Yan, S.R. Saha, N.P. Butch, K. Kirshenbaum, K.H. Kim, J. Paglione, R.L. Greene, and I.Takeuchi, *Physical Review B* **82**, 020515 (2010)
2. P. Szabó, Z. Pribulová, G. Pristáš, S. L. Bud'ko, P. C. Canfield, and P. Samuely, *Physical Review B* **79**, 012503 (2009).
3. W.R. Clarke, M.Y. Simmons, and C.-T. Liang, *Comprehensive Semiconductor Science and Technology* **1**, 279, (2011).
4. W.-C. Lee, W.K. Park, H.Z. Arham, L. H. Greene, and P. Phillips, *Proceedings of the National Academy of Sciences of the United States of America* **112**(3), 651-656 (2015).



5. B. Shen, H. Yang, Z-S. Wang, F. Han, B. Zeng, L. Shan, C. Ren, and H.-H. Wen, *Physical Review B* **84**, 184512 (2011).
6. R. Richardson, *Experimental Techniques In Condensed Matter Physics At Low Temperatures* (CRC Press, 2019).
7. P. Samuely, Z. Pribulová, P. Szabó, G. Pristáš, S. L. Bud'ko, P. C. Canfield, *Physica C*, **469**(9-12), 507 (2009).
8. S.-F. Wu, P. Richard, H. Ding, H.-H. Wen, G. Tan, M. Wang, C. Zhang, P. Dai, and G. Blumberg, *Physical Review B* **95**, 085125 (2017).
9. R. S. Gonnelli, D. Daghero, M. Tortello, G. A. Ummarino, V. A. Stepanov, J. S. Kim, and R. K. Kremer, "Coexistence of two order parameters and a pseudogaplike feature in the iron-based superconductor  $\text{LaFeAsO}_{(1-x)\text{F}_x}$ ," arXiv:0807.3149 (unpublished).
10. Yi Yin, M. Zech, T. L. Williams, X. F. Wang, G. Wu, X. H. Chen, and J. E. Hoffman, *Physical Review Letters* **102**, 097002 (2009).
11. M. C. Boyer, Kamallesh Chatterjee, W. D. Wise, G. F. Chen, J. L. Luo, N. L. Wang, E. W. Hudson, "Scanning tunneling microscopy of the 32 K superconductor  $(\text{Sr}_{1-x}\text{K}_x)\text{Fe}_2\text{As}_2$ ," arXiv:0806.4400 (unpublished).

With an SPS Membership, you will gain access to our awards system to apply for scholarships, internships, research grants, and many other benefits!



# Photometric Study of RR Lyrae Star TV Lyn

She'Kayla Love,<sup>1, a)</sup> Dr. Susmita Hazra,<sup>1, b)</sup> and Dr. Michael Fitzgerald<sup>2, c)</sup>

<sup>1</sup> Department of Chemistry, Physics, and Engineering, Cameron University, Lawton, OK, USA

<sup>2</sup> Edith Cowan Institute for Education Research, School of Education, Edith Cowan University, Joondalup, WA, Australia

<sup>a)</sup> Corresponding author: shekayla.love@cameron.edu

<sup>b)</sup> shazra@cameron.edu

**Abstract.** In this research, we are reporting the light curve of RR Lyrae type variable star TV Lyn. This star is observed in the northern hemisphere and its coordinates are 07:33:31.7 +47:48:09.8. We have used data from Las Cumbres Observatory (LCO) which consists of a worldwide network of robotic telescopes. Photometric measurements were conducted using the SBIG 6303 0.4-meter telescope with a field of view of 29'x19'. Depending on what the color of a star is when different filters are applied to it, the luminosity will change accordingly. Our data consists of four filters, Bessell B (Blue), Bessell V (visual), SDSS-I (Infrared), and PAN-STARRS-Z (Near Infrared). Results show that this star has a variability period of  $0.2407 \pm 0.002$  days, metallicity -1.49, and located at a distance of  $1362 \pm 118$  pc. We have used an estimate of the reddening  $E(B-V)$  as 0.08. This research is a part of an Our Solar Sibling Project by an undergraduate student with the help of a faculty advisor and an Our Solar Sibling Project Investigator.

## INTRODUCTION

RR Lyrae type stars are one of the brightest representative variable stars in the galaxy. They are variable stars since they pulsate. These stars are older than 10 Giga-years. They are typically low mass and found within an instability strip with a temperature ranging from 6000 K to 7250 K [1]. They change internal temperature due to being compressed by gravity which causes photons to be trapped inside the star, making the temperature rise. This increases pressure within the star, which then makes the gas expand allowing the photons to escape and the pressure to release. The study of these stars can provide us information on the distance and properties of star clusters. Their brightness can range from a thousandth of a magnitude to as much as twenty magnitudes over periods of a fraction of a second to years, depending on the size. There are over 150,000 RR Lyrae stars known and catalogued, and many more are suspected to be RR Lyrae stars. The study of variable stars allows us to study the universe because stars are the primary engines of cosmic evolution. Variable stars teach us about stellar properties such as mass, radius, luminosity, temperature, composition, and evolution. There are many types of variable stars such as Cepheid variables, Mira variables, and cataclysmic variables. Cepheid type variable stars play a major part in determining distances to far away galaxies and determining the age of the universe. Mira variables allow us to analyze the evolution of stars and Accretion disks help us to understand disk behavior [2,3].

Study of RR Lyrae stars can provide important information on chemical compositions and dynamical properties of old stellar populations. RR Lyrae stars in Galactic globular cluster (GC) systems are of particular importance to address the question of the early history and structure of our Galaxy [2]. Drake et al. [4,5] and Pietrukowicz et al. [6] have used RR Lyrae stars to understand the substructures in the Galactic halo expected from the theory of the hierarchical structure formation and to delineate the bar structure in the central part of our Galaxy. Lee et al (2014) have presented a high-precision BV CCD photometry of RR Lyrae stars in NGC 6723 galaxy [7]. They studied the

RR Lyrae star population in NGC 6723 and estimated the distance scale. Fitzgerald et al [8] have used photometric methods to study open cluster NGC 2215.

This research focuses on RR Lyrae type variable star TV Lyn located in Lynx constellation and in NGC 2770 galaxy in the northern celestial hemisphere. The coordinates of TV Lyn are: 07:33:31.7 +47:48:09.8. The light-curve of a stellar object is important for astronomical research and studying this star can provide concepts of distance scale, formation process of the galaxy, age, stellar content, and metallicity [8].

## OBSERVATIONS

We have used photometric analysis to obtain the light-curve of the variable star TV Lyn. Photometry is the measurement of brightness. Time series photometer monitors the light variation from an astronomical object over the time. The data contains a series of images of a stellar object over the time, typically over different color filters to extract different brightnesses [10]. Inner and outer sky annulus and the size of the photometry aperture are three main parameters for photometric analysis. The inner radius needs to be large enough to include all light from the star but not too much of the sky. The outer radius determines the size of the sky annulus, this is important because the sky is a variable and changes over short time intervals. Aperture size of the star can be calculated by counting the pixels that form the center of the star.



**FIGURE 1.** TV Lyn on a night sky! (Courtesy: Las Cumbres Observatory; FOV: 29'x19' )

For better representation of the images of celestial bodies from telescopes, astronomers usually place a unique piece of colored glass into the path of light called a filter. Astronomical filters allow light of different wavelengths to pass through while also blocking unwanted wavelengths. Any set of color filters with known light transmission properties is called a photometric system. At present, there are over 200 photometric systems. There are two types of color filters: wide band and narrow band filters. Visible light photometry most commonly uses wide band filters by the names of U, B, V, R, and I [10]. The U filter stands for ultraviolet and allows light of wavelengths about 320 nm and 400 nm to pass through. The B filter stands for blue and allows light of wavelengths about 400nm and 500 nm. The V, R, and I filters stand for visible, red, and infrared and their respective wavelength ranges are 500-700 nm, 550-800 nm, 700-900 nm.

For this research, we initially have used images of the star TV Lyn from Las Cumbres Observatory (LCO) over the course of 5 days in U, B, I, and V filters. Figure 1 shows an image of TV Lyn in the night sky with a field of view of 29'x19', courtesy of our LCO telescope data. Each filter needs a specific exposure time in order to give the best quality, therefore, the 4 test images had base exposure times of 12 to 30 seconds. We were able to calculate the desired exposure times of TV Lyn and requested 2 weeks of data during the period of January 2020 with new exposure times B: 40s, V: 5s, I: 20s, and Z: 70s. LCO's SBIG 6303 telescope recorded the light from TV Lyn with a CCD camera with a pixel scale of 0.571 (bin 1x1). This telescope has an aperture of 0.4 m. Around 50 images were received and placed in a google drive folder by the Our Solar Sibling Project Investigator. As a part of the Solar Sibling project, a series of automated python scripts were provided by Michael Fitzgerald to calculate time period from the light curve by observing how bright the standard stars comparable in size to TV Lyn are and plotting it as

phase vs magnitude. The python scripts also allowed us to observe apparent magnitude and metallicity of the variable star in different filters. Some of the standard stars used to observe TV Lyn's brightness were: LP 162-33, TYC 3409-2065-1, TYC 3409-2187-1, and BD+48 1546 with Bessell B magnitudes of 11.7, 18.7, 12.8, 12.1, and 11.1 respectively.

We obtained four light curves for the star TV Lyn for the filters B, V, I, and Z. The details of these light curves are discussed in the results section of this paper.

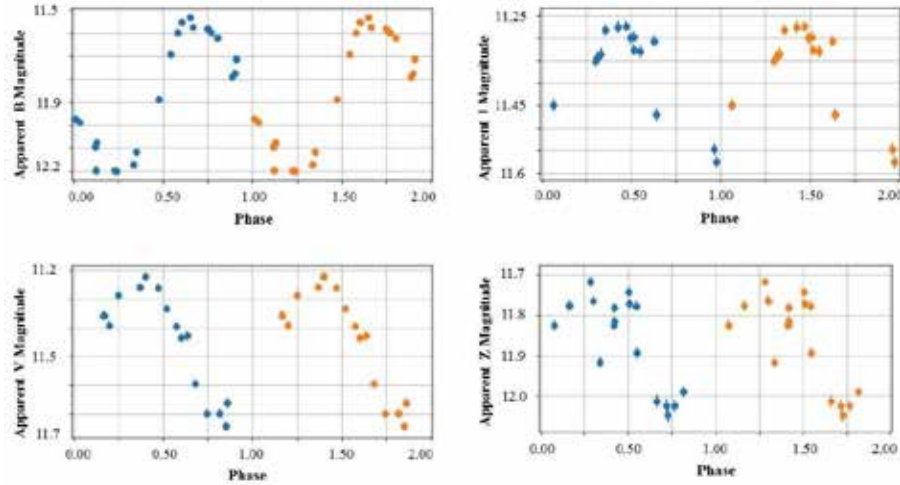


**FIGURE 2.** Light curves of RR Lyrae star TV Lyn over two cycles in B, V, I, and Z filters

## RESULTS

Figure 2 shows the light curves of the star TV Lyn for two cycles of most likely period with error bars in B, V, I, and Z filters. The error bars should be based on the variations of the differences between the comparison and check star magnitudes. Actual error could be more than that though, due to external factors. Based on the shape of the sinusoidal graph, we classify TV Lyn as an RRc variable star [11]. The time period of the star in different filters, with standard deviations, are shown in Table 1. Theoretical period-luminosity of the RR Lyrae stars were used from Catelan et al [1] and Caceres and Catelan [12].

$$M_v = 2.288 + 0.882 \log Z + 0.108 (\log Z)^2 \quad (1)$$

$$M_i = 0.908 - 1.035 \log P + 0.220 \log Z \quad (2)$$

$$M_z = 0.839 - 1.295 \log P + 0.211 \log Z \quad (3)$$

$$\log Z = \left[ \frac{M}{H} \right] - 1.765 \quad (4)$$

$$\left[ \frac{M}{H} \right] = \left[ \frac{Fe}{H} \right] + \log(0.638f + 0.362) \quad (5)$$

Where  $f = 10^{0.3}$  (as provided by Our Solar Sibling project),  $M_v$ ,  $M_i$ , and  $M_z$  are the absolute magnitude in V, I, Z filters.  $P$  is the pulsation period,  $Z$  is metallicity. We have used metallicity  $Fe/H$  value as -1.490 (as provided by Our Solar Sibling project). Absolute magnitudes are calculated using metallicity ( $Z$ ) and time periods using equations 1, 2, and 3. We received excel files from the python scripts containing calibrated TV Lyn magnitudes as well as differential magnitudes. Calibrated magnitudes are exact measurements of a celestial object, whereas differential magnitudes are more variable because their brightness is being compared with nearby stars of similar magnitude.

The average time period of all the filters is around 0.24 days with an error estimate of 0.003 days. The luminosity is calculated with the average of maximum and minimum values of magnitudes. For B it is  $11.87 \pm 0.057$ , for V it is  $11.43 \pm 0.025$ , for I it is  $11.34 \pm 0.018$ , and for Z it is  $11.88 \pm 0.011$ . Table 1 shows all the time period data with standard deviation. In our data we have used an estimate of reddening  $E(B-V)$  as 0.08 based on minimum variance in distance among V, I, and Z filters. The distance (d) of the star TV Lyn in parsec is calculated using the theoretical relation between absolute magnitude (M) and apparent magnitude (m) are shown in Table 2.

$$m - M = 5 \log d - 5 \tag{6}$$

$$d = 10^{((m-M+5)/5)} \tag{7}$$

**TABLE 1.** Time periods in B, V, I, Z filters with standard deviation

Filter	Wavelength	Period	Standard Deviation
B (Blue)	400-500 nm	0.2407 days	0.002 days
V (Visible)	500-700 nm	0.2407 days	0.002 days
I (Infrared)	700-900 nm	0.2407 days	0.002 days
Z (Near Infrared)	~900 nm	0.2406 days	0.002 days

**TABLE 2.** Comparison of distances in V, I, and Z filters with GAIA.

	Distance (parsecs)	Error (parsecs)
<b>GAIA</b>	1219	73.5
<b>V</b>	1362	118
<b>I</b>	1252	73
<b>Z</b>	1564	64
<b>Average (V, I, Z)</b>	1393	49

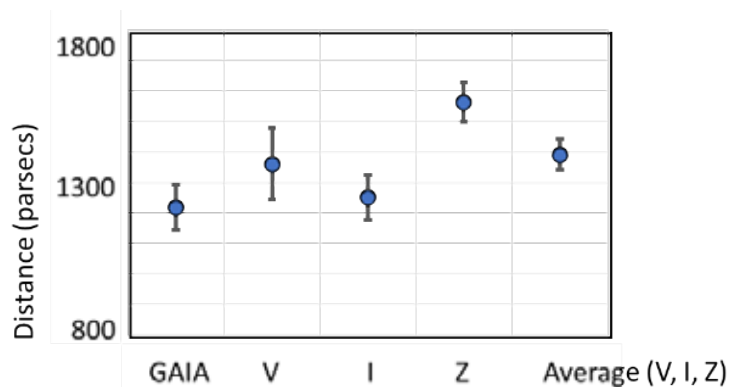


**FIGURE 3.** Comparison of TV Lyn distance from LCO data with GAIA telescope.

Table 2 and Fig. 3 show the comparison of the star TV Lyn distance in V, Z, I with GAIA distance. GAIA is a space observatory that measures the distance, position, and motion of the stars. V and I distance measurements agree with GAIA distance within the error limit, whereas Z and Average do not [13,14].

## CONCLUSION

In this paper, we have studied the light curve of the variable star TV Lyn. We have measured the time period of variation, distance, luminosity, and metallicity using the robotic telescope data from LCO. Our data shows that TV Lyn is an RRc type variable star with a periodicity of 0.2407 days. The distance of the star is 1362 parsecs. The luminosity of the star is 11.87 Watts and metallicity is -1.49. These results are consistent with results presented in Cohen et al [15] and Fitzgerald [10] for other RR Lyrae stars. One of the sources of error is estimation of reddening  $E(B-V)$ . A change of  $E(B-V)$  by 0.03 leads to 8% to 13% of distance error in V filter [9].

## ACKNOWLEDGMENTS

This work is a part of Our Solar Sibling Project. This work makes use of observations from the Las Cumbres Observatory global telescope network. This research has made use of "Aladin sky atlas" developed at CDS, Strasbourg Observatory, France. We thank the reviewer for reviewing this paper. We acknowledge Cameron University for supporting this research work.

## REFERENCES

1. M. Catelan, B.J. Pritzl, and H.A. Smith, The Astrophysical Journal Supplement Series **154**(2), 633 (2004).
2. H.A. Smith, *Rr lyrae stars Vol. 27*. (Cambridge University Press, 2004).
3. A.W. Harris, B.D. Warner, and P. Pravec, Asteroid Lightcurve Derived Data V16.0. NASA Planetary Data System, EAR-A-5- DDR-DERIVED-LIGHTCURVE-V16.0 (2016).
4. A. Drake, M. Catelan, S. Djorgovski, G. Torrealba, M. Graham, V. Belokurov, et al, The Astrophysical Journal **763**(1), 32 (2013).
5. D. L. Davids, "Recovery effects in binary aluminum alloys," Ph.D. thesis, Harvard University, 1998.
6. P. Pietrukowicz, A. Udalski, I. Soszynski, D. Nataf., R. Poleski, S. Kozłowski, et al, The Astrophysical Journal **750**(2), 169 (2012).
7. Burke, C. J., Bryson, S. T., Mullally, F., Rowe, J. F., Christiansen, J. L., Thompson, S. E., et al., The Astrophysical Journal Supplement Series **210**(2), 19 (2014).



8. T. Fitzgerald, L. Inwood, D.H. McKinnon, W. Dias, M. Sacchi, B. Scott., R. Edwards, *The Astronomical Journal* **149**(6), 190 (2015).
9. G. Clementini, L. Federici, C. Corsi, C. Cacciari, M. Bellazzini, and H.A. Smith, *The Astrophysical Journal Letters*, **559**(2), L109 (2001).
10. M.S. Bessell, *Annu. Rev. Astron. Astrophys.* **43**, 293–336 (2005).
11. M.T. Fitzgerald, J. Criss, T. Lukaszewicz, D.J. Frew, M. Catelan, S. Woodward, D.H. McKinnon, *Publications of the Astronomical Society of Australia* **29**(1), 72–77 (2012).
12. C. Cáceres and M. Catelan, *The Astrophysical Journal Supplement Series* **179**(1), 242 (2008).
13. A.G. Brown, A. Vallenari, T. Prusti, J. De Bruijne, F. Mignard, R. Drimmel, et al., *Astronomy & Astrophysics* **595**, A2 (2016).
14. T.L. Astraatmadja, and C.A. Bailer-Jones, *The Astrophysical Journal* **833**(1), 119 (2016).
15. J.G. Cohen, *The Astrophysical Journal* **740**(2), L38 (2011).

# Viscoelastic Relaxation of the Nuclear Envelope Does Not Cause the Collapse of the Spindle After Ablation in *S. pombe*

Parsa Zareiesfandabadi<sup>1, a)</sup> and Mary Williard Elting<sup>1, 2</sup>

<sup>1)</sup>Department of Physics, North Carolina State University, Raleigh, NC 27695, USA

<sup>2)</sup>Cluster on Quantitative and Computational Developmental Biology, North Carolina State University, Raleigh, NC 27695, USA

<sup>a)</sup>Corresponding author: pzareie@ncsu.edu

**Abstract.** A large molecular machine called the mitotic spindle is responsible for accurate chromosome segregation in eukaryotic cells. The spindle consists of protein filaments known as microtubules and microtubule-associated proteins such as motors and crosslinkers, which help impart its organization. In the case of the fission yeast *S. pombe*, these form a single bundle inside the nucleus. During spindle elongation, sliding by motor proteins provides an internal source of extensile forces, which are resisted by the compressive forces of the nuclear envelope. To probe the sources of this force balance, we cut the spindle using focused laser light at various stages of spindle elongation. We find that the spindle pole bodies collapse toward each other post-ablation. While this basic behavior has been previously observed, many questions remain about the timing, mechanics, and molecular requirements of this phenomenon. Here, we quantify the time scale of the relaxation and probe its underlying mechanism. We demonstrate that viscoelastic relaxation of the nuclear envelope cannot explain this phenomenon and provide evidence of active forces as the underlying mechanism.

## INTRODUCTION

The mitotic spindle machinery is highly conserved across all eukaryotes, likely due to its critical functional role of accurately segregating chromosomes between the two daughter cells, ensuring that both have identical genetic information. The fission yeast *Schizosaccharomyces pombe* is an important model organism used in the study of eukaryotic cell division because it achieves chromosome segregation with a relatively simple spindle that is stereotyped cell to cell and because of its well-developed genetic toolkit. These features make it an ideal model system for the mechanical perturbation of the spindle. *S. pombe* undergoes a closed cell division process [1, 2] - wherein its nuclear envelope remains intact - that can be categorized into four morphologically distinct phases defined by the spindle length and rate of elongation [3]: 1- prophase and spindle formation; 2- metaphase and anaphase A; 3- anaphase B and spindle breakdown. The mitotic spindle (Fig. 1a) is assembled from a single bundle of microtubules [4] and microtubule-associated proteins. The elongation phase of the spindle (phase 3) is mainly driven by sliding apart the interdigitating microtubules at the spindle midzone via motor proteins [4, 5, 6, 7]. This is a crucial step to move the segregated chromosomes as far as possible from each other before the cell itself divides in two.

In the past few decades, laser microsurgery coupled with the use of GFP (green fluorescent protein)-based protein markers have been developed as a powerful technique to observe the mechanical response to a controlled intracellular perturbation. This approach allows thorough ablation of cellular structures within a spatial resolution of  $\sim 500$  nm and temporal resolution on the order of seconds with minimal off-target damage to the cell [8]. This technique has previously been used to probe force balance in the *S. pombe* spindle, and it was observed that ablation was followed by the collapse of the spindle [9, 10]. This previous work hypothesized that extensile forces within the spindle resist compressive forces of nuclear envelope and DNA, leading to the collapse of the spindle after spindle ablation. Here, we probe this hypothesis by measuring the shape change of the nucleus following ablation. Surprisingly, we find that the nuclear envelope's viscoelastic relaxation fails to account for the spindle collapse. Instead, the change of nuclear shape that we observe suggests active pulling from inside the nucleus.

## MATERIALS AND METHODS

*Schizosaccharomyces pombe* strains used in this study are PZ2: h+ GFP-atb2:kanMX ade6- leu1-32 ura4-D18 and PZ20: h+ nmt41-GFP-atb2:hpnMX6 + cut11-meGFP:kanMX6. The sources of PZ2 and PZ20 are Chang Lab stock FC2861 and a gift of Caroline Laplante, respectively. For growth conditions and media preparations, we adapted previously described methods [11]. For imaging, we inoculated cultures from YE5S agar plates into YE5S media and grew at 25 °C for 12-24 hours before imaging. For PZ20, we then washed three times with EMM5S and further grew for 6-18 hours in EMM5S liquid media before imaging.

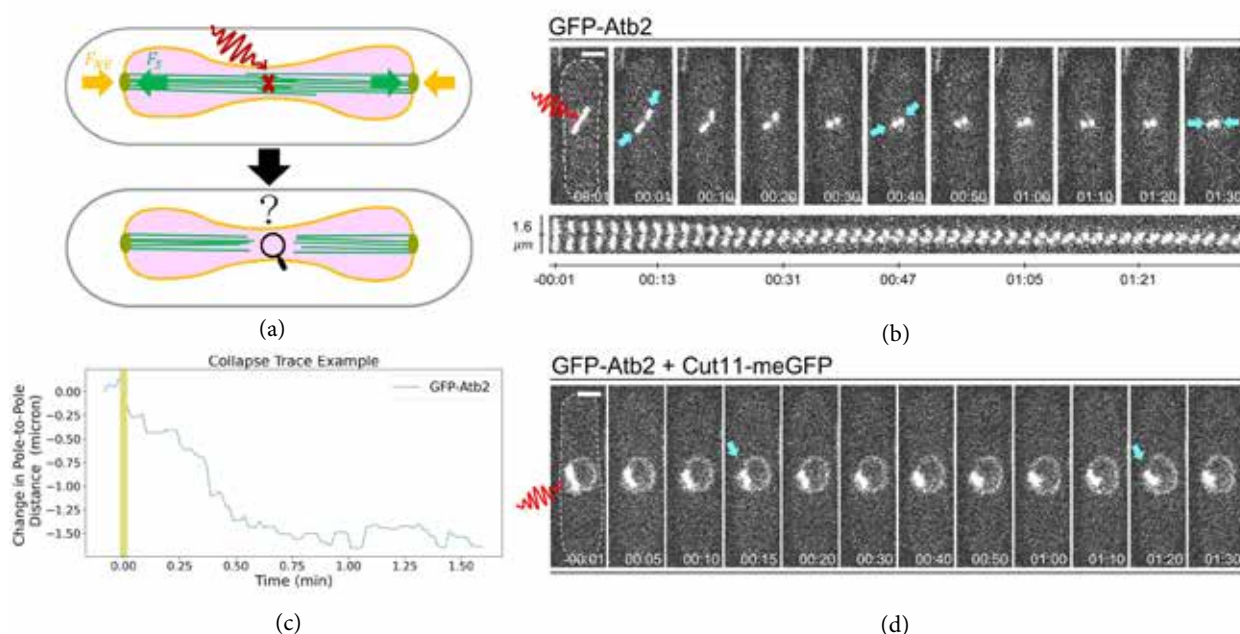


**FIGURE 1.** The response of the mitotic spindle to laser ablation and its effect on the nuclear envelope. (a) Experimental schematic. To cut the spindle, we target the spindle microtubules (green) in a nucleus (magenta) for laser ablation (red X) and track the response of the spindle, the nuclear envelope (orange), and the spindle pole bodies (lime). Arrows indicate the presumed compressive force of the nuclear envelope oppose by the extensile force of spindle elongation. (b) Example ablation of spindle expressing GFP-Atb2 (alpha-tubulin) during phase two of mitosis. Spindle ends (cyan arrows) collapse toward each other after ablation. Top, highlighted frames; below, a montage of the spindle following ablation. (c) Change in the pole-to-pole distance overtime for the example in (b). (d) Example ablation of spindle expressing GFP-Atb2 and Cut11-meGFP ablated near the midzone during phase two of mitosis. Cyan arrows mark the dents appearing at the nuclear envelope and cytoplasm boundary, indicating inward pulling forces after ablation. (b) and (d) Dashed lines in the first frames indicate the cell boundary. Scale bars,  $2\mu\text{m}$ . Timestamps, min:sec. We are unable to image during ablation, and the yellow shaded region in (c) indicates this period.

We prepared imaging slides by using a gelatin or agar pad on a microscope glass slide as previously described [12]. We then centrifuged 1 mL of culture at log phase (verified by measuring optical density) at 3000 RCF using a table-top centrifuge, decanted the supernatant, and resuspended the pellet in  $20\mu\text{L}$  of media. We placed  $5\mu\text{L}$  of resuspended culture on the pad, covered with a coverslip, and sealed with VALAP (1:1:1 Vaseline:lanolin:paraffin).

We performed all imaging at  $22^\circ\text{C}$  on a Nikon Ti-E stand equipped with an Andor Dragonfly spinning disk confocal fluorescence microscope for GFP imaging and an Andor Micropoint with galvo-controlled steering to deliver 10-15 ns pulses at 20 Hz using a 551 nm dye laser as previously described [13, 14].

We performed image analysis using ImageJ to crop and adjust brightness and contrast in all images. We also used ImageJ to convert the cropped .tif files to .avi for further analysis. We used linear adjustment for brightness and contrast and did not use interpolation or compression at any stage. After the initial cropping and adjustment with ImageJ, we performed all further analyses using home-built Python codes using the Jupyter notebook environment (available upon request). Our software loads in the cropped image stacks as .avi files, records the locations of the distal (presumed spindle pole body) ends of the spindles by manual tracking, and calculates the end-to-end Cartesian distance over time between these two tracked ends.

## RESULTS AND DISCUSSION

To investigate the origin of force balance of the mitotic spindle, we ablated the elongating spindles of live *S. pombe* in  $n = 73$  cells expressing GFP-Atb2 (alpha-tubulin) on three different dates and  $n = 89$  cells expressing GFP-Atb2 plus Cut11-meGFP on five different dates (Fig. 1a). As previously described [9, 10], cutting the spindle causes the fragments to rapidly collapse towards each other (Fig. 1b). We quantified the dynamics of collapse by tracking the

ends of the spindle fragments after ablation and calculated the change in distance between the ends over time. An example of the change in pole-to-pole distance over time is shown in Fig. 1c where a sharp decrease in distance between the poles is evident.

While previous work [9, 10] hypothesized this behavior as passive relaxation of the nuclear envelope or other materials inside of the nucleus (such as chromosomal DNA), its driving force is not yet clear. To test whether nuclear envelope relaxation drives the collapse of the spindle after ablation, we ablated cells expressing GFP-Atb2 and Cut11-mGFP (which localizes to the nuclear envelope) to observe their simultaneous response (Fig. 1d). As shown by arrows in Fig. 1d, during the collapse, the spindle fragments pull the nuclear envelope inward with them, creating local dents at the boundary between the nuclear membrane and the cytoplasm. Such changes in the membrane morphology are inconsistent with the collapse of the spindle driven by the relaxation of tension in the nuclear membrane. This result suggests that active pulling forces internal to the spindle, such as molecular motor proteins, may be at play here (Fig. 1d), and that the surface tension of the nuclear envelope does not cause the collapse.

Work here demonstrates the power of laser ablation as a tool for investigating the mechanics of cytoskeletal machinery. While previous work suggested the presence of compressive forces from outside the spindle, the current work instead suggests that collapse requires pulling from inside the spindle. However, this does not exclude the possibility of additional viscoelastic contributions from the nuclear envelope or chromosomal DNA. Furthermore, the current work raises new questions regarding the origin of the spindle's force balance. To fully explain the spindle's mechanical equilibrium, it will be important to determine the dependence of collapse on spindle-based forces, and the molecular requirements for this force generation.

## ACKNOWLEDGMENTS

We thank Caroline Laplante and Fred Chang for providing strains and Kimberly Bellingham-Johnstun, along with the Elting lab members, for helpful discussions. PZ acknowledges the funding support by the Provost's Professional Experience Program, the Office of Undergraduate Research at North Carolina State University, and the National Society of Physics Students. MWE acknowledges support by NIH 1R35GM138083 and NSF 1935260.

## REFERENCES

1. J. M. Mitchison, "Chapter 7 physiological and cytological methods for *schizosaccharomyces pombe*," in *Methods in Cell Biology*, Vol. 4, edited by D. M. Prescott (Academic Press, 1970) pp. 131–165.
2. I. M. Hagan and J. S. Hyams, *J. Cell Sci.* **89** ( Pt 3), 343–357 (1988).
3. K. Nabeshima, T. Nakagawa, A. F. Straight, A. Murray, Y. Chikashige, Y. M. Yamashita, Y. Hiraoka, and M. Yanagida, *Molecular Biology of the Cell* **9**, 3211–3225 (1998).
4. R. Ding, K. L. McDonald, and J. R. McIntosh, *Journal of Cell Biology* **120**, 141–151 (1993).
5. K. Tanaka and T. Kanbe, *Cell Sci.* **80**, 253–268 (1986).
6. H. Masuda, T. Hirano, M. Yanagida, and W. Z. Cande, *The Journal of Cell Biology* **110**, 417–425 (1990).
7. A. Mallavarapu, K. Sawin, and T. Mitchison, *Current Biology* **9**, 1423–1428 (1999).
8. A. Khodjakov, R. W. Cole, and C. L. Rieder, *Cell Motility and the Cytoskeleton* **38**(4), 311–317 (1997).
9. A. Khodjakov, S. La Terra, and F. Chang, *Current Biology* **14**, 1330–1340 (2004).
10. I. M. Tolić-Nørrelykke, L. Sacconi, G. Thon, and F. S. Pavone, *Current Biology* **14**, 1181–1186 (2004).
11. S. L. Forsburg and N. Rhind, *Yeast (Chichester, England)* **23**, 173–183 (2006).
12. J.-Q. Wu, J. R. Kuhn, D. R. Kovar, and T. D. Pollard, *Developmental Cell* **5**, 723–734 (2003).
13. M. W. Elting, M. Prakash, D. B. Udy, and S. Dumont, *Current Biology* **27**, 2112–2122.e5 (2017).
14. M. A. Begley, A. L. Solon, E. M. Davis, M. G. Sherrill, R. Ohi, and M. W. Elting, preprint bioRxiv , 2020.05.19.104661 (2020).
15. M. W. Elting, C. L. Hueschen, D. B. Udy, and S. Dumont, *Journal of Cell Biology* **206**, 245–256 (2014).
16. S. Santaguida and A. Amon, *Nature Reviews. Molecular Cell Biology* **16**, 473–485 (2015).
17. V. P. Singh and J. L. Gerton, *Current Opinion in Cell Biology Differentiation and Disease* **37**, 9–17 (2015).

# Preliminary Examination of Uncertainties due to Parton Distribution Functions in Far-Forward Neutrino Production at the Large Hadron Collider

Fnu Karan Kumar<sup>a)</sup>

Physics Department, Stony Brook University, Stony Brook, New York, 11794, USA

<sup>a)</sup>Corresponding author: [fnu.karankumar@stonybrook.edu](mailto:fnu.karankumar@stonybrook.edu)

**Abstract.** A large flux of neutrinos is expected in the forward direction of the pp collisions [1, 3] at the Large Hadron Collider (LHC) at CERN. Several experiments have recently been proposed at CERN to detect these neutrinos and discussion has started on the possibility of building a Forward Physics Facility grouping many of them. Among the others, the FASER-nu [2] proposal consists of a lead+emulsion neutrino detector at a distance of 480 m from the ATLAS interaction region along the tangent to the LHC beamline. Old calculations of neutrinos rates in the forward direction were done to leading order in the QCD perturbative series. We have included next-to-leading order (NLO) terms in our calculation. We have also studied the effect of incorporating a non-perturbative Gaussian intrinsic  $k_T$ . This  $k_T$  effect mimics the contribution from missing higher-order terms in QCD calculations. We present the study of uncertainties due to scale variations and Parton Distribution Function (PDF) variations in the production rate of  $D_s^\pm$  and tau neutrinos in the far-forward Production at the Large Hadron Collider. We compare our predictions with the LHCb data with  $D_s^\pm$  production in the rapidity range of  $[2 - 4.5]$  at the LHC. In our studies, for which we consider various modern PDF sets, we also include the comparison of predictions obtained by different dynamical central scale assumptions.

## INTRODUCTION

Neutrinos are one of the fundamental particles that make up the universe. They are one of the most abundant particle in the universe and are also the least understood. The neutrino is a subatomic particle that resembles an electron but is electrically neutral and has a very small mass compared to other elementary particles. Neutrinos belong to the lepton family in the standard model. Lepton is a family of particles that doesn't experience strong interactions. Out of the four fundamental forces, neutrinos interact only through the weak force and gravity. As the weak nuclear force is very short-range and gravitational interaction of the neutrino is extremely weak, they rarely interact with normal matter. There are trillions of neutrinos passing through us every second.

Neutrinos come in three flavors: electron, muon, and tau neutrinos. They are labeled after their charged partners within the Standard Model. In charged current neutrino interactions in matter, neutrinos of a given type result in the emission of their charged partner. Out of the three flavors, tau neutrinos are the least studied as there is not sufficient data available to study them. The collision of proton beams at 14 TeV at the Large Hadron Collider (LHC) produces a large flux of hadrons. The hadrons produced in the proton/proton collisions decay further into neutrinos. In particular, the decays of  $D_s^\pm$  and B mesons produce a large flux of tau neutrinos in the forward direction of the collision; however, there have been no experiments to observe these neutrinos. A new set of experiments have been proposed at CERN [2]. This paper is about the calculation of the flux of neutrinos in the forward direction at the LHC, along with the flux we study the uncertainties in our predictions caused by seven scale variations and Parton Distributions Functions.

The forward region can be understood with the kinematic variable called pseudo-rapidity. Pseudo-rapidity ( $\eta$ ) is a geometric quantity and is a function of the angle  $\theta$  with respect to the collision axis as seen in Fig.1. In this project, we are exploring the region with  $\eta > 6.87$  which approximately covers the forward detector coverage for the proposed experiments at CERN.

$$\eta = -\ln\left(\tan\left(\frac{\theta}{2}\right)\right) \quad (1)$$

There are two problems that arise in the Quantum Chromodynamics (QCD) perturbation theory that is used to calculate meson production in pp collisions: ultra-violet (UV) and infrared (IR) divergences. To include the higher-order term in perturbation theory, we come across Feynman graphs with closed loops, that are associated with unbounded energy. Because of unconstrained energy, the integral associated with such Feynman diagrams tend to diverge. Such divergences are called UV divergences. These divergences are not physical. The UV divergence are cured by introducing the renormalization factor ( $\mu_R$ ). We also encounter Feynman diagrams which include massless particles of energy

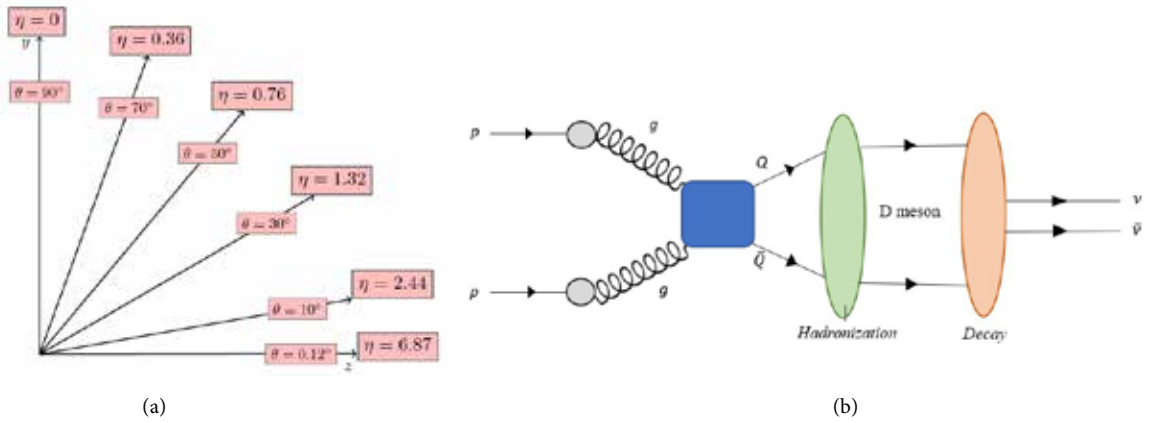


**FIGURE 1:** (a) The relation between  $\eta$  and  $\theta$ : An angle of zero is along the beam axis. Generally, particles in the high pseudorapidity regime escape through space in the detector along with the beam axis (forward direction), and this project includes the study of tau neutrino in the forward direction. (b) Proton-proton collision: Gluons from colliding proton interact during the collision. Gluon-Gluon interaction produce a quark and anti-quark which further produces hadrons like  $D_s^\pm$  meson.  $D_s^\pm$  meson decay into tau neutrinos.

approaching zero. The integral of Feynman diagrams including massless particles with zero energy also diverge. The divergence due to massless particles is known as Infrared(IR) divergences. The problem of IR divergence is solved by introducing the factorization factor ( $\mu_F$ ). The renormalization and factorization scales ( $\mu_R, \mu_F$ ) are defined to be the factors ( $N_R, N_F$ ) multiplied by the transverse mass  $m_T$ . We will use two different definitions for the transverse mass:

$$m_T = \sqrt{m_c^2 + p_T^2} \quad \text{and} \quad m_T = \sqrt{4m_c^2 + p_T^2},$$

where  $p_T$  is the magnitude of the transverse momentum of the charm quark and  $m_c$  is the charm quark mass.

The other variable in our calculation is the Parton Distribution Function (PDF). Parton, name given by Richard Feynman, refers to particle (quarks and gluons) constituents within the protons, neutrons and other hadrons. In the proton/proton collision, what actually happen is that these partons collide with each other as seen in Fig.1a. The colliding parton carries a fraction of the momentum of the proton. Parton distributions functions are momentum distribution functions of the partons within the proton. They are probability densities to find a parton with momentum with fraction  $x$  at an energy scale of  $\mu^2$ . We can calculate the hadronic cross section using these PDF.

## THEORY

The most important concept in collisions of subatomic particles is their cross section. The word cross section is first introduced in mathematics as a intersection between a plane and a three dimensional object. In physics, the word cross section also has units of area, but comes from a different consideration. The cross section with units of area governs the probability that two particles will collide or interact to produce a certain outcome and is denoted by  $\sigma$ . For example, the total cross section for production of tau neutrinos could be written as:

$$\sigma = \frac{\text{\# of tau neutrinos produced per unit time}}{\text{Luminosity of protons per unit area per unit time}} \quad (2)$$

The other important term is Luminosity. In the above formula, it can be seen that Luminosity is the ratio of the number of events detected (N) in a certain time (t) to the cross-section. Using cross section and luminosity, we can



calculate the number of events ( $dN/dt$  events/sec) by the following:

$$dN/dt = L \times \sigma . \quad (3)$$

As mentioned earlier, we include NLO QCD corrections to the heavy-quark (HQ) production cross section. The HQ production cross section under perturbative QCD is as follow [4]:

$$E \frac{d^3\sigma}{dp^3} = \sum_{i,j} \int dx_1 dx_2 f_i^{H_1}(x_1, \mu_F^2) f_j^{H_2}(x_2, \mu_F^2) \left[ E \frac{d^3\hat{\sigma}_{ij}(x_1 P_{H_1}, x_2 P_{H_2}, p, m^2, \mu_F^2, \mu_R^2)}{dp^3} \right]$$

(4) where  $f_i^{H_1}(x_1, \mu_F^2)$  and  $f_j^{H_2}(x_2, \mu_F^2)$  are parton distribution functions (PDFs),  $\mu_F^2$  and  $\mu_R^2$  are factorization and renormalization scales, respectively. As we discussed before, we need to account for mean transverse momentum in our calculation. We use a Gaussian approximation for transverse momentum in 2 dimensions.

$$f(\vec{k}_T) = \frac{1}{\pi \langle k_T^2 \rangle} e^{-\frac{k_T^2}{\langle k_T^2 \rangle}} \quad (5)$$

After including the  $k_T$  effect and integrating over it, the heavy quark production cross section becomes:

$$E \frac{d^2\sigma}{dp_z d^2p_T} = \int d^2k_T \int d^2p'_T f(\vec{k}_T) E \frac{d^2\sigma}{dp_z d^2p'_T} \delta^2(\vec{p}_T - \vec{p}'_T - \vec{k}_T) \quad (6)$$

The theoretical evaluation of the production of heavy quarks like charm has been studied for quite a long time, and is already implemented in a computer program called HVQ [5, 6] using the FORTRAN language. We used this program with some modifications to run simulations in our study. The HVQ code uses the Vegas algorithm [7] to calculate the integrals for the heavy quark production cross section. As there is no data available in the forward direction for production of particles, we use LHCb data for the production of  $D_s^\pm$  to compare with our theoretical predictions. We provide predictions by varying three parameters:  $k_T$ ,  $\mu_F^2$  and  $\mu_R^2$ . By varying these parameters, we tried to fit the data with our predictions using different transverse masses as discussed above. From the previous studies, we found that  $k_T = 0.7$  GeV fit well with the data [8, 9].

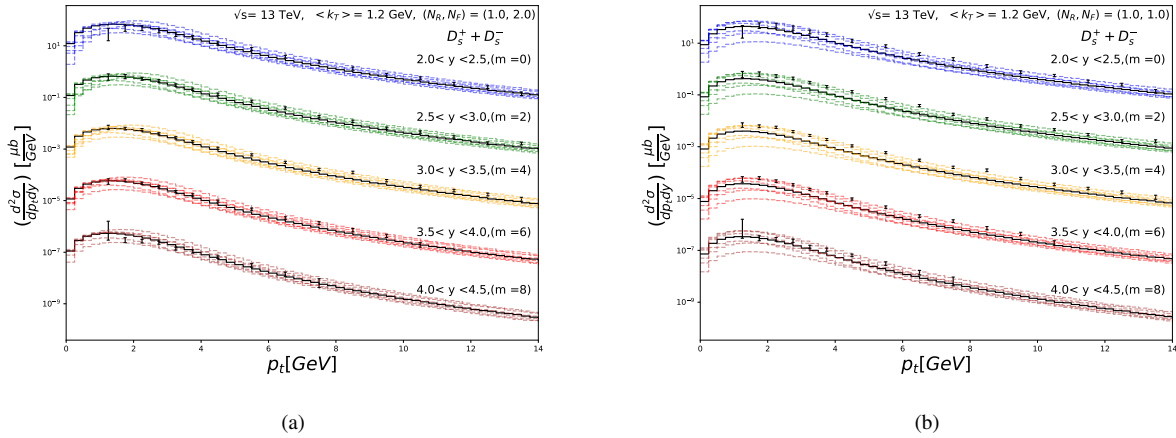


**FIGURE 2:** Comparison between our predictions and LHCb experimental data on double-differential cross section for  $D_s^\pm$  production. Data and predictions for different  $y$  bins are shifted by  $10^{-m}$  where values of  $m = 0, 2, 4, 6$  and  $8$ . Fig. (a) refers to the central scale  $N_R = 1.0$ ,  $N_F = 2.0$  with  $m_T = \sqrt{m_c^2 + p_T^2}$  with  $\langle k_T \rangle = 1.2$ . Fig. (b) shows to the central scale  $N_R = 1.0$ ,  $N_F = 1.0$  with  $m_T = \sqrt{4m_c^2 + p_T^2}$  with  $\langle k_T \rangle = 1.2$ . The colored portion shows the uncertainty band of seven scale variations.

The scale variations  $(N_R, N_F)$  in  $(\mu_R, \mu_F) = (N_R, N_F)m_T$ , where  $m_T = \sqrt{m_c^2 + p_T^2}$  are  $[(1,2), (0.5, 1), (2,4), (0.5,2), (1,1), (2,2), (1,4)]$  with  $(1,2)$  as central scale choice. The scales variations  $(N_R, N_F)$  in  $(\mu_R, \mu_F) = (N_R, N_F)m_T$ , where  $m_T = \sqrt{4m_c^2 + p_T^2}$  are  $[(1,1), (0.5,0.5), (2,2), (0.5,1), (1,0.5), (2,1), (1,2)]$  with  $(1,1)$  as central scale choice. By examining the scale variations, we find the best central scale assumptions of transverse mass with  $k_T$ . In our studies, we are using PROSA [10] PDF. The PDF are created using data from Deep Inelastic Scattering (DIS) of leptons and fit with different models and parameters. PROSA contains 40 variations that account for PDF fit uncertainty, PDF parameter uncertainty, PDF model uncertainty. The fit uncertainties come from the data that is used to create the PDF, parameter uncertainties arise from the parameter used to fit the data, and model uncertainties originate from the assumed model for the fit for the PDF. The total uncertainties are obtained by adding fit, model, and parameter uncertainties in quadrature.

## RESULTS

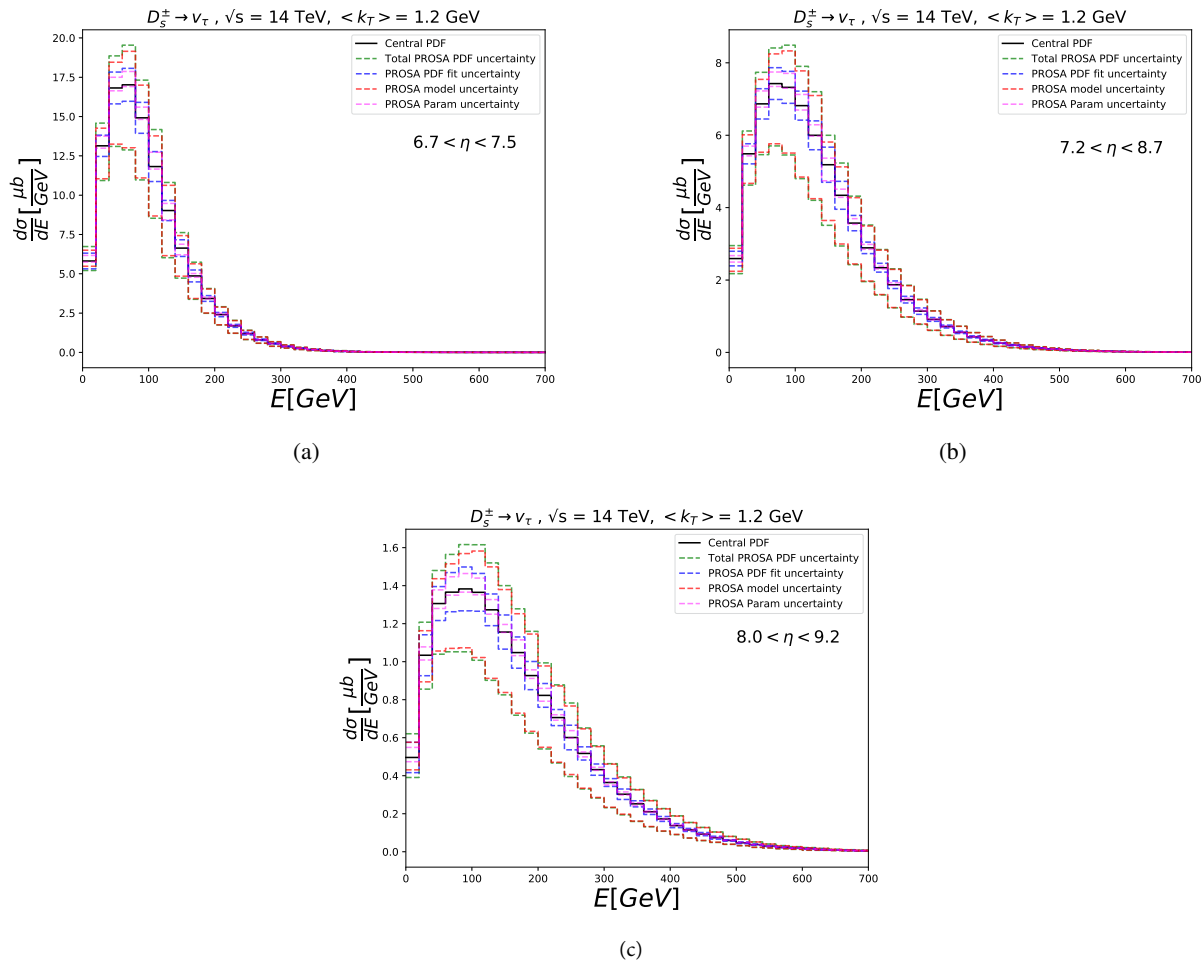


**FIGURE 3.** These figures show the uncertainties in the calculation of cross section of tau neutrinos in the rapidity range from  $6.7 < \eta < 7.5$ ,  $7.2 < \eta < 8.7$ , and  $8.0 < \eta < 9.2$ . The selected rapidity ranges represent the forward region of the pp collision.

In Fig. 2, we compare our prediction of  $D_s^\pm$  double differential cross section with the LHCb data. By comparing

figures 2a and 2b, we conclude that transverse momentum  $m_T = \sqrt{m_c^2 + p_T^2}$  with  $k_T = 1.2$  GeV produces better prediction. We select the parameter,  $\langle k_T \rangle = 1.2$  GeV, and  $m_T = \sqrt{m_c^2 + p_T^2}$  with central scale of  $(N_R, N_F) = (1.0, 2.0)$ , to further study the uncertainties in PDFs for tau neutrino production in the forward region. Fig. 3 shows the uncertainties as bands around the central PDF assumption due to variations in PDFs in the cross section of tau neutrinos in the forward region of the pp collision. The majority of the uncertainties are due to model assumptions made in creating the PDF. These model assumptions vary from different collaborations who have produced these PDFs. The root of the problem arises from the lack of knowledge of the structure of the nucleon. To get better estimates of the production rate in the forward direction, we need better understanding of model assumptions for PDFs.

## CONCLUSION

Neutrinos are mysterious and everywhere around us. Understanding neutrinos is a challenging task as they rarely interact with matter. FASER-nu [2] experiment has been proposed to measure the flux of neutrinos in the forward direction at the LHC. This paper focused on flux uncertainties using seven scale variations and PDF uncertainties in the production of  $D_s^\pm$  and tau neutrinos from decays of these mesons. According to our results, the calculation of  $D_s^\pm$  double differential cross section with transverse momentum  $m_T = \sqrt{m_c^2 + p_T^2}$  is the best fit for the LHCb data. The tau neutrino flux uncertainties with  $m_T = \sqrt{m_c^2 + p_T^2}$  are comparably less than uncertainties with  $m_T = \sqrt{4m_c^2 + p_T^2}$ . The analysis of PDF uncertainties is still under way. According to our initial studies, the dominant part of the uncertainty is due to the PDF model itself. The studies will continue to examine the various elements of uncertainties due to the PDFs and find ways to reduce those uncertainties in our calculation.

## ACKNOWLEDGMENTS

I would like to thank my mentor Dr. Milind Diwan at Brookhaven National Lab for his support and knowledge on this project. I would also like to thank Prof. Mary Hall Reno (University of Iowa), Prof. Maria Vittoria Garzelli (Hamburg University), Dr. Weidong Bai (University of Iowa), and Dr. Yu Seon Jeong (CERN) for their time and valuable suggestions on this project. This project was supported in part by the U.S. Department of Energy.

## REFERENCES

1. A. De Rujula and R. Ruckl, "Neutrino and muon physics in the collider mode of future accelerators" in *Proceedings of the ECFA-CERN Workshop : Large Hadron Collider in the LEP tunnel* (Lausanne, 1984) pp.571-596.
2. FASER collaboration, A. Ariga et al., Technical Proposal for FASER: ForwArd Search ExpeRiment at the LHC, 1812.09139.
3. K. Winter, "Detection of the tau-neutrino at the LHC" in *ECFA Large Hadron Collider Workshop Proceedings.2.*, (Aachen, 1990) pp. 37-49.
4. P. Nason, S. Dawson and R. K. Ellis, Nucl. Phys. B **303**, 607-633 (1988) .
5. M. L. Mangano, P. Nason and G. Ridolfi, Nucl. Phys. B **373**, 295-345 (1992).
6. P. Nason, S. Dawson and R. K. Ellis, Nucl. Phys. B **327**, 49-92 (1989) [erratum: Nucl. Phys. B **335**, 260-260 (1990)]
7. G. P. Lepage, J. Comput. Phys. **27**, 192 (1978).
8. W. Bai and M. H. Reno, J. High Energ. Phys., **2019**, 77 (2019).
9. W. Bai, M. Diwan, M. V. Garzelli, Y. S. Jeong and M. H. Reno, J. High Energ. Phys. **2020**, 032 (2020)
10. PROSA collaboration, O. Zenaiev, M. Garzelli, K. Lipka, S. Moch, A. Cooper-Sarkar, F. Olness et al., J. High Energ. Phys. **2020**, 118, (2020).

# Installation of a Cosmic-Ray Trigger System to Commission the Belle II Experiment VerteX Detector with Cosmic Rays

Ahmed Halawani,<sup>1, a)</sup> Rachid Ayad,<sup>2, b)</sup> Mohammed Albalawi,<sup>2</sup> Mansour Alatawi,<sup>2</sup> Abdulaziz Alatawi,<sup>2</sup> and Hans-Günter Moser<sup>3</sup>

<sup>1</sup> King Abdulaziz University, Al Jami'ah, 21589, Jeddah, Saudi Arabia

<sup>2</sup> University of Tabuk, King Faisal Street , 47512 Tabuk , Saudi Arabia

<sup>3</sup> Max Planck Institute for Physics, Fohringer Ring 6, 80805 Munich, Germany

<sup>a)</sup>Corresponding author: ahalawani0050@stu.kau.edu.sa

<sup>b)</sup>Electronic mail: rayad@ut.edu.sa

**Abstract.** In this paper, we describe the design, construction, testing, and installation of the cosmic ray trigger system used to commission the VerteX Detector (VXD) of the Belle II experiment at the High-Energy Accelerator Research Organization (KEK) in Japan. The system consists of two rows of scintillators; with six scintillators being on top of the VXD, and six at the bottom of it. The scintillators were characterized (plateaus, threshold values, coincidences rate), and when compared with the simulation values a concordant match was found for all cosmic coincidence measurements. In Phase 3 of SuperKEKB accelerator, the VXD was the last sub-detector to be integrated into the heart of Belle II detector, after it was absent from being integrated within Belle II in Phase 1 and Phase 2 of SuperKEKB machine studies. A system consisting of VXD prototype parts had been installed, into Belle II detectors, at the VXD location during Phase 2 to study background and it was found that the VXD can cope with the level of measured background: allowing the VXD to be present during Phase 3 Belle II data taking. The VXD was tested with cosmic rays outside of Belle II before it was integrated within Belle II just before Phase 3 data taking, which commenced in March 2019.

## INTRODUCTION

The B-Factories accelerators PEP-II at KEKB at the KEK (Translated from Japanese to be “The High Energy Accelerator Research Organization”) center, Japan, and the Stanford Linear Accelerator Center (SLAC), USA, have been extremely successful during the period 1999-2010. Belle experiment took data at KEKB and BaBar experiment took data at PEP II. Both Belle and Babar contributed to the establishment of the theory of Makoto Kobayashi and Toshihide Maskawa[1] who quantitatively explained the observed CP violation in the K-meson and B-meson systems. Both M. Kobayashi and T. Maskawa, along with Yoichiro Nambu, were awarded the 2008 Nobel Prize in Physics, where Belle and BaBar experiments were cited, in the 2008 Nobel Prize of physics press release, as main contributors to this Nobel Prize. We will discuss here the construction and installation of a cosmic ray trigger system, at KEK center in Japan, to commission the Belle II experiment VerteX Detector (VXD) with cosmic rays before it was integrated within the Belle II

detector. In section 2 we will discuss the apparatus and its components; afterwards we will report in section III the results of the cosmic trigger system tests done at the bench. Then, in section 4, we will report on the assembly and studies of the system at KEK center in Japan; finally, data quality will be discussed and examined in section 5.

## APPARATUS

Cosmic rays were used to commission VXD for SuperKEKB phase 3 data taking. Historically, cosmic rays had been used in the 1940s and 1950s as a source to search for new particles in fixed target experiments. Later on, in the beginning of 1960s, colliders had been built to reach higher energy collisions and cosmic rays have been used ever since to test and commission new particle trackers (detectors). Our cosmic ray trigger system is composed of four main parts; the frame, scintillators (including light-guides), photomultipliers, and a rack housing a NIM and VME crates with many data acquisition modules. We will elaborate on each of those components in this section.

### The Frame

The VXD cosmic trigger system was designed to house six top scintillators and six bottom scintillators, each scintillator has dimensions of:  $10\text{cm} \times 30\text{cm} \times 1\text{cm}$ , as shown in Fig. 1. The cosmic trigger system had been tested at the bench during spring 2018 and results are shown in section 4. Then the cosmic trigger system was shipped to KEK to be installed in the VXD commissioning clean room near Belle II IP. The cosmic trigger system frame is designed to be fixed on the granite threaded table, where VXD sits, with scintillators surrounding VXD as shown in Fig. 2.



**FIGURE 1.** A schematic of the VXD cosmic trigger system with six top and six bottom scintillators.

### Connections & Data Acquisition

We worked on making the cosmic trigger Data AcQuisition DAQ system automatic enough to control it from a host at least at the run control system. However the PMs thresholds, on the CAEN NIM discriminator modules, were the only ones not accessible from the host and were adjustable by hand. The cosmic VXD raw data are stored within the Belle II DAQ system, however we wrote a standalone DAQ in which we monitor and store cosmic scintillators coincidence rates by reading a CAEN VME V830 scaler module.

An overview of the VXD cosmic trigger system DAQ is shown in Fig. 3. The DAQ system is written in C/C++ code within a PC under a Linux/ubuntu platform. The CAEN HV SY403 module is connected to the DAQ machine, via a RS232-to-USB cable, to automatically ramp- up/ramp-down PMs HVs and monitor them together with the currents. PMs signals are first discriminated by CAEN NIM discriminator modules (N841), then the discriminated NIM signals are sent to coincidence NIM modules to generate a global trigger signal to be sent to Belle II DAQ for cosmic data taking.

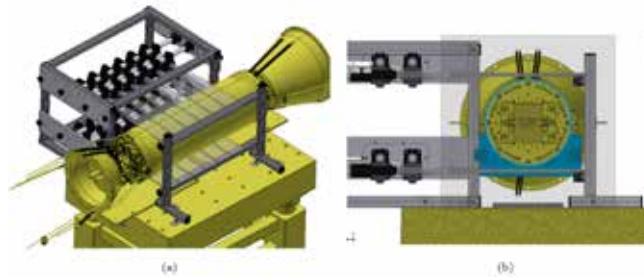


**FIGURE 2.** Front view (a) and a side view (b) of the cosmic trigger system frame, with its 12 scintillators. The pictures also show the way at which the VXD is fixed on the commissioning granite table at KEK.

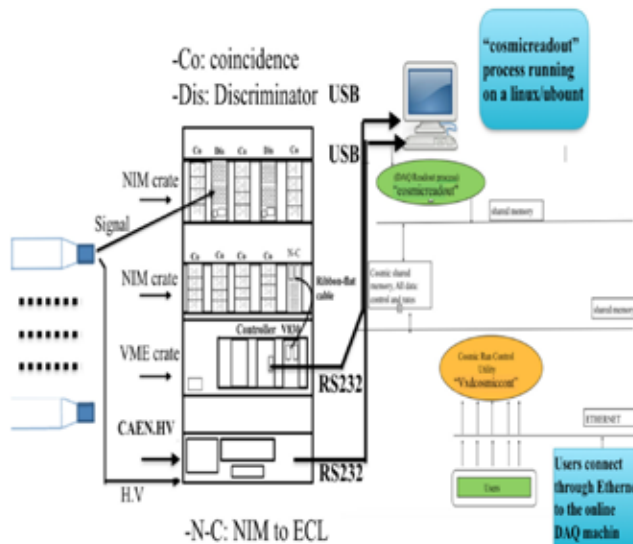


**FIGURE 3.** A schematic of the cosmic trigger Rack with all its NIM and VME crates with their electronic modules. At the right of the figures is the structure of the cosmic standalone DAQ.

## TESTS AT THE BENCH

The cosmic trigger looks like as in Fig. 4 when the scintillators are inserted with PMs. The scintillators had been tested before being mounted in the frame two by two on top of each other. Signals were studied and plateaus measured as shown in Fig. 5. The operating HV is taken at the beginning of the plateaus to be 1250 V for the first scintillator and 1400 V for the second scintillator. Finally we measured top and bottom scintillators coincidence rates. In particular we measured coincidence rates for one top scintillator with each of the six bottom scintillators with all scintillators installed in the frame.

## INSTALLATION AT KEK

Once the cosmic trigger system was tested at the bench, it was dismantled and its parts were shipped to KEK in June 2018. The scintillators were fixed on the cosmic-ray trigger frame, and then the frame was installed inside the VXD commissioning room as shown in Fig. 6. Coincidence rates versus incidence angle, of one top corner scintillator with each of the bottom scintillators are shown in Fig. 7 where the x-axis is the horizontal shift in cm of the bottom scintillators with respect to one of the top corner scintillators. We used a miss-and-hit program (written in C) to simulate cosmic rays coincidence rates between top and bottom. Fig. 7 shows that the coincidence rates, following a cosine-square behavior as known, match the simulation very well.



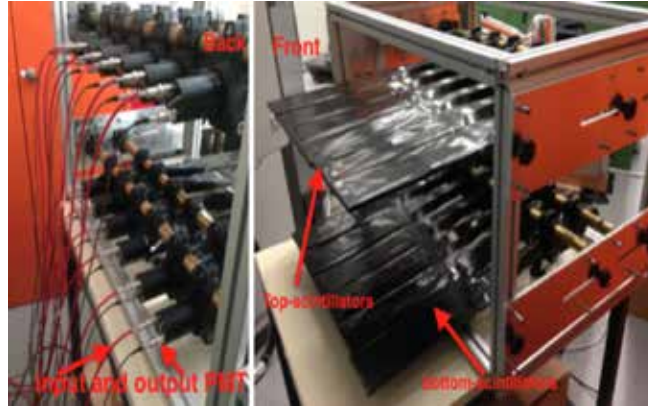


**FIGURE 4.** All scintillators, with PMTs, are Installed in the frame, and tested.

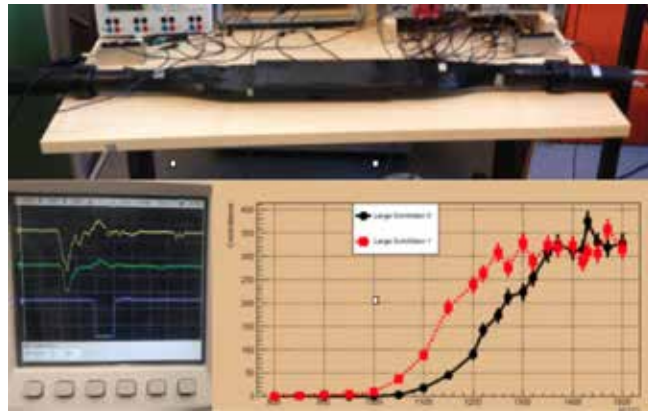


**FIGURE 5.** Plateaus of two scintillators tested on top of each other.

## COSMIC-RAY DATA QUALITY

At the beginning of November 2018, we started taking cosmic data with the VXD in the commissioning clean room at KEK, for about 12 days. The global trigger is defined as: **OR** for all the six top scintillators, connected with **AND** of **OR** of all the six bottom scintillators. The cosmic global trigger coincidence rate had been measured during data taking using a system NIM discriminator and Coincidence CAEN modules and a CAEN VME scaler module (V830). We took several runs to measure this global coincidence rate, and all runs give stable distribution rates like in Fig. 8. The cosmic rate distribution, in Fig. 8, looks like a Poisson Distribution with a mean value of  $(10.05 \pm 3.12 \text{ Hz})$  matching the simulation result of 10.45 Hz.

We also used the Belle II Analysis Software Framework (basf2) simulation and reconstruction program to display cosmic-ray tracks in VXD. An example of such display is shown in Fig. 9 [2, 3, 4]. The cosmic-ray track is shown in r-z view (front view) and r- $\varphi$  views (side view).

About 300,000 tracks were reconstructed. A full analysis of these events to align VXD will be discussed in a future paper, as this paper discusses only the construction and installation of the Belle II VXD detector cosmic-ray trigger system.

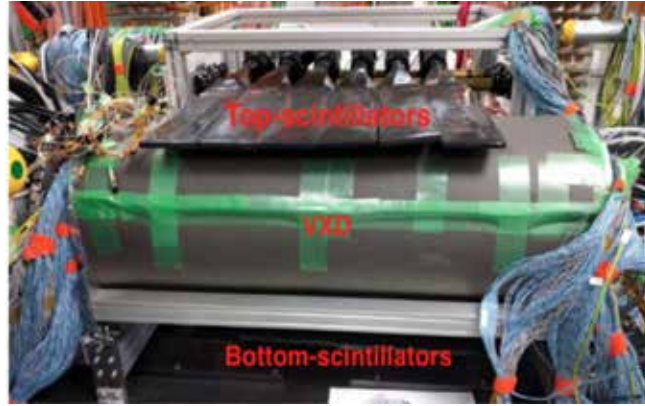


**FIGURE 6.** A view of the cosmic trigger system surrounding VXD, where the top scintillators are seen. The VXD is the sealed tube in the middle.

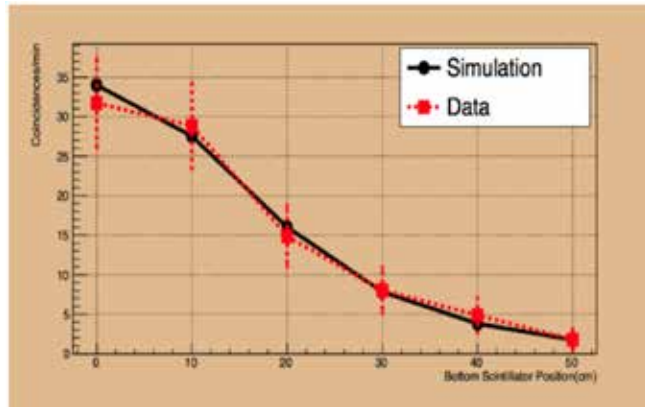


**FIGURE 7.** Coincidence rates of a top corner scintillator with each of the six bottom scintillators. The rates are found matching the simulation.

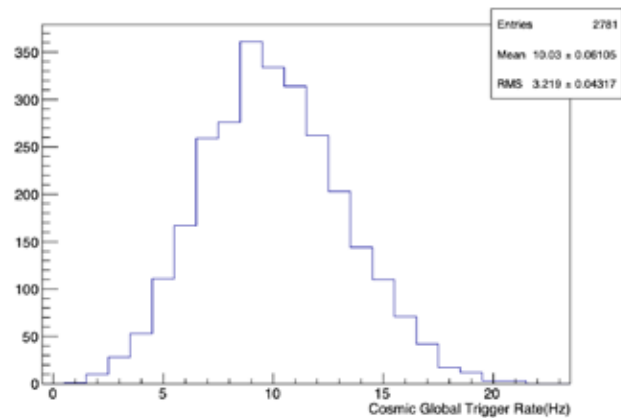


**FIGURE 8.** Global cosmic trigger rate had been continually measured by a VME scaler module from CAEN. The global coincidence trigger rate, of six top and six bottom scintillators, found to be  $(10.05 \pm 3.124)$  Hz matching the simulation value that is of 10.45 Hz. The distance between top and bottom scintillators is 19.2 cm.

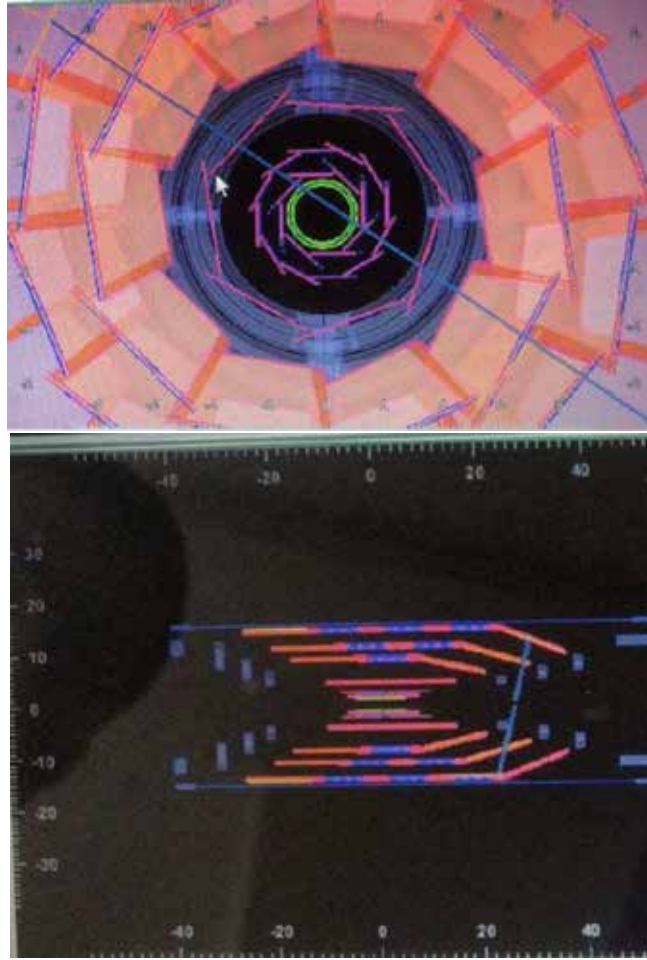


**FIGURE 9.** A display of a cosmic ray, triggered by our system, in  $r$ - $z$  and  $r$ - $\phi$  views.

## CONCLUSION

We designed, constructed, tested, and installed the Belle II cosmic trigger system to commission Belle II VXD detector at KEK center during fall 2018. The VXD had been assembled in a clean room at KEK before it was installed within Belle II detector at the beginning of 2019. We took cosmic-ray data on the VXD, while it was outside Belle II detector, showing events display with well reconstructed cosmic tracks which seem to match simulation results. Immense effort had been done to align Belle II VXD detector with cosmic rays so as to be commissioned before being integrated within Belle II detector. The results will be published soon, though they were already presented in conferences [5].

We are preparing ourselves to use this cosmic trigger system to commission the Belle II VXD with its full parts during 2021 SuperKEKB shutdown.

## ACKNOWLEDGMENTS

We would like to thank the University of Tabuk, KSA, for their unwavering support in the research, and for providing grants: S-1438-0256 and S-1439-0280, which were put into purchasing parts of the trigger system, as well as for covering traveling expenses. We would also like to extend our gratitude to King Abdulaziz University, KSA, for contributing by supplying researchers and some travel tickets. We would like to also thank KEK center and the Max Planck Institute of physics (MPI) for providing some of the cosmic

trigger hardware parts.

## REFERENCES

1. M. Kobayashi and T. Maskawa, *Prog. Theor. Phys.* **49**, 652–657 (1973).
2. T. Bilka et al, *EPJ Web Conf.* **245**, 02023 (2020).
3. J. Kandra et al., preprint, arXiv:1910.06289 [physics.ins-det] (2019).
4. B. Spruck et al., *PoS Vertex2019*, 015 (2020).
5. A. Halawani, R. Ayad, and M. Albalwi, “Commissioning the Belle II Vertex Detector (VXD), at KEK Center, Japan, with Comic Rays” in *Bulletin of the American Physical Society*, APS April Meeting (2019).

# PREPARING A MANUSCRIPT FOR PUBLICATION

B. Conrad,<sup>1, a)</sup> R. Adelberger,<sup>2</sup> and W. Slaton<sup>3, b)</sup>

<sup>1</sup>*Society of Physics Students, American Institute of Physics (AIP), College Park, MD 20782 USA*

<sup>2</sup>*Department of Physics, Guilford College, Greenboro, NC 27410 USA*

<sup>3</sup>*Department of Physics and Astronomy, University of Central Arkansas, Conway, AR 72035 USA*

<sup>a)</sup> *Corresponding author: [bconrad@aip.org](mailto:bconrad@aip.org)*

<sup>b)</sup> *[wvslaton@uca.edu](mailto:wvslaton@uca.edu)*

**Abstract.** Scientific manuscripts are documents that focus on providing a scientific argument to a specific group. In fact, audience selection is potentially the most important decision a science communicator needs to make before preparing a manuscript for publication. This document will outline a process to draft a manuscript for the Journal of Undergraduate Reports in Physics (JURP), but can also be used for most publications. In this specific case, junior or senior physics majors and undergraduate professors are your primary audiences. They are knowledgeable about physics, but unlike you, they have not spent much time trying to understand the specific problem being discussed in your report.

## OVERVIEW

Scientific manuscripts are documents that focus on providing a scientific argument to a specific group. In fact, audience selection is potentially the most important decision a science communicator needs to make before preparing a manuscript for publication. This document will outline a process to draft a manuscript for the Journal of Undergraduate Reports in Physics (JURP), but can also be used for most publications. In this specific case, junior or senior physics majors and undergraduate professors are your primary audiences. They are knowledgeable about physics, but unlike you, they have not spent much time trying to understand the specific problem being discussed in your report.

There is a big difference between the comments you write in the margin of your lab notebook and what you might write in a paper for publication in a scientific journal. Your laboratory data book is a chronological, definitive record of everything that you did. It contains all the data, what you did even if it was ultimately wrong, as well as comments as to what you were thinking at that time. A journal article is a focused summary discussion of the research question, its processes, and conclusions. Authors should avoid discussing experimental dead ends and present a clear scientific argument. The reader does not have to be able to completely reproduce the work from the Journal article. Instead, the reader should be able to understand both the physics and techniques of what was done and the rationale behind why it was done.

The goal of a journal article is to announce a new finding, idea, or process. Abstracts should provide the key result as most readers will only look at titles and abstracts. By using key words and clear abstracts, potential readers locate research of interest. If, after reading an article, a reader then wants to find out the finer details of an experiment or derivation, they can contact the author of the paper for a personal in-depth conversation about the subtleties.

The general style of writing used in a physics Journal is different from that of literary works. The narrative of the paper is intended to do three things: 1) present the background necessary for the reader to understand the science being reported in the paper; 2) outline the details and the implications of your work; 3) lead the reader through the work in such a way that they can clearly follow the rationale leading to your conclusions. When finished with your paper, the reader should not have to decide for themselves what you are proposing. The narrative should lead readers through your work in an unambiguous manner, telling them what to see and understand in what you did. Assist the reader with

interpretation of the data and calculations. Presenting a clear interpretation of your results is the most important part of the paper.

You should take care to make sure that the material is presented in a concise and logical way. Make sure that your sentences do not have too many dependent clauses. Overly complicated or long sentences make the logic of an argument difficult to follow. You should choose a paragraph structure that focuses the attention of the reader on the development of the ideas. Paragraphs should connect to each other, as the manuscript is a focused logical argument.

## SECTIONS

### Abstract

An abstract is a self-contained paragraph that concisely explains what you did and presents key results. The abstract is often published separately from the body of the paper, so you cannot assume that the reader of the abstract also has a copy of the rest of the paper. You cannot refer to figures or data that are presented in the body of the paper. Since abstracts are used in literature searches, all key words that describe the paper should be included in the abstract. Be quantitative with results and keep it to less than 100 words.

### Introduction

This section outlines the background necessary to introduce your results. It is not an abbreviated review of what you are going to discuss in detail later. This section should present the necessary theoretical and experimental context such that a knowledgeable colleague, who is not an expert in the field, will be able to understand the data presentation and discussion. If you are going to use a particular theoretical model to extract some information from your data, this model should be discussed in the introduction.

Where appropriate, factual information should be referenced. When presenting background information, you may guide the reader to a detailed description of a particular item with the statement such as: "A more detailed discussion of laminar flow can be found elsewhere.<sup>1</sup>" If you know where there is a good discussion of some item, you should not repeat it.

How one proceeds from this point depends upon whether the paper is about a theoretical study or an experiment. We will first suggest a format for papers about experimental investigations and then one that describes a theoretical derivation.

## Experimental Investigations

### *The Experiment*

This section guides the reader through the techniques and apparatus used to generate the data. Schematic diagrams of equipment and circuits are often easier to understand than prose descriptions. A statement such as "A diagram of the circuit used to measure the stopping potential is shown in Fig. 6" is better than a long set of words. It is not necessary to describe in words what is shown in a diagram unless the average reader would not be able to follow. If special experimental techniques were developed as part of this work, they should be discussed here. You should separate the discussion of the equipment used to measure something from your results. This section should not include data presentations or discussions of error analysis.

### *Data Presentation and Interpretation of Results*

The data are the truths of your work. This section should lead the reader through the data and how errors were measured or assigned. The numerical data values should be presented in tables and figures, each with its own number and caption, e.g., "The results of the conductivity measurements are shown in Table 3." It is difficult to follow narratives when the numerical results are included as part of the narrative. Raw, unanalyzed data should not be presented in the paper. All figures and tables should be referred to by their number. Any figure or table that is not discussed in the narrative should be eliminated. Items which are not discussed have no place in a paper.



## Theoretical Studies

### *The Model*

This part should consist of a theoretical development of the constructs used to model the physical system under investigation. Equations should be on separate lines and numbered consecutively. The letters or symbols used in the equations should be identified in the narrative, e.g., “The potential can be approximated as:

$$W \approx Z - \sigma(\rho) \quad (1)$$

where  $Z$  is the number of protons and  $\sigma$  is the screening constant that is dependent on the charge density,  $\rho$ , of the inner electrons of the  $K$  and  $L$  shells”. If you wish to use this equation at a later time in the narrative, refer to it by its number, e.g., “The straight line fit shown in Fig. 3 indicates that Equation 1 can be used to extract a value of...”

### *Calculations*

This section presents a summary and discussion of the numerical results calculated from the model. The results should be presented in tables or graphs, each with a caption. A table or graph that is not discussed in the narrative should be eliminated. Data that are not interpreted by the writer have no place in a paper. Reference numerical results that are used in the calculations and come from previous work done by others.

## Conclusion

In this section, briefly summarize the key result and supporting argument. Be sure to list important quantities and, if appropriate, where this research could lead in the future.

## References

All references, numbered in order of appearance, are collected together at the end of the paper. Note that in most cases you do not need to include article titles. Additional formatting guidance for JURP submissions is available on the JURP website and AIP Publishing’s website. See the references for examples.<sup>1-6</sup>

## Other Advice

### *Tables and Figures*

In some journals, tables and figures are placed by the layout editors at the corners of the page to make the format attractive and easy to read. A figure may not be on the same page as the discussion of that figure. Readers often scan papers by looking at the figures and data tables before they read the narrative of the work. For these reasons, each table or figure should be numbered and have a descriptive caption. Take care to put enough information in the caption that the reader can get some feeling for the meaning of the data presentation. All lines shown on graphs should be identified, e.g., “The dashed line is drawn to guide the eye” or “The solid line is a fit to the data using the Ising model.”

An example of a graph of a set of data is shown in Figure 1. The graph is sized by the range of data points. The bottom left point does not have to be the origin (0, 0). Error bars must be shown with data points. A graph with all the data points clustered in one small corner and lots of white space does not help the reader get a feeling of the dependence of your data. Be careful that the figures you present are not too busy; too much information on a figure makes it difficult to pick out the important parts. Remember that figures often appear much smaller in print so make sure graph fonts are about the same size as in the narrative. Also, color plots could be more expensive to print than black and white and not convey the information any more clearly. Black filled vs empty symbols or solid vs dashed lines offer high contrast on a plot that will be reduced in size for publication. Figures should have high resolution or they may appear blurry.

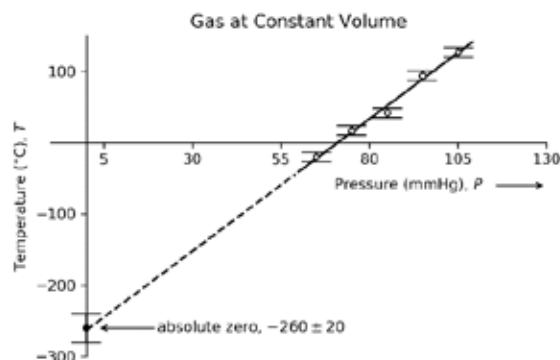


**FIGURE 1.** A graph of gas temperature versus pressure for an ideal gas at constant volume. The solid line drawn is the least squares fit straight line to the data. The dashed line extrapolates to the intercept, with uncertainty, denoting an estimate of absolute zero. This figure is adapted from John Taylor's "An Introduction to Error Analysis" 2nd Edition. The figure should be centered. To help stay within the space requirement consider having two figures next to each other. If figures have more than one part, each part should be labeled (a), (b), etc.

**TABLE 1.** Energy states found in the numerical search. The accepted values for these states are also listed.

State	Experimental $eV$	Theoretical $eV$
3S	$5.15 \pm 0.01$	5.13
4S	$1.89 \pm 0.02$	1.93
3P	$2.96 \pm 0.01$	3.02

## Numbers and Units

Any experimentally measured data presented in tables, such as that shown in Table 1, should include uncertainties. You should use scientific notation when presenting numbers,  $(7.34 \pm 0.03) \times 10^7$  eV. Take care that you have the correct number of significant digits in your results; just because the device shows six digits, does not mean that they are significant. You should use the MKS system of units.

## Style

It is often helpful to make an outline of your paper, with figures, before you write it. In this way, you can be sure that the logical development of your presentation does not resemble two octopuses fighting, but that it is linear. Often the order of your journal notebook is not the same order in which you should present the data.

One generally writes the report in the past tense. You also should use the third person. Even though you might have done the work by yourself, use "we," e.g., "*We calculated the transition probability for...*" It is often confusing when you begin sentences with conjunctions. Make sure that each sentence is a clear positive statement rather than an apology.

There are a few words or phrases you should be careful of using. **Fact** – this is a legal word and is generally avoided in the physics literature. **Proof or prove** – These words are meaningful in mathematics and you cannot prove something in physics, especially experimental physics. **The purpose of this experiment is...** – Through background information we outline the issue we aim to solve. **One can easily show that...** – Do not intimidate the reader. Remember that the reader of your paper is a senior in college! **It is obvious that...** or **One clearly can see....** – Such statements only intimidate the reader that does not find your work trivial. **Data** is the plural form of the noun datum. "The data are..." or "The data show that...". **Human Error** – has no specific meaning but instead indicates an unspecified error. Errors must be quantified, not swept under a rug and remain unnamed. **'In order to'** – this phrase can usually be replaced with just the word 'to'. **Almost exactly** – we do not know how can something be almost and exact at the same time

Adhere strictly to the template and format guidelines required by the publisher of the journal. The newest JURP templates and formatting guidelines are available online.

Lastly, the journal may request that you suggest reviewers of your manuscript. Reviewers should be as unbiased as possible and knowledgeable of the area of physics you are doing. Possible reviewers are scientists that have recently published in the same or related areas of physics as your manuscript. Good reviewers will offer helpful criticism of your work to improve the manuscript. The journal editor may also offer suggestions to improve the manuscript and ultimately has the responsibility to accept or reject your manuscript or revisions for publication.

## ACKNOWLEDGMENTS

This short section should acknowledge the help received from others if it is not referenced in the previous sections. This is where you would give credit to a colleague or someone in the machine shop who helped you build a piece of equipment. You may also include your funding source, if appropriate.

## REFERENCES

References should be numbered using Arabic numerals followed by a period (.) as shown below and should follow the format in the examples. Ref. 1 is for a book. Ref. 2 is for a journal article.

1. M. P. Brown and K. Austin, *The New Physique* (Publisher Name, Publisher City, 2005), pp. 25–30.
2. M. P. Brown and K. Austin, *Appl. Phys. Letters* **85**, 2503–2504 (2004).
3. R. T. Wang, “Title of Chapter,” in *Classic Physiques*, edited by R. B. Hamil (Publisher Name, Publisher City, 1999), pp. 212–213.
4. C. D. Smith and E. F. Jones, “Load-cycling in cubic press,” in *Shock Compression of Condensed Matter-2001*, AIP Conference Proceedings 620, edited by M. D. Furnish *et al.* (AIP Publishing, Melville, NY, 2002), pp. 651–654.
5. B. R. Jackson and T. Pitman, U.S. Patent No. 6,345,224 (8 July 2004).
6. D. L. Davids, “Recovery effects in binary aluminum alloys,” Ph.D. thesis, Harvard University, 1998.
7. R. C. Mikkelsen (private communication).

# JURP

**JOURNAL** *of*  
UNDERGRADUATE  
REPORTS IN PHYSICS

## What is JURP?

The Journal of Undergraduate Reports in Physics (JURP) is a peer-reviewed publication of the society of Physics Students comprised of research, outreach, and scholarly reporting.

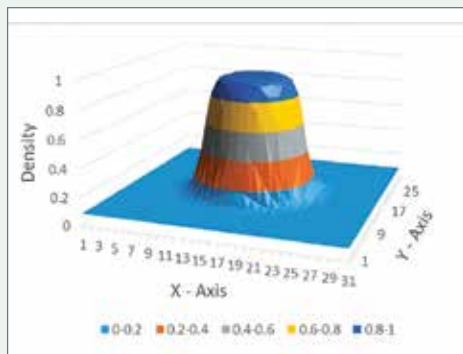
JURP provides exposure for SPS members conducting physics research while also supporting faculty who conduct undergraduate research and scholarship through peer-reviewed publication.

### Research

Peer-reviewed papers within any area of physics research  
Accepted research submissions will be indexed and searchable

### Scholarship

Independent research across all of physical sciences: physics, quantum, astronomy, engineering physics, astrophysics, optics, mathematical physics, nano-science, acoustics, meteorology, physics education, particle physics, electronics, medical physics, and more



## Submit Your Report!

All current SPS members are eligible to submit to JURP. The author(s) must have performed all the work reported in the paper as an undergraduate student.

SPS National will accept the submissions to JURP on a rolling basis, but final deadline for the print edition is **March 15**.